Spring 1-1-2015

Molecular Thermodynamics of Superheated Lipid-Coated Fluorocarbon Nanoemulsions

Paul A. C. Mountford
University of Colorado Boulder, paul.mountford@colorado.edu

Molecular Thermodynamics of Superheated Lipid-Coated Fluorocarbon Nanoemulsions

by

PAUL A. C. MOUNTFORD

B.S., University of Colorado Boulder, 2010

M.S., University of Colorado Boulder, 2011

A thesis submitted to the
Faculty of the Graduate School of the
University of Colorado in partial fulfillment
Of the requirement for the degree of
Doctor of Philosophy
Department of Mechanical Engineering
2015

This thesis entitled:
Molecular Thermodynamics of Superheated Lipid-Coated Fluorocarbon Nanoemulsions
written by Paul Mountford
has been approved for the Department of Mechanical Engineering

---

Professor Mark Borden
Mechanical Engineering, University of Colorado Boulder

Professor Todd Murray
Mechanical Engineering, University of Colorado Boulder

Professor Yifu Ding
Mechanical Engineering, University of Colorado Boulder

Date: July 17, 2015

The final copy of this thesis has been examined by the signor, and
finds that both the content and the form meet acceptable presentation standards
of scholarly work in the above mentioned discipline.

Abstract

Mountford, Paul (Ph.D., Mechanical Engineering)

Molecular Thermodynamics of Superheated Lipid-Coated Fluorocarbon Nanoemulsions

Thesis directed by Associate Professor Mark Borden

Diagnostic ultrasound is a safe, inexpensive and highly portable real-time imaging modality for viewing the human body. For over two decades, lipid-coated fluorocarbon microbubble contrast agents have been developed to help improve the diagnostic and therapeutic capabilities of ultrasound, but they have certain limitations. Recently, it was found that the microbubbles can be condensed into superheated liquid nanodrops capable of being vaporized by external optical or acoustic triggers. The compact form and vaporization effects of these phase-shift nanodrops may offer advantages over microbubbles for a number of current and future therapeutic and diagnostic applications. The goal of this dissertation work was to study the molecular thermodynamics and interfacial phenomena of these superheated phase-shift nanodrops.

In the first part of this work, a custom microscopy pressure chamber with control over temperature and pressure was used to observe microbubbles during condensation. Compression behaviors of fluorocarbon microbubbles constructed with lipid shells of varying acyl chain lengths were quantified over a broad temperature range. Microbubbles containing lipids of longer acyl chains were found to resist ideal compression and condensation. Dissolution was found to dominate as temperature approached the lipid main phase transition temperature, resulting in incomplete condensation. However, successful condensation of gas-filled microbubbles to liquid-filled nanodrops could be achieved at lower temperatures, and fluorescence microscopy showed that the lipid monolayer shell buckles and folds into surface-attached bilayer strands. The

nanodrops were found to be remarkably stable when brought back to standard temperature and pressure. The temperature-pressure data were used to construct condensation phase diagrams to determine the thresholds for successful nanodrop formation.

In the second part of this study, the superheated nanodrops were vaporized back into microbubbles by changes in temperature and pressure. A custom optical chamber with control over temperature and pressure was used to track the kinetics of condensation, vaporization and dissolution of microbubble suspensions with varying fluorocarbon core and lipid shell compositions. A simple model was used to extract kinetic rates from the optical data, and Arrhenius plots were used to determine activation energies. The activation energy for thermal vaporization was found to vary with lipid acyl chain length, and a simple model of lipid intermolecular forces was used to explain this effect. Additionally, thermal vaporization was found to occur near 90% of the critical temperature of the fluorocarbon core, indicating that metastability of the superheated droplets was due to the low probability of homogenous nucleation rather than a Laplace overpressure. The superheated droplets could be reversibly vaporized and condensed to at least ten cycles, showing remarkable stability.

In the final part of this study, the tunability of vaporization was examined through the mixing of fluorocarbon gases in droplet core. A clinical ultrasound imaging system was used to track vaporization as a function of temperature and mechanical index. Discrepancies were found in the vaporization thresholds owing to mass transfer; the high solubility of the lower fluorocarbon caused it to rapidly deplete. However, a successful acoustic temperature probe was demonstrated. The experimental data from all three parts of this study were examined and explained by conventional molecular thermodynamics theory, providing new insights into the behavior and properties of these novel theranostic agents.

To my comrade, my brother

Samuel C. B. Mountford

Upon being cut from the high school freshman basketball team, my father, Dr. Mark C. Mountford, provided me with this quote:

It is not the critic who counts; not the man who points out how the strong man stumbles, or where the doer of deeds could have done them better. The credit belongs to the man who is actually in the arena, whose face is marred by dust and sweat and blood; who strives valiantly; who errs, who comes short again and again, because there is no effort without error and shortcoming; but who does actually strive to do the deeds; who knows great enthusiasms, the great devotions; who spends himself in a worthy cause; who at the best knows in the end the triumph of high achievement, and who at the worst, if he fails, at least fails while daring greatly, so that his place shall never be with those cold and timid souls who neither know victory nor defeat.

- Theodore Roosevelt, 1910

It has resonated with me ever since and is embedded in this work.

Acknowledgements

First I would like to thank my advisor and mentor Dr. Mark Borden. He welcomed me into his lab with an unparalleled desire to teach and motivate. He was consistently critical and excited about this work and provided remarkable guidance throughout the past four years. He allowed me to "skin the cat" how I saw fit and utilize my skill sets while suggesting improvements as needed. He has been an exceptional mentor and friend. For this I am truly grateful.

I would like to thank the entire Borden lab. I would like to thank Dr. Jake Dove for continuously sharing exciting results and knowledge which unveiled the fundamental mechanisms of this work. I would like to personally give thanks to Dr. Shashank Sirsi for having introduced me to the Borden lab. He took me under his wing and showed me how to become a graduate researcher. Additionally, he contributed to this work without hesitation and allowed me to collaborate on his studies as his peer. From the first day I joined the group he supported my research and treated me like a fellow scientist. He remains a great friend and collaborator.

I would like to thank Julie Bielinski for being the constant light at the end of the tunnel during the final enduring year of this graduate work.

Finally I would like to thank my family. My mother, Prof. Gillian Collie, who taught me to be critical of the world I live in since I could remember. My father, Dr. Mark Mountford, who taught me to appreciate the struggles and failures associated with success. My stepfather, John Moser, who motivated me to use my mind over my body and taught me that expedited respect is obtained through kindness. My brother, Samuel Mountford, who taught me how to be a mentor and take criticism with a light heart.

Contents

Tables

Figures

Chapter 1

Introduction

1.1 Specific Aims

The intention of this work was to identify the thermodynamic conditions necessary for the condensation of a phospholipid-coated gas microbubble into a liquid nanodroplet and the vaporization of a condensed nanodroplet back into a gas microbubble. More specifically, this study looked to examine the following:

1. To measure the condensation pressures of lipid-coated perfluorocarbon (PFC) core microbubbles over a large range of temperatures and explore the effects varying the lipid acyl chain length has on the compression and condensation dissolution behaviors.
2. To identify the vaporization temperatures of microbubble condensed nanoemulsions and approximate the thermal phase-shift activation energies for liquid nanodroplets with varying acyl chain length lipids and PFC gas cores.

3. To control the thermal and acoustic vaporization of a microbubble condensed nanodroplet through the predetermined selection and combination of the nanodroplet shell and core materials.

Prior to executing these specific aims, the following was hypothesized:

1.1 The condensation pressure of a lipid-coated PFC microbubble, dependent of temperature, should not stray far from the PFC macroscopic condensation pressure.

1.2 The lipid-monolayer shell of the microbubble should decrease the dissolution of the microbubble during pressurization and improve condensation stability.

1.3 Any inhibition of microbubble condensation pressure compared to macroscopic condensation pressure is due to additional strength and rigidity provided by the lipid shell.

2.1 The vaporization temperature of a PFC microbubble-condensed nanodroplet is greater than the PFC bulk boiling temperature.

2.2 This enhanced resistance to vaporization was previously hypothesized as being a product of the increased Laplace pressure experienced in the droplet core. Here, the superheated stability of droplets is due to the Laplace pressure in combination with the energy barriers associated with expanding the lipid monolayer shell and forcing the formation of the gas phase.

2.3 The activation energy for the thermal actuation of a droplet into a bubble is positive indicating that additional thermal energy is required to vaporize a droplet into a gaseous state.

3. The PFC-core composition of a microbubble condensed nanoemulsion can be carefully manipulated so that vaporization can occur over a specific temperature range and mechanical index at constant pressure. Specifically, PFC gases can be mixed with

sufficient specificity to create multi-component nanodroplet cores providing controllable multi-modal vaporization.

This study is motivated by the principle of understanding before applying. Through an in-depth investigation of microbubble-condensed nanodrops and their condensation and vaporization properties, a heightened control over their stability and behaviors can be achieved. A profound understanding of condensed droplet phase-shift behavior exposes physical limitations and improves their reproducibility for various applications. Varying the lipid composition of the shell during condensation and vaporization provides new information on lipid monolayer strength and integrity. Changing the PFC used in the microbubble core will elucidate the molecular thermodynamic properties of a micron-sized PFC sphere, clarify the principles responsible for condensation and vaporization and make it easier for researchers to effectively apply this technology. Finally, mixing PFCs to tune thermal vaporization will expose the stability of multi-component condensed nanodrops and inform investigators on their limitations and applicability for various applications.

1.2 Microbubbles

1.2.1 Microbubble Design and Behavior

The title of this investigation reads "*Molecular Thermodynamics of Superheated Lipid-Coated Fluorocarbon Emulsions*". With molecular thermodynamics headlining this work, it makes sense to introduce microbubbles with one of the most fundamental laws of thermodynamics. It is understood that gases are compressible and can change their volume with temperature and pressure whereas liquids are incompressible and maintain their volume independent of temperature and pressure. From the ideal gas law, $PV = nBT$, (where P is pressure, V is volume, n being the number

of moles, B is the ideal gas constant (8.3144 m^3 Pa K^{-1} mol^{-1}) and T is temperature) it is known that the volume of a gas is inversely proportional to its pressure. From this, one can deduct that an oscillation in pressure would cause an oscillation in gas volume, therefore expanding and contracting the exposed surface of the gas volume (surface area). In principle, the cyclic pressurization rate defines the gas volume expansion and contraction (oscillation) rate. These are the fundamental principles for designing contrast agents for diagnostic ultrasound imaging.

Ultrasound technology emits sound waves in the ultrasound frequency range traditionally varying from 1 to 18 MHz. At these frequencies the fluctuation in pressure is extremely fast and would provide spatial gradients in pressure for a relatively large volume of gas. A gas volume can only oscillate uniformly if it is experiencing a uniform change in pressure across the entire volume. If the size of the gas volume (d, diameter) is significantly smaller than the wavelength (λ) of the pressure wave imposed on the gas particle ($d << \lambda$) then the particle experiences a uniform pressure fluctuation and can oscillate, scattering sound as defined by Rayleigh scatter.[1] A gas particle suspended in a liquid medium is commonly referred to as a bubble. Comparable to water, the speed of sound in tissue is roughly 1540 m s^{-1} permitting ultrasound imaging of the anatomy.[2] The physiological speed of sound (c) and the frequency range of diagnostic ultrasound imaging (f) provides wavelengths ranging from 85 to 1540 μm in the tissue being imaged ($\lambda = c/f$). A gas bubble will scatter sound if its diameter is less than 85 μm. A stable gas particle on the order of ~10 μm in diameter can provide a means of effectively scattering ultrasound thereby enhancing the signal-to-noise ratio received by any given diagnostic ultrasound technology. Hoff also confirmed that 1-10 μm gas particles scatter sound most efficiently from 1 to 10 MHz (Fig. 1.1).[3]

In order to effectively transport and scatter ultrasound within the vasculature of the human anatomy, ultrasound scattering microbubbles need to be of a similar size to red blood cells (<10

μm).[4,5] Microbubbles of this size naturally occur when a gas-liquid interface is agitated, but are extremely unstable due to a pressure difference between the gas core of the microbubble and its liquid surroundings.[6] This pressure difference is defined by Laplace as:

$$P_{IN} - P_{OUT} = \frac{2\gamma}{R} \tag{1.1}$$

where P_{IN} is the internal microbubble pressure, P_{OUT} is the hydrostatic pressure, γ is the interfacial surface tension of water and air (72 mN m^{-1}) and R is the particle radius.[7,8] With constant surface tension, as the particle radius decreases, the pressure inside the bubble increases leading to expedited dissolution of the gas phase into the surrounding liquid. Upon examining Equation

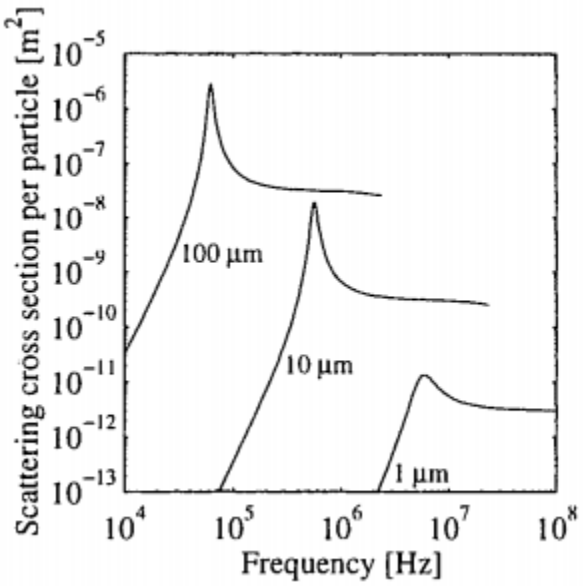

Figure 1.1. The scattering cross-section of a gas particles (1-100 μm in diameter) versus the sound excitation frequency.[3]

1.1, it is apparent that the interfacial surface tension must be reduced to decrease the pressure difference across the air-water interface and prolong the stability of the bubble. In an attempt to lower the air-water surface tension of microbubbles, researchers have looked to the lungs and their ability to minimize the surface tension between inhaled air and pulmonary fluid.[9] More

specifically, the lung surfactants of various animals have been measured for their interfacial surface tensions. Tierney and Johnson showed that surface tension could be reduced to values near 0 mN m^{-1} (0-5 mN m^{-1}).[10] Recently, Sirsi et al. created bubbles that were stable at less than 10 μm in diameter with the extracted bovine lung surfactant drug Survanta.[11] Bovine lung surfactant is primarily made up of phospholipids (79% phosphatidylcholine, DPPC) which are the amphiphilic molecules responsible for stabilizing bubbles at micron-sized diameters.[12] The most common method of stabilizing a microbubble emulsion consists of introducing phospholipids into the aqueous phase during fabrication and is the method used in this work.[13]

Microbubbles, formed with phospholipids, can be generated through probe sonication, amalgamation, extrusion or microfluidics. These fabrication methods all consist of introducing a lipid monolayer at a gas-liquid interface, with the gas being the desired core material of the microbubble, and the liquid being water (commonly having an ionic strength). Figure 1.2 presents the positioning of phospholipids at the gas-liquid interface of a bubble with their hydrophobic tails oriented inwards towards the gas phase and their hydrophilic phosphatidylcholine head groups adhering to the liquid.[14] To generate microbubbles via sonication, an ultrasound probe sonicator

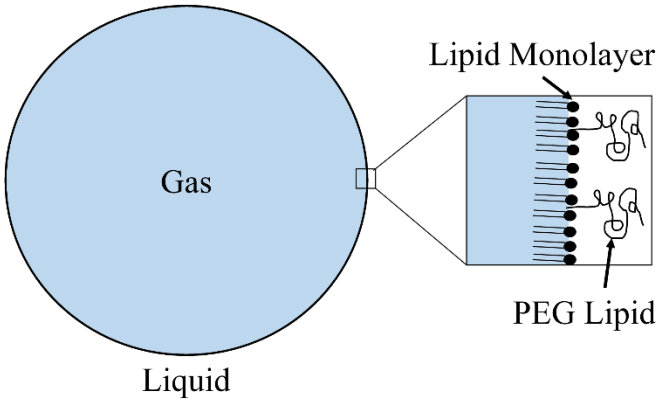

Figure 1.2. Cartoon showing the orientation of lipid molecules at a gas liquid interface. Additionally, the lipid monolayer contains polyethylene glycol-functionalized lipids commonly used for limiting the likelihood of microbubble coalescence.

is introduced to a gas-liquid interface and emits acoustic waves causing the formation of capillary waves at the surface. These standing waves at the interface then cause the entrapment of the gas within the liquid, resulting in the formation of bubbles. As the probe sonicator continues to emit ultrasound waves, the larger bubbles undergo break-up into smaller micron-sized bubbles. This proposed mechanism for microbubble formulation via probe sonication (Fig. 1.3), proposed by

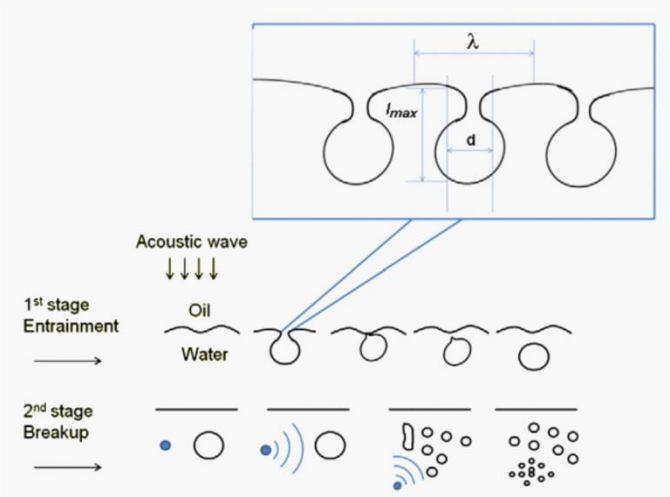

Figure 1.3. Depiction of the proposed sonication microbubble formulation mechanism. Initially, standing waves cause the entrapment of larger bubbles similar in size to the sonication wavelength (λ). As sonication of the suspension persists, larger bubbles are subjected to a secondary breakup phenomena forming microbubbles that are stabilized due to the rapid absorption of lipids at the gas-liquid interface.[15]

Feshitan et al. [15], provides a polydisperse microbubble size distribution with peak a diameter around 1-2 µm. One can easily visualize how amphiphilic lipids can absorb and orient themselves at the gas-liquid interface of a newly formed microbubble when referring to Figures 1.2 and 1.3. Amalgamation also causes the formation of a polydisperse, micron-sized bubble distribution. To form microbubbles through amalgamation, a sealed vial is filled partially with an aqueous lipid suspension, and the desired gas-core material is added to occupy the vial's remaining volume. The vial is then agitated violently, most commonly in a dental amalgamator, causing the formation of a microbubble-in-water emulsion.[16] To better control microbubble size, sonicated and/or

homogenized gas-in-water lipid emulsions have been passed through micron-sized (50-100 μm in diameter) porous filters for the extrusion and formation of monodisperse microbubble solutions.[17] Most recently, microfluidics has been used to create small quantities of perfectly monodisperse microbubble suspensions by introducing the gas core material to the shell material suspension in a confined channel.[18] All microbubbles in this work were formed either using probe sonication or amalgamation.

Uncoated microbubbles statically suspended in solution are subject to a Laplace pressure (Eqn. 1.1), which is responsible for driving out the gas core into the aqueous surroundings. Introducing a lipid monolayer at the gas-liquid interface has been shown to lower the surface tension resulting in a decreased Laplace pressure and increased microbubble stability. It has been shown that lipid monolayers reduce interfacial surface tension from 72 mN m^{-1} (that of a naked gas-water interface) to approx. 0-25 mN m^{-1}.[14,19] Regardless if a microbubble has a lipid shell or not, the microbubble is still going to dissolve as described by Epstein and Plesset[20]:

$$\frac{dR}{dt} = -Dk_h BT \frac{1 - f + \frac{2M_w\gamma}{\rho BTR}}{1 + \frac{4M_w\gamma}{3\rho BTR}} \left[\frac{1}{R}\right] \tag{1.2}$$

where R is the bubble radius, t is time, D is the diffusion coefficient of the gas in the medium, k_h is the Henry's constant for the gas in water, f is the ratio of the initial gas concentration to that at saturation (saturated, $f = 1$), M_w is the gas molecular weight, γ is the surface tension, and ρ is the gas density.[21] Borden and Longo[22] studied the effects of lipid shell on dissolution and re-derived the dissolution of a lipid-coated microbubble to contain a gas permeation resistance term dependent of the lipid species being used.

Lipid molecules are very small (~0.4 nm in diameter) in comparison to a microbubble and are assumed to be in a flat 2D monolayer when compressed or expanded. This assumption permits

investigating lipid monolayer compression mechanics on a Langmuir trough and translating the monolayer stress and folding results to a microbubble geometry.[23] Kwan and Borden[24] studied microbubble gas exchange in an open environment and found that microbubbles initially grew to a larger size and then slowly shrank until being fully dissolved. They found that the lipid monolayer shell was smooth during expansion and then underwent a compression phase which caused the shell to appear wrinkled followed by a relaxation phase which caused the shell to appear smooth again.[25] The relaxation phase was believed to occur when the compressive stress was so high that the lipids formed bilayers to minimize energy (Fig. 1.3). These lipid monolayer studies help in understanding the stability of microbubbles in a compressive state, but are limited to minimal compression driven by dissolution.

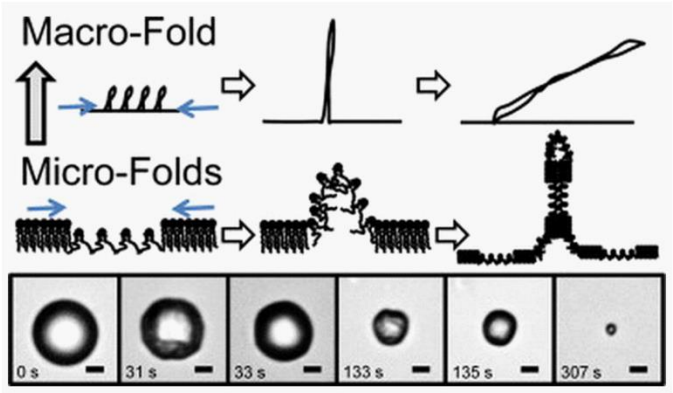

Figure 2.4. Cartoon schematic showing lipid bilayer formation caused by monolayer compression being driven by microbubble dissolution.[25]

1.2.2 Microbubbles for Diagnostic Imaging

Diagnostic ultrasound imaging is a highly portable, inexpensive and safe method of imaging the human anatomy. Shell-stabilized gas-in-liquid emulsions have been heavily researched for improving the diagnosis capabilities of ultrasound imaging by enhancing contrast within the vasculature. Figure 1.5 presents traditional diagnostic ultrasound cadence pulse sequencing (CPS)

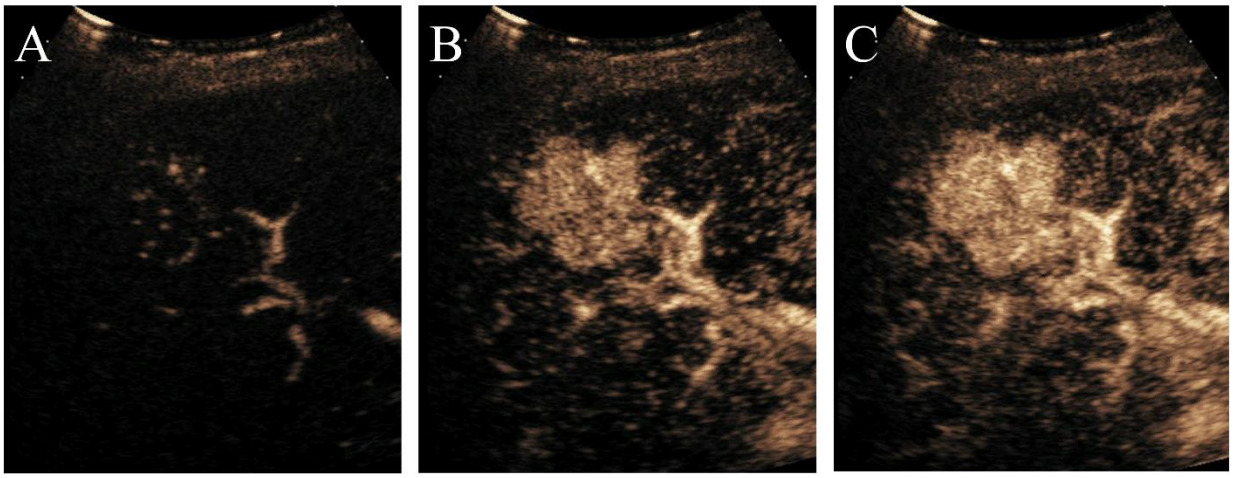

Figure 1.5. Contrast enhanced diagnostic ultrasound CPS images taken as microbubbles reach the liver vasculature of a human. Minimal contrast is observed as microbubbles begin to reach the region of interest (**A**), but as circulation continues enhanced contrast is apparent (**B, C**). Courtesy of Siemens Ultrasound.

images showing the contrast enhancement of microbubbles flowing through liver vasculature in a human. This amazing ability to enhance the diagnostic efficacy of ultrasound imaging came from the hurried preparation of an indocyanine green contrast injection for an echocardiogram of the mitral valve in 1967.[26] The same contrast effect was also seen with a 5% dextrose in water solution.[27] Upon observing the two solutions, it was noticed that a thin film of cloudy foam, comprised of small particles, was present. After concluding that the enhanced contrast effect was due to the presence of bubbles, Gramiak and Shah produced the first microbubble contrast enhanced ultrasound study of the aortic root with the injection of an agitated saline solution.[28] Since 1968, microbubbles have been researched for enhancing the diagnosis capabilities of ultrasound imaging in all parts of the anatomy, but have only been FDA-approved for echocardiography (1997).[29]

Early researchers narrowed the optimal microbubble size range to 1-10 μm in diameter because microbubbles smaller than 1 μm in diameter lacked the desired enhanced contrast effect and bubbles larger than 10 μm were considered too large for intravascular circulation and more

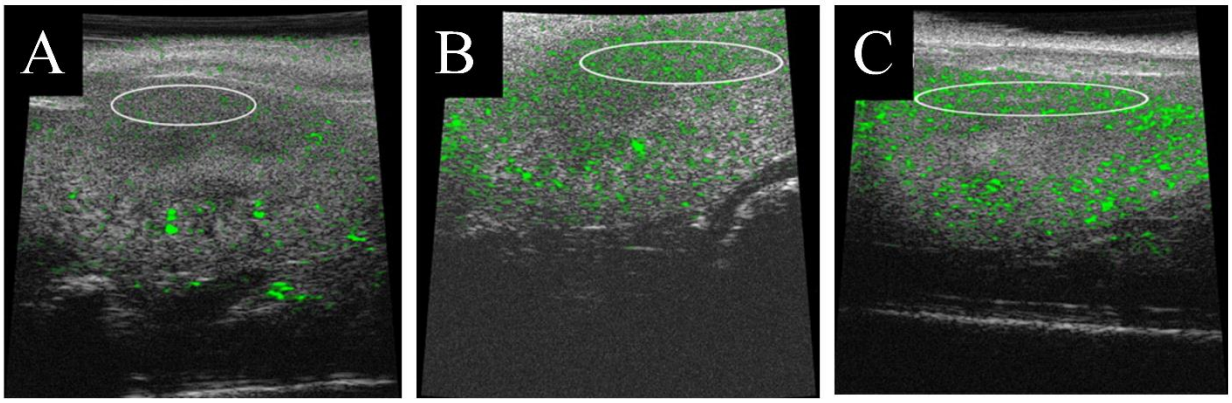

Figure 1.6. Fundamental mode high-frequency ultrasound *in-vivo* images of 1-2 (**A**), 4-5 (**B**) and 6-8 (**C**) μm bubbles persisting in the kidney of a mouse.[30]

susceptible to phagocytosis. FDA-approved microbubbles, manufactured as Optison and Definity, claimed to have tighter size distributions around 2.0-4.5, 6.0, 1.1-3.3 μm in diameter, respectively.[29] Upon recognizing that commercial microbubble emulsion manufacturers were producing emulsions with different mean diameters, researchers sought to determine the optimal, monodisperse, microbubble solution for contrast enhanced ultrasound. Sirsi et al. showed that bubbles 6-8 μm in diameter provided the best high-frequency ultrasound imaging contrast and had the longest circulation half-life compared to bubbles ranging from 1-2 or 4-5 μm in diameter (Fig. 1.6).[30] SonoVue, a recently FDA-approved microbubble contrast agent for echocardiography, proved that 80% of contrast enhancement was due to microbubbles with 3-9 μm diameters, even though 1-3 μm diameter bubbles accounted for 50% of the bubbles in the solution.[31] With smaller 1-3 μm bubbles lacking in ultrasound scattering cross-section, it has been hypothesized that bubbles 3-8 μm in diameter are optimal for contrast enhanced diagnostic ultrasound.

As previously mentioned, forming microbubbles with a microfluidic apparatus provided a near perfect monodisperse microbubble emulsion when operated at low pressures and flow rates.[32] Although microbubble size was precise, this method lacked the bubble generation rate necessary for producing useful quantities of microbubbles in a cost-effective manner. Increasing

the microfluidic flow rates and pressures to improve bubble production time has been shown to reduce the monodispersity of the microbubble emulsion. More recently, a method of producing size-selected microbubbles with a narrower size range (as compared to 1-10 μm) has been presented by Feshitan et al.[15] This method consisted of producing large amounts of polydisperse microbubbles that were then size-selected through differential centrifugation. To elaborate, microbubble differential centrifugation consists of centrifuging the emulsion at different speeds to change the relative gravity experienced by the buoyant microbubbles, allowing larger ones to rise into the supernatant. This method of producing size-selected microbubble solutions has been widely used and is used predominantly in this work.

Microbubbles have not only been limited to enhancing diagnostic ultrasound imaging. Microbubble shells have been functionalized and conjugated to different particles and molecules to provide enhanced contrast under various imaging modalities.[33] One of the most common forms of bi-modal diagnostic imaging is magnetic resonance (MR) – ultrasound imaging which requires a contrast agent that is magnetic and scatters sound efficiently like a microbubble. Liu et al. attached iron oxide particles to polymer-shelled microbubbles which provided T_1 and T_2-relaxivity and enhanced ultrasound contrast in a MLS mouse tumor during microbubble persistence.[34] Upon ultrasound-induced destruction, T_1-relaxivity was increased providing a stable MR imaging contrast agent. Nanoparticles have been attached to microbubbles to enhance fluorescent and molecular imaging.[35] Ke et al.[36] electrostatically conjugated CdTe quantum dots to fluorosurfactant-coated microbubbles and observed a contrast enhancement in ultrasound and ultraviolet fluorescent imaging. Additionally, a photoacoustic-ultrasound dual contrast agent was created by Dove et al.[37] where gold nanoparticles were conjugated onto the surface of a phospholipid microbubble with avidin-biotin binding (Fig. 1.7). Although photoacoustic-

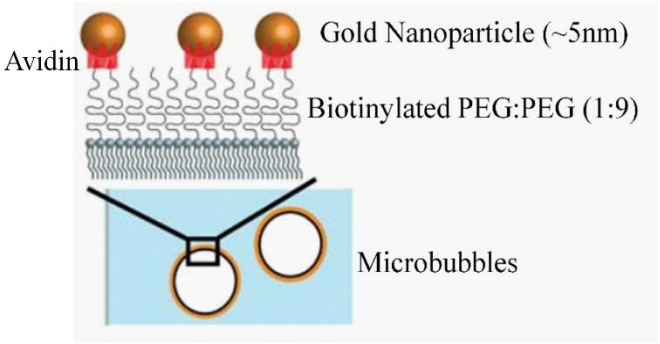

Figure 1.7. The gold nanoparticle – lipid microbubble avidin-biotin conjugation scheme used to produce photoacoustic-ultrasound contrast enhancing microbubbles.[37]

ultrasound contrast agents had been previously made with the optically absorbing species in the core,[38] the shell-conjugated dual modal agents provided longer lasting contrast enhancements due to the functionalization of the shell instead of the core. Functionalizing a microbubble shell not only provides an anchor for secondary imaging contrast agents, but opens a window for attaching various molecules, particles and genes for targeted therapy within the vasculature.

1.2.3 Microbubbles for Therapy

Microbubbles can provide treatment within the vasculature by delivering a pharmaceutical payload to an intended area, carrying and improving the uptake of genes into targeted cells, aiding in tumor ablation through lowering the tissue cavitation threshold and accelerating clot lysis via sonothrombolysis.[39,40] Therapeutic microbubbles, commonly stabilized by a lipid or polymer shell,[41] can be loaded with drugs by attaching them to the shell membrane, embedding them within the shell construct, enclosing them in core and encapsulating them around the gas core using double emulsion techniques.[42] The ability to deliver model drugs, loaded onto the surface of microbubbles, to a targeted location of the vasculature has been shown by Lum et al.[43] This work utilized ultrasound radiation forces to push fluorescent avidin-biotin conjugated microbubbles up against the wall of 200 µm diameter cellulose tubing. Once microbubbles were in location, a more intense fragmentation ultrasound pulse was delivered destroying microbubbles

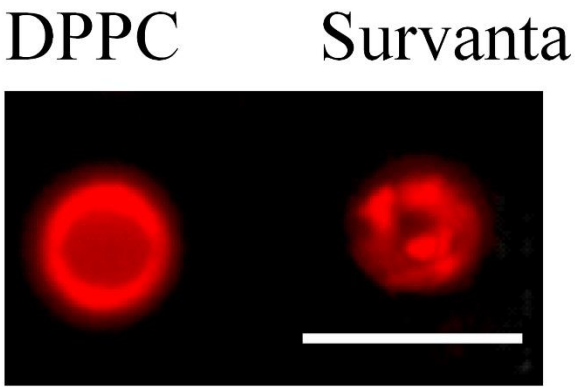

Figure 1.8. Fluorescent microscopy images of DPPC and Survanta coated microbubbles both loaded with a DiI fluorescent dye. DPPC provides a smoother interfacial surface architecture than Survanta.[44]

and leaving behind fluorescent model drug-loaded lipid that had adhered to the tubing wall. Interestingly, Sirsi et al.[44] conducted a similar study but with Survanta-coated microbubbles. Survanta, a natural bovine lung surfactant extract pharmaceutical, contains SP-B and SP-C proteins which are believed to facilitate in the bending and anchoring of lipid monolayers (Fig. 1.8).[45] This folding of the monolayer provided an increased payload surface area and resulted in the heightened delivery of model drug to the tubing wall. Recently, Kang Ho Song from the Borden laboratory showed the enhanced uptake of fluorescent model drug into HeLa cells using

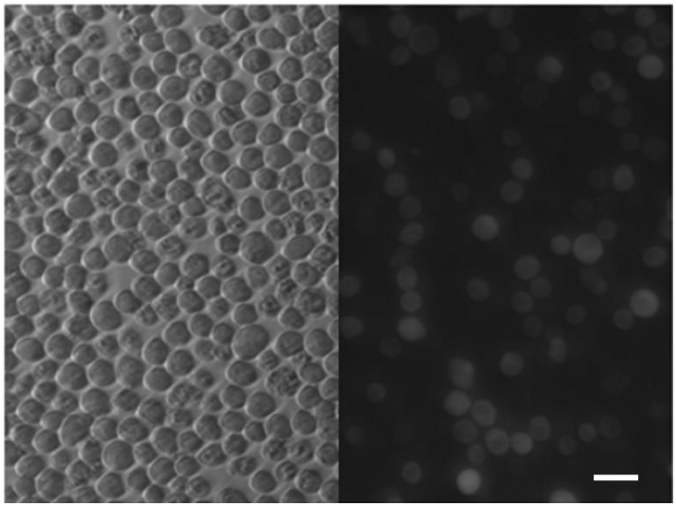

Figure 1.9. Brightfield (left) and fluorescent (right) microscopy of HeLa cells after sonoporation in a solution containing fluorescent red dye and microbubbles. (Courtesy of Kang Ho Song)

therapeutic ultrasound in combination with microbubbles (Fig. 1.9). The ability to disrupt and porate the cellular membrane with sound is known in the literature as sonoporation. Microbubbles in their fabricated state (1-10 µm in diameter) lack the ability to deliver molecules outside the vasculature to areas of interest such as the brain or extravascular tumor tissue.

Therapeutic high-intensity focused ultrasound (HIFU) provides a means of delivering heightened mechanical intensities (sound) to a small region of tissue through the focusing of traditional planar ultrasound waves. Focusing ultrasound can be expensive, administered with HIFU therapeutic concave and linear array transducers, or economically favorable, by simply attaching a poly methyl methacrylate (PMMA) spherical concave lens to a therapeutic ultrasound machine (Fig. 1.10). HIFU can mechanically agitate and enhance the uptake of molecules through the blood brain barrier (BBB), but not without having caused acute damage to tissue when driven near allowable clinical imaging intensities.[46] To avoid the acute ablation of brain tissue, it has been proposed that microbubbles, acting as cavitation nuclei within the blood, can be used at the focal region of ultrasound to lower the HIFU intensity required to open the BBB.[47] Obviously, the thermal necrosis of tissue should be avoided when trying to open the BBB. Having noted that,

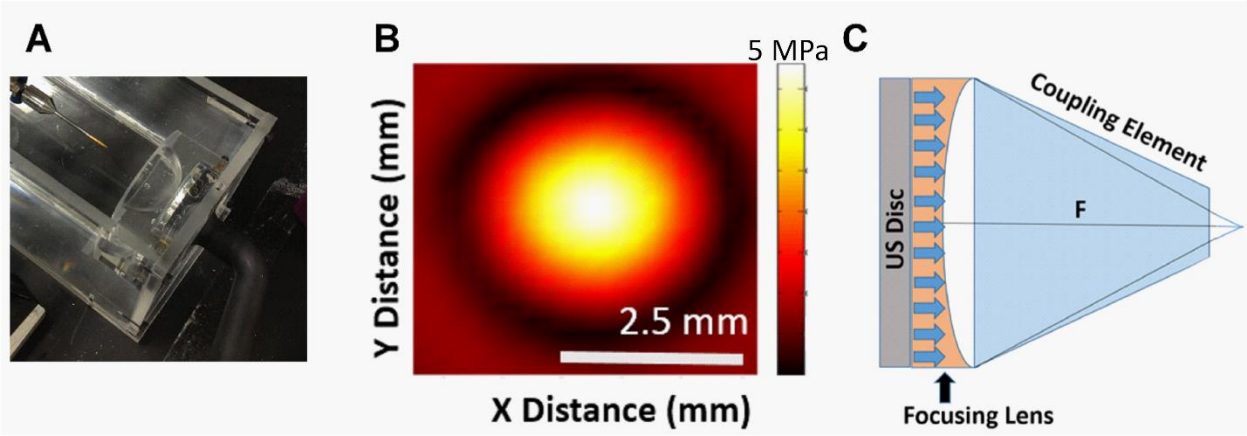

Figure 1.10. A) A PMMA spherical lens attached to a therapeutic ultrasound transducer being measured with a needle hydrophone. **B**) The focused ultrasound intensity provided by the lens at approx. ~4 cm from the transducer. **C**) A schematic showing how a coupling device can be attached to the lens and allow the HIFU device to be used in a dry experimental setting.

HIFU has shown to be extremely effective in the thermal ablation of benign and cancerous tumors throughout the anatomy. Guided by MR imaging, HIFU has been FDA-approved for the treatment of uterine fibroids and is currently undergoing clinical trials for the thermal therapy of breast, liver, prostate, and brain cancer.[48] Kaneko et al.[49] found that introducing microbubbles intravenously to a rabbit liver enhanced HIFU-mediated ablation by providing a greater lesion in the tissue. These studies show the efficacy of ultrasound-mediated non-invasive surgeries and how they can be improved through the use of microbubble contrast agents.

Alternatively, traditional planar ultrasound (non-focused) in combination with microbubble contrast agents has shown the ability to aid in the lysis of clots (sonothrombolysis).[50] Culp et al.[51] showed that microbubbles improved the removal of clots in canine dialysis grafts when subjected to ultrasound. It is proposed that the combination of inertial and stable cavitation along with the radiation forces of ultrasound are responsible for the improvement of sonothrombolysis when microbubbles are present.

To conclude, ultrasound imaging and therapies have been heavily researched for their ability to provide diagnostic information and therapeutic treatment within the anatomy, respectively. Microbubble contrast agents have shown that they enhance these technologies by providing optimal sound scattering cavitation nuclei in a localized, targetable region within the vasculature. Microbubbles are limited to intra-vascular transport because of their size relative to gaps in the endothelial wall of the vasculature (e.g. 100-750 nm in leaky tumors).[52] Referring back to Figure 1.1 shows microbubbles of 100-800 nm diameter providing poor ultrasound scattering. Liquid droplets and solid particles capable of extravasation would provide no contrast due to their incompressibility. A desirable agent would have the ability to exist in one phase for extravasation then shift into another phase and provide ultrasound contrast.

1.3 Phase Change Agents

1.3.1 Fluorocarbon Phase-Shift Droplets for Imaging and Therapy

Phase changing particles are being developed as theranostic (therapeutic-diagnostic) agents capable of providing contrast and carrying a targeted drug payload both within and outside the vasculature. Although droplets can be detected, gas is the only material phase that can sufficiently scatter ultrasound and provide favorable contrast. This indicates that either a liquid-gas, solid-liquid-gas or solid-gas phase transformation is capable of producing an echo-genic microbubble. Simplicity would designate starting with a liquid and adding energy to increase entropy and create a gaseous phase through vaporization. A liquid-gas phase transformation would also be favorable because of the volumetric shift the material undergoes based on its expansion.[53] A droplet with a small liquid volume, for transport into interstitial space, could be vaporized into a larger gas volume providing a microbubble large enough to scatter ultrasound effectively. Typically, vaporization of a liquid droplet at a specific location is executed by focusing acoustic or electromagnetic waves that noninvasively deliver energy (mechanical or thermal) to the droplet.[54,55] Ideally, a droplet would be stable in the liquid state at STP and vaporize *in vivo* with minimal energy.

In order for phase-change agents to be medically applicable they must be sufficiently stable in storage and cardiopulmonary circulation to avoid spontaneous vaporization, and yet they must be volatile enough to vaporize at a relatively low mechanical or thermal dose to prevent damage to healthy tissue. There are many materials that are in the liquid phase at STP that require minimal energy to evaporate, but only PFCs have boiling points near the physiological temperature, provide a stable gaseous microbubble core and are safe to use *in vivo* in small amounts.[56] PFCs with boiling points slightly above physiological temperature, such as perfluorohexane (T_b = 59 ^oC)[57],

are often used to create stable droplet emulsions, but still require a high excitation input for vaporization.[58] For small droplets (<10 μm diameter), the Laplace pressure is believed to suppress vaporization, allowing fluorocarbons with boiling points below physiological temperature, such as perfluoropentane (C_5F_{12}) (T_b = 30 ^oC) to be applied as the liquid core material at 37 °C.[57,59] C_5F_{12}, a liquid at STP, is the most popular PFC droplet material because it remains stable as a liquid in a superheated state and requires minimal actuation energy to form a microbubble. PFCs generally exhibit a volumetric expansion ratio of approx. 125-200 which results in a radial expansion ratio of 5-6. This would indicate that a C_5F_{12} droplet with a diameter of 0.7 μm, capable of extravasation into leaky tumor tissue, vaporizes into a 3.5-4.2 μm diameter bubble optimal for contrast enhanced ultrasound imaging.

Many investigators have shown the ability to enhance ultrasound contrast by vaporizing nanodrops into microbubbles both within and out of the vasculature.[60] Rapoport et al.[61] showed, using contrast enhanced ultrasound imaging, that liver uptake was greater for C_5F_{12} nanodroplets stabilized with a polymer coating than with a surfactant coating. This study also confirmed extravasation of nanodrops to the periphery of a pancreatic mouse tumor. Nanodrops have also been used to enhance other imaging modalities, either separate from or in combination with diagnostic ultrasound. Liquid nanodrops made from perfluorononane (C_9F_{20}) have enhanced contrast for functional magnetic resonance (F-MR) imaging.[62] The addition of gold nanorods to the liquid core of C_5F_{12} droplets has provided both ultrasound and photoacoustic imaging with enhanced contrast *in vivo* (Fig. 1.11).[63] Similarly, C_5F_{12} droplets loaded with indocyanine green have shown enhanced photoacoustic and ultrasound contrast and provided the location of the photoacoustic contrast enhancing particles post vaporization.[64] Not only do nanoparticle-loaded droplets provide dual contrast, but the vaporization event of a droplet provides a high amplitude

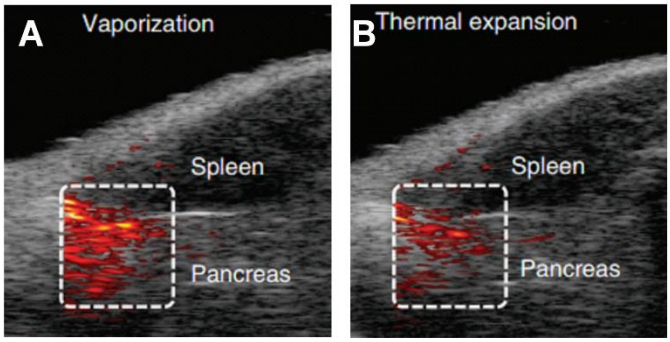

Figure 1.11. Dual ultrasound and photoacoustic contrast provided by the vaporization (A) and continued thermal expansion (B) of gold nanorod loaded C_5F_{12} drops near the pancreas of a mouse.[63]

ultrasonic signal that can be detected by both imaging modalities.[65,66] It is clear that nanodrops have the same applications as microbubbles, but provide a geometry and phase-shift event that is potentially more effective than microbubbles.

Along with providing enhanced contrast outside the vasculature, these nano-scale droplet emulsions are capable of carrying a payload and delivering it during vaporization, or upon destruction of the resulting microbubble.[61,67,68] Liquid phase-change nanoemulsions have been loaded with cancer fighting drugs (paclitaxel) and have released them via ultrasound excitation to treat ovarian carcinoma tumors in mice.[69] Fang et al.[70] showed that nanodrops inhibit the release of highly cytotoxic drugs until activated by ultrasound. The ability to not release drugs in the body until they reach a specific location provides a platform for treating cancerous tissues with a higher therapeutic index. Phase change nanodrops have been shown to have greater circulation times than microbubbles, which increases the likelihood that the drugs on the droplet will be administered to harmful tissue under ultrasound and not filtered out through the kidneys or liver.[71] Current literature proposes that a nanodrop is a more effective vesicle than a microbubble for targeting and delivering drugs under ultrasound or photoacoustic excitation.

In addition to pharmaceutical therapies, PFC nanodrops have also enhanced the effects of HIFU-mediated thermal therapies.[72,73] Zhang and Porter[74] used C_5F_{12} droplets as bubble

cavitation nuclei to lower the HIFU intensity required for tissue ablation *in vitro*. This same group furthered this technology by using monodisperse droplets on the order of 100 and 200 nm in diameter (capable of extravasation) to create microbubbles for ultrasound contrast and, concurrently, ablated legions in tissue-mimicking phantoms.[75] Martin et al.[76] proposed a clever approach to lowering HIFU ablation limits by allowing C_6F_{14} and C_5F_{12} nanodrops to coalesce within macrophage cells, making the droplet cross-section larger and more likely to vaporize and cavitate under ultrasound. This approach to tissue ablation would allow for nanodrop extravasation and more effectively lower HIFU intensities. Like microbubbles, phase-shift nanodrops have been investigated as a cavitation nuclei for MR imaging-guided HIFU tissue ablation. Kopecheck et al.[77] improved HIFU ablation technology by taking advantage of nanodroplet coalescence. C_5F_{12} nanodrops coated with gadolinium (Gd) were injected intravenously into rabbits and allowed to accumulate in a VX2 tumors for various lengths of time (0 to 6 hr). It was observed that Gd-nanodrops coalesced, lowering HIFU-ablation intensities, and provided MR imaging contrast. Superheated nanodrops are a promising discovery that may improve the clinical feasibility of various HIFU ablation technologies.

The metastability of nanoemulsions manufactured with C_5F_{12} sparked interest in utilizing low-boiling point fluorocarbons for their heightened volatility. More volatile nanoemulsions require less energy for vaporization allowing for more possible modes of biocompatible phase-change agent excitation. Assuming the Laplace pressure is the reason for the metastability of superheated droplets, maybe it is possible to create a droplet that is right on the verge of vaporizing at physiological temperature (37 °C). From thermodynamics it is observed that gas-liquid phase transformations happen abruptly over small temperature fluctuations. Ideally, droplets could be tailored to vaporize at specific ultrasound intensities or temperatures to behave as a sonothermetry

probe. In order to improve and innovate upon nanodroplet designs, the interfacial phenomena and molecular thermodynamic behavior of phase-shift drops needs to be investigated.

1.3.2 Phase-Shift Droplet Fabrication and Actuation

Like microbubbles, liquid PFC-in-water emulsions are typically generated by sonication, amalgamation, homogenization or microfluidics and are stabilized by adsorbed monolayers of lipids, proteins or copolymers.[78,79,56,74,61,80] Sonicated droplets, generally having a lipid shell, are made by submerging an ultrasonic probe into a liquid PFC-aqueous mixture and agitating the mixture so that smaller particles are formed.[74] The probe is not placed near the gas-liquid interface because microbubbles are undesirable. Extrusion techniques are then used to create monodisperse droplet emulsions. Amalgamation consists of shaking a vial filled partially with a protein or lipid suspension and a liquid PFC. No air exists in the vial to avoid the formation of microbubbles. Polymer droplets are generally formed via homogenization and size selected using filtered extrusion.[81] Microfluidic generation of droplets is identical to the microfluidic generation of microbubbles (section 1.2.1), except that the liquid PFC is introduced to the confined channel. These methods all require the use of a perfluorocarbon that exists in a liquid state at STP and exclude the low-boiling point choices.

In phase-shift nanoemulsion research there exist two main modes of vaporization excitation, acoustic droplet vaporization and optical vaporization. Acoustic droplet vaporization utilizes the high mechanical energy of ultrasound to onset inertial cavitation in the droplet core (liquid) and force complete vaporization.[58,73] Originally, the acoustic vaporization of droplets was thought to have been actuated by the peak negative pressure (PNP) of the ultrasound wave.[82] With the aid of high speed imaging, researchers now speculate that acoustic droplet vaporization occurs due to a superharmonic lensing effect on the liquid PFC core caused by the change in

acoustic properties at the PFC-liquid interface.[83,84] The acoustic intensity required for droplet vaporization is dependent of the ultrasound transducer being used, the temperature of the droplets, and droplet materials, making it hard to compare droplet vaporization intensities. Interestingly, Kawabata et al.[85] mixed multiple perfluorocarbons of different volatilities to achieve desirable acoustic excitation energies. It was found that as the stable PFC (2H,3H-C_5F_{12}) was added from 0 to 100% to the volatile PFC (C_5F_{12}), the acoustic intensity required for vaporization decreased from 12 to 2 W cm^{-2} at 3.4 MHz. Generally speaking, C_5F_{12} droplets have higher than desirable excitation energies which may be able to be lowered through the mixing of PFCs for the core material.[86]

Optical vaporization, on the other hand, is a more complicated mode of vaporization in that the nanoemulsion needs to absorb heat efficiently to onset thermal droplet vaporization. To enhance the heat absorption of the droplets, optically absorbing nanoparticles have been introduced to perfluorocarbon emulsions.[63,87–89] Silica-loaded lead sulfide has been loaded into a C_5F_{12} microemulsions and heated using a 1064 nm laser to actuate phase-change around a fluence of ~ 2 J cm^{-2}.[90] Gold nanoparticles have been injected into the droplet core and vaporized with optical wavelengths ranging from 532 to 800 nm at various optical intensities dependent upon the nanoparticle geometry.[63,91,92] Although acoustic and optical vaporization[93] has been proven, there is still the need for nanoemulsions capable of phase-shift at energies comfortably below the allowed clinical exposure limits.

To increase volatility, Sheeran et al.[94] developed a cold-temperature extrusion method to emulsify liquid droplets comprised of the low-boiling point fluorocarbon, perfluorobutane (C_4F_{10}) (T_b = -2 ^oC)[57] core in a stabilizing phospholipid shell. The droplets resisted spontaneous vaporization when brought to physiological temperature and pressure, but they were easily

converted to microbubbles by acoustic pulsing at relatively low mechanical index. Discovering the metastability of C_4F_{10} extruded droplets led to the invention of an entirely new technique to generate a liquid-to-gas phase change agent: microbubble condensation.[95]

1.3.3 Dual-Component PFC Droplets

PFCs can be mixed for the core of a phase change droplet and vaporize at different temperatures. This indicates that MCDs may have the potential to be tuned for providing *in situ* temperature feedback under diagnostic ultrasound. C_3F_8 and C_4F_{10} mixed superheated droplets have already been applied as detectors for subatomic particles.[99–102] Here, researchers fill a chamber with C_3F_8:C_4F_{10} (1:1) polymer-stabilized droplets and control the environmental conditions with great precision so that the minimal translational energy provided by a neutrino would cause droplets to vaporize, leaving behind a trail of bubbles. These chambers are commonly known as special bubble detectors and most often used deep beneath the surface of the earth for dark matter detection. Although far from detecting dark matter, lipid-stabilized C_3F_8:C_4F_{10} mixed theranostic nanodrops may be able to aid in the diagnostic ultrasound thermal mapping of tissue for various thermal therapy applications.

1.4 Microbubble Condensed Droplets

1.4.1 Condensation

Sheeran et al.'s method of microbubble condensation for the formation of nanodrops all begins with microbubble generation. To generate microbubbles, as previously described, a probe sonicator introduced capillary waves at the interface between the aqueous lipid suspension (DPPC:DSPE-PEG-2K:TAP at 65:5:30) and the perfluorocarbon gas head space which caused the formation of micron-scale gas bubbles (Fig. 1.3).[96] This resulting suspension can be washed

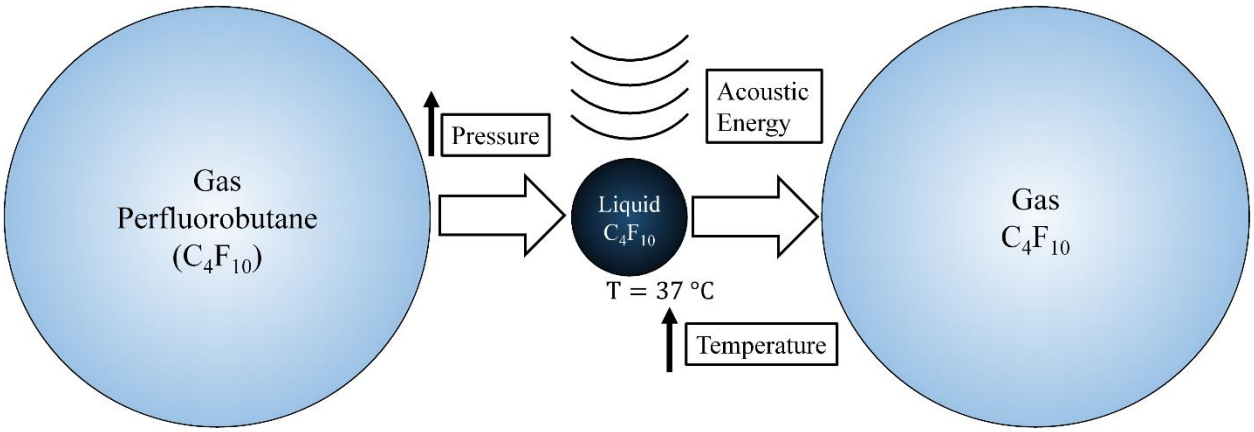

Figure 1.12 Cartoon showing the condensation and re-vaporization of a lipid-stabilized C_4F_{10} microbubble phase change agent.[95]

fractionated to isolate bubbles of a desired size range.[15] The fluorocarbon suspension is then cooled and pressurized to convert the gas microbubbles into liquid droplets (Fig. 1.12). Although these studies proved microbubble condensation through sizing and vaporization studies, their condensation pressures and behaviors have yet to be documented.

Sheeran et al.[97] later went on to show that even microbubble condensed droplets (MCDs) comprising octafluoropropane (C_3F_8) (T_b = -39 °C)[57] were stable against spontaneous vaporization at physiological conditions. It remains unclear how MCDs with such a high degree of superheating (approx. 70 °C) can be stable under physiological conditions. The Laplace pressure in combination with the Antoine vapor equation predicts that C_4F_{10} and C_3F_8 condensed droplets on the order of ~700 µm in diameter should vaporize near the physiological temperature (37 °C), yet somehow these droplets are stable *in vivo*.[98] Regardless of how MCDs retain their surprising metastability, they appear to have great potential as theranostic agents.

1.4.2 Vaporization

Along with liquid forged droplets, only acoustic and optical vaporization of MCD theranostic agents has been investigated. Acoustic droplet vaporization of C_4F_{10} nanodrops was observed by

Sheeran et al. [94], in which 200-300 nm sized MCDs (formed from ~1 μm diameter bubbles) were re-vaporized at a frequency of 5 MHz with an mechanical index (MI) of 1.7 at approx. 22 °C. In a following study, Sheeran also confirmed acoustic droplet vaporization of C_3F_8 MCDs of the same size at a frequency of 7.5 MHz with an MI of 0.4 at 37 °C. [97] This study also reported the PNPs required to vaporize C_4F_{10} and C_3F_8 micron-scale droplets (~ 1 to 5 μm in diameter). Increasing the MCD solution temperature from 22 to 37 °C caused the vaporization PNP to drop from ~ 3.3 to 2.0 and 2.0 to 0.5 MPa for C_4F_{10} and C_3F_8, respectively, and showed the dependence of acoustic droplet vaporization intensity on temperature.

Recently, Dove et al.[93] optically vaporized C_3F_8, C_4F_{10} and C_5F_{12} MCDs utilizing optical energy. Optically absorbing nanoparticles needed to be attached to the surface of the microbubble, instead of injected into the core,[63] so the optical heating ability is retained from the liquid phase to the gas. Mentioned above, Dove et al.[37] attached gold nanospheres onto the surface of size-isolated phospholipid-coated microbubbles and created dual-modal contrast microbubbles. These gold-conjugated microbubbles were condensed using microbubble condensation techniques[94] to

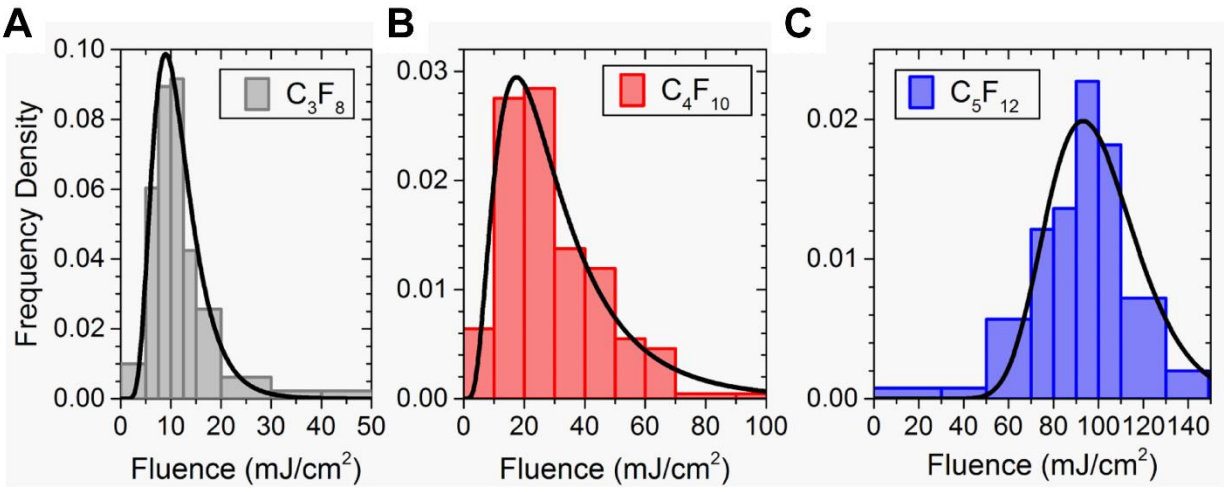

Figure 1.13 The optical vaporization frequency distribution for lipid-coated MCDs fabricated with a C_3F_8 (**A**), C_4F_{10} (**B**) and C_5F_{12} (**C**) core.[93]

form optically active MCDs. These droplets were re-vaporized using a 532 nm laser at ~11, 29 and 96 mJ cm^{-2} for C_3F_8, C_4F_{10} and C_5F_{12} respectively (Fig. 1.13). This result agreed with acoustic studies having showed the ability to change the optical MCD vaporization intensity through selection of the PFC core material. In photoacoustic imaging, higher optical intensities subject nanoparticles to higher degrees of heat, indicating the PFC core material determines the vaporization temperature of a droplet. Currently, there has been no investigation to determine PFC MCD vaporization temperature or validate the mechanism permitting superheated droplet stability.

1.5 Dissertation Objectives

The purpose of this dissertation was to explore the molecular thermodynamic behaviors of superheated fluorocarbon nanoemulsions undergoing condensation and vaporization. The theory of homogeneous nucleation during condensation and vaporization of a pure substance is provided. Experiments providing condensation and vaporization conditions for microbubble condensed droplets MCDs is presented. The work of this dissertation is outlined in the following chapters as so:

Chapter 2. Homogeneous nucleation of a pure fluorocarbon substance: A theoretical prediction of condensation pressure and vaporization temperature is made for a pure supercooled gas and superheated liquid, respectively. The spinodal limit of a liquid-to-gas and a gas-to-liquid phase transition is clarified and approximated. A quantification of the energy barrier associated with greatly compressing and expanding the stabilizing lipid monolayer is presented.

Chapter 3. Condensation of lipid-stabilized fluorocarbon microbubbles: A custom experimental chamber is created to confirm microbubble condensation using microscopy. Microbubble condensation pressures over a range of temperatures, dependent of lipid-shell

composition, are determined. Compression behaviors of the bubble core and lipid monolayer are observed. Condensation pressures of microbubbles were compared to the bulk to elucidate properties inherent of size and geometry.

Chapter 4. Thermal vaporization of microbubble condensed nanoemulsions: An optical extinction chamber is manufactured to monitor microbubble condensation and droplet vaporization. MCD vaporization temperatures and thermal activation energies are quantified dependent of lipid shell materials. Post-vaporization dissolution properties of re-vaporized microbubbles are examined. A more volatile PFC droplet core is used and studied for comparison. An experiment showing the hysteretic phase change capabilities of MCDs is conducted and presented.

Chapter 5. Thermal tunability of superheated fluorocarbon nanoemulsions: MCDs formulated with mixed two-component PFC cores at various ratios are examined during thermal vaporization. Vaporization temperatures are measured in an optical-extinction chamber for multiple core mixture ratios. A temperature controlled water bath is created to confirm MCD vaporization temperatures under ultrasound imaging. Ultrasound vaporization intensities are recorded dependent of core composition and high temperature exposure time. A two-component liquid-in-liquid dissolution model is derived for comparison to experimental results.

References

[1] Sboros, V., Pye, S. D., Anderson, T. A., Moran, C. M., and McDicken, W. N., 2007, "Acoustic Rayleigh scattering at individual micron-sized bubbles," Appl. Phys. Lett., **90**(12), p. 123902.

[2] Ophir, J., 1986, "Estimation of the Speed of Ultrasound Propagation in Biological Tissues: A Beam-Tracking Method," IEEE Trans. Ultrason. Ferroelectr. Freq. Control, **33**(4), pp. 359–368.

[3] Hoff, L., 2002, Acoustic characterization of contrast agents for medical ultrasound imaging, Springer.

[4] Skalak, R., and Branemark, P. I., 1969, "Deformation of Red Blood Cells in Capillaries," Science, **164**(3880), pp. 717–719.

[5] Lindner, J. R., Song, J., Jayaweera, A. R., Sklenar, J., and Kaul, S., 2002, "Microvascular rheology of Definity microbubbles after intra-arterial and intravenous administration," J. Am. Soc. Echocardiogr. Off. Publ. Am. Soc. Echocardiogr., **15**(5), pp. 396–403.

[6] Medwin, H., 1974, "Acoustic fluctuations due to microbubbles in the near-surface ocean," J. Acoust. Soc. Am., **56**(4), pp. 1100–1104.

[7] Menger, F. M., 1979, "Laplace pressure inside micelles," J. Phys. Chem., **83**(7), pp. 893–893.

[8] Eastoe, J., and Dalton, J. S., 2000, "Dynamic surface tension and adsorption mechanisms of surfactants at the air–water interface," Adv. Colloid Interface Sci., **85**(2–3), pp. 103–144.

[9] Pedley, T. J., 1977, "Pulmonary Fluid Dynamics," Annu. Rev. Fluid Mech., **9**(1), pp. 229–274.

[10] Tierney, D. F., and Johnson, R. P., 1965, "Altered surface tension of lung extracts and lung mechanics," J. Appl. Physiol., **20**(6), pp. 1253–1260.

[11] Sirsi, S., Pae, C., Oh, D. K. T., Blomback, H., Koubaa, A., Papahadjopoulos-Sternberg, B., and Borden, M., 2009, "Lung surfactant microbubbles," Soft Matter, **5**(23), pp. 4835–4842.

[12] Yu, S., Harding, P. G. R., Smith, N., and Possmayer, F., 1983, "Bovine pulmonary surfactant: Chemical composition and physical properties," Lipids, **18**(8), pp. 522–529.

[13] D'Arrigo, J. S., and Imae, T., 1992, "Physical characteristics of ultrastable lipid-coated microbubbles," J. Colloid Interface Sci., **149**(2), pp. 592–595.

[14] McConnell, H. M., 1991, "Structures and Transitions in Lipid Monolayers at the Air-Water Interface," Annu. Rev. Phys. Chem., **42**(1), pp. 171–195.

[15] Feshitan, J. A., Chen, C. C., Kwan, J. J., and Borden, M. A., 2009, "Microbubble size isolation by differential centrifugation," J. Colloid Interface Sci., **329**(2), pp. 316–324.

[16] Cuthbertson, A., Tornes, A., Solbakken, M., Moen, O., and Eriksen, M., 2003, "Amphiphilic Lipopeptide Microparticles as Contrast Agents for Medical Ultrasound Imaging," Macromol. Biosci., **3**(1), pp. 11–17.

[17] Okada, K., Shimizu, M., Isobe, T., Kameshima, Y., Sakai, M., Nakajima, A., and Kurata, T., 2010, "Characteristics of microbubbles generated by porous mullite ceramics prepared by an extrusion method using organic fibers as the pore former," J. Eur. Ceram. Soc., **30**(6), pp. 1245–1251.

[18] Wan, J., Bick, A., Sullivan, M., and Stone, H. A., 2008, "Controllable Microfluidic Production of Microbubbles in Water-in-Oil Emulsions and the Formation of Porous Microparticles," Adv. Mater., **20**(17), pp. 3314–3318.

[19] MacDonald, R. C., and Simon, S. A., 1987, "Lipid monolayer states and their relationships to bilayers," Proc. Natl. Acad. Sci., **84**(12), pp. 4089–4093.

[20] Epstein, P. S., and Plesset, M. S., 1950, "On the Stability of Gas Bubbles in Liquid-Gas Solutions," J. Chem. Phys., **18**(11), p. 1505.

[21] Duncan, P. B., and Needham, D., 2004, "Test of the Epstein−Plesset Model for Gas Microparticle Dissolution in Aqueous Media: Effect of Surface Tension and Gas Undersaturation in Solution," Langmuir, **20**(7), pp. 2567–2578.

[22] Borden, M. A., and Longo, M. L., 2002, "Dissolution Behavior of Lipid Monolayer-Coated, Air-Filled Microbubbles: Effect of Lipid Hydrophobic Chain Length," Langmuir, **18**(24), pp. 9225–9233.

[23] Gopal, A., Belyi, V. A., Diamant, H., Witten, T. A., and Lee, K. Y. C., 2006, "Microscopic Folds and Macroscopic Jerks in Compressed Lipid Monolayers," J. Phys. Chem. B, **110**(21), pp. 10220–10223.

[24] Kwan, J. J., and Borden, M. A., 2010, "Microbubble Dissolution in a Multigas Environment," Langmuir, **26**(9), pp. 6542–6548.

[25] Kwan, J. J., and Borden, M. A., 2012, "Lipid monolayer collapse and microbubble stability," Adv. Colloid Interface Sci., **183–184**, pp. 82–99.

[26] MD, B. B. G., 1996, Ultrasound Contrast Agents, CRC Press, London.

[27] Goldberg, B. B., Liu, J.-B., and Forsberg, F., 1994, "Ultrasound contrast agents: A review," Ultrasound Med. Biol., **20**(4), pp. 319–333.

[28] Gramiak, R., and Shah, P. M., 1968, "Echocardiography of the aortic root," Invest. Radiol., **3**(5), pp. 356–366.

[29] Li, P., Armstrong, W. F., and Miller, D. L., 2004, "Impact of myocardial contrast echocardiography on vascular permeability: comparison of three different contrast agents," Ultrasound Med. Biol., **30**(1), pp. 83–91.

[30] Sirsi, S., Feshitan, J., Kwan, J., Homma, S., and Borden, M., 2010, "Effect of Microbubble Size on Fundamental Mode High Frequency Ultrasound Imaging in Mice," Ultrasound Med. Biol., **36**(6), pp. 935–948.

[31] Gorce, J. M., Arditi, M., and Schneider, M., 2000, "Influence of bubble size distribution on the echogenicity of ultrasound contrast agents: a study of SonoVue," Invest. Radiol., **35**(11), pp. 661–671.

[32] Hettiarachchi, K., Talu, E., Longo, M. L., Dayton, P. A., and Lee, A. P., 2007, "On-chip generation of microbubbles as a practical technology for manufacturing contrast agents for ultrasonic imaging," Lab. Chip, **7**(4), pp. 463–468.

[33] Liu, Z., Kiessling, F., and Gätjens, J., 2010, "Advanced Nanomaterials in Multimodal Imaging: Design, Functionalization, and Biomedical Applications," J Nanomater., **2010**, pp. 51:1–51:15.

[34] Liu, Z., Lammers, T., Ehling, J., Fokong, S., Bornemann, J., Kiessling, F., and Gätjens, J., 2011, "Iron oxide nanoparticle-containing microbubble composites as contrast agents for MR and ultrasound dual-modality imaging," Biomaterials, **32**(26), pp. 6155–6163.

[35] Seo, M., Gorelikov, I., Williams, R., and Matsuura, N., 2010, "Microfluidic Assembly of Monodisperse, Nanoparticle-Incorporated Perfluorocarbon Microbubbles for Medical Imaging and Therapy," Langmuir, **26**(17), pp. 13855–13860.

[36] Ke, H., Xing, Z., Zhao, B., Wang, J., Liu, J., Guo, C., Yue, X., Liu, S., Tang, Z., and Dai, Z., 2009, "Quantum-dot-modified microbubbles with bi-mode imaging capabilities," Nanotechnology, **20**(42), p. 425105.

[37] Dove, J. D., Murray, T. W., and Borden, M. A., 2013, "Enhanced photoacoustic response with plasmonic nanoparticle-templated microbubbles," Soft Matter, **9**(32), pp. 7743–7750.

[38] Kim, C., Qin, R., Xu, J. S., Wang, L. V., and Xu, R., 2010, "Multifunctional microbubbles and nanobubbles for photoacoustic and ultrasound imaging," J. Biomed. Opt., **15**(1), p. 010510.

[39] Unger, E. C., Porter, T., Culp, W., Labell, R., Matsunaga, T., and Zutshi, R., 2004, "Therapeutic applications of lipid-coated microbubbles," Adv. Drug Deliv. Rev., **56**(9), pp. 1291–1314.

[40] Ferrara, K., Pollard, R., and Borden, M., 2007, "Ultrasound Microbubble Contrast Agents: Fundamentals and Application to Gene and Drug Delivery," Annu. Rev. Biomed. Eng., **9**(1), pp. 415–447.

[41] Hernot, S., and Klibanov, A. L., 2008, "Microbubbles in ultrasound-triggered drug and gene delivery," Adv. Drug Deliv. Rev., **60**(10), pp. 1153–1166.

[42] Unger, E. C., Hersh, E., Vannan, M., Matsunaga, T. O., and McCreery, T., 2001, "Local drug and gene delivery through microbubbles," Prog. Cardiovasc. Dis., **44**(1), pp. 45–54.

[43] Lum, A. F. H., Borden, M. A., Dayton, P. A., Kruse, D. E., Simon, S. I., and Ferrara, K. W., 2006, "Ultrasound radiation force enables targeted deposition of model drug carriers loaded on microbubbles," J. Controlled Release, **111**(1–2), pp. 128–134.

[44] Sirsi, S. R., 2013, "Lung Surfactant Microbubbles Increase Lipophilic Drug Payload for Ultrasound-Targeted Delivery," Theranostics, **3**(6), pp. 409–419.

[45] Lipp, M. M., Lee, K. Y., Zasadzinski, J. A., and Waring, A. J., 1996, "Phase and morphology changes in lipid monolayers induced by SP-B protein and its amino-terminal peptide," Science, **273**(5279), pp. 1196–1199.

[46] Mesiwala, A. H., Farrell, L., Wenzel, H. J., Silbergeld, D. L., Crum, L. A., Winn, H. R., and Mourad, P. D., 2002, "High-intensity focused ultrasound selectively disrupts the blood-brain barrier in vivo," Ultrasound Med. Biol., **28**(3), pp. 389–400.

[47] Meairs, S., and Alonso, A., 2007, "Ultrasound, microbubbles and the blood–brain barrier," Prog. Biophys. Mol. Biol., **93**(1–3), pp. 354–362.

[48] Jolesz, F. A., 2009, "MRI-Guided Focused Ultrasound Surgery," Annu. Rev. Med., **60**, pp. 417–430.

[49] Kaneko, Y., Maruyama, T., Takegami, K., Watanabe, T., Mitsui, H., Hanajiri, K., Nagawa, H., and Matsumoto, Y., 2005, "Use of a microbubble agent to increase the effects of high intensity focused ultrasound on liver tissue," Eur. Radiol., **15**(7), pp. 1415–1420.

[50] Porter, T. R., and Xie, F., 2001, "Ultrasound, microbubbles, and thrombolysis," Prog. Cardiovasc. Dis., **44**(2), pp. 101–110.

[51] Culp, W. C., Porter, T. R., Xie, F., Goertzen, T. C., McCowan, T. C., Vonk, B. N., and Baxter, B. T., 2001, "Microbubble Potentiated Ultrasound as a Method of Declotting Thrombosed Dialysis Grafts: Experimental Study in Dogs," Cardiovasc. Intervent. Radiol., **24**(6), pp. 407–412.

[52] Hobbs, S. K., Monsky, W. L., Yuan, F., Roberts, W. G., Griffith, L., Torchilin, V. P., and Jain, R. K., 1998, "Regulation of Transport Pathways in Tumor Vessels: Role of Tumor Type and Microenvironment," Proc. Natl. Acad. Sci., **95**(8), pp. 4607–4612.

[53] Watson, K. M., 1943, "Thermodynamics of the Liquid State," Ind. Eng. Chem., **35**(4), pp. 398–406.

[54] Lin, C.-Y., and Pitt, W. G., 2013, "Acoustic Droplet Vaporization in Biology and Medicine," BioMed Res. Int., **2013**.

[55] Strohm, E. M., Min Rui, Kolios, M. C., Gorelikov, I., and Matsuura, N., 2010, "Optical droplet vaporization (ODV): Photoacoustic characterization of perfluorocarbon droplets," 2010 IEEE Ultrasonics Symposium (IUS), IEEE, pp. 495–498.

[56] Sheeran, P. S., and Dayton, P. A., 2012, "Phase-change contrast agents for imaging and therapy," Curr. Pharm. Des., **18**(15), pp. 2152–2165.

[57] Yaws, C. L., 2006, The Yaws Handbook of Thermodynamic Properties for Hydrocarbons and Chemicals, Gulf Pub.

[58] Fabiilli, M. L., Haworth, K. J., Fakhri, N. H., Kripfgans, O. D., Carson, P. L., and Fowlkes, J. B., 2009, "The role of inertial cavitation in acoustic droplet vaporization," IEEE Trans. Ultrason. Ferroelectr. Freq. Control, **56**(5), pp. 1006–1017.

[59] Asami, R., Azuma, T., and Kawabata, K. -i., 2009, "Fluorocarbon droplets as next generation contrast agents - their behavior under 1 #x2013;3 MHz ultrasound," Ultrasonics Symposium (IUS), 2009 IEEE International, pp. 1294 –1297.

[60] Díaz-López, R., Tsapis, N., and Fattal, E., 2009, "Liquid Perfluorocarbons as Contrast Agents for Ultrasonography and 19F-MRI," Pharm. Res., **27**(1), pp. 1–16.

[61] Rapoport, N., Nam, K.-H., Gupta, R., Gao, Z., Mohan, P., Payne, A., Todd, N., Liu, X., Kim, T., Shea, J., Scaife, C., Parker, D. L., Jeong, E.-K., and Kennedy, A. M., 2011, "Ultrasound-mediated tumor imaging and nanotherapy using drug loaded, block copolymer stabilized perfluorocarbon nanoemulsions," J. Controlled Release, **153**(1), pp. 4–15.

[62] Schwarz, R., Schuurmans, M., Seelig, J., and Künnecke, B., 1999, "19F-MRI of perfluorononane as a novel contrast modality for gastrointestinal imaging," Magn. Reson. Med., **41**(1), pp. 80–86.

[63] Wilson, K., Homan, K., and Emelianov, S., 2012, "Biomedical photoacoustics beyond thermal expansion using triggered nanodroplet vaporization for contrast-enhanced imaging," Nat Commun, **3**, p. 618.

[64] Hannah, A., Luke, G., Wilson, K., Homan, K., and Emelianov, S., 2014, "Indocyanine Green-Loaded Photoacoustic Nanodroplets: Dual Contrast Nanoconstructs for Enhanced Photoacoustic and Ultrasound Imaging," ACS Nano, **8**(1), pp. 250–259.

[65] Reznik, N., Williams, R., and Burns, P. N., 2011, "Investigation of Vaporized Submicron Perfluorocarbon Droplets as an Ultrasound Contrast Agent," Ultrasound Med. Biol., **37**(8), pp. 1271–1279.

[66] Williams, R., Wright, C., Cherin, E., Reznik, N., Lee, M., Gorelikov, I., Foster, F. S., Matsuura, N., and Burns, P. N., 2013, "Characterization of Submicron Phase-change Perfluorocarbon Droplets for Extravascular Ultrasound Imaging of Cancer," Ultrasound Med. Biol., **39**(3), pp. 475–489.

[67] Rapoport, N. Y., Kennedy, A. M., Shea, J. E., Scaife, C. L., and Nam, K.-H., 2009, "Controlled and targeted tumor chemotherapy by ultrasound-activated nanoemulsions/microbubbles," J. Controlled Release, **138**(3), pp. 268–276.

[68] Sarker, D. K., 2005, "Engineering of Nanoemulsions for Drug Delivery," Curr. Drug Deliv., **2**(4), pp. 297–310.

[69] Rapoport, N., 2012, "Phase-shift, stimuli-responsive perfluorocarbon nanodroplets for drug delivery to cancer," Wiley Interdiscip. Rev. Nanomed. Nanobiotechnol., **4**(5), pp. 492–510.

[70] Fang, J.-Y., Hung, C.-F., Hua, S.-C., and Hwang, T.-L., 2009, "Acoustically active perfluorocarbon nanoemulsions as drug delivery carriers for camptothecin: Drug release and cytotoxicity against cancer cells," Ultrasonics, **49**(1), pp. 39–46.

[71] Krafft, M. P., 2001, "Fluorocarbons and fluorinated amphiphiles in drug delivery and biomedical research," Adv. Drug Deliv. Rev., **47**(2–3), pp. 209–228.

[72] Zhang, P., Kopechek, J. A., and Porter, T. M., 2013, "The impact of vaporized nanoemulsions on ultrasound-mediated ablation," J. Ther. Ultrasound, **1**, p. 2.

[73] Zhang, M., Fabiilli, M. L., Haworth, K. J., Padilla, F., Swanson, S. D., Kripfgans, O. D., Carson, P. L., and Fowlkes, J. B., 2011, "Acoustic Droplet Vaporization for Enhancement of Thermal Ablation by High Intensity Focused Ultrasound," Acad. Radiol., **18**(9), pp. 1123–1132.

[74] Zhang, P., and Porter, T., 2010, "An in vitro study of a phase-shift nanoemulsion: A potential nucleation agent for bubble-enhanced HIFU tumor ablation," Ultrasound Med Biol, **36**(11), pp. 1856–1866.

[75] Kopechek, J. A., Zhang, P., Burgess, M. T., and Porter, T. M., 2012, "Synthesis of Phase-shift Nanoemulsions with Narrow Size Distributions for Acoustic Droplet Vaporization and Bubble-enhanced Ultrasound-mediated Ablation," J. Vis. Exp., (67).

[76] Martin, A. L., Seo, M., Williams, R., Belayneh, G., Foster, F. S., and Matsuura, N., 2012, "Intracellular Growth of Nanoscale Perfluorocarbon Droplets for Enhanced Ultrasound-Induced Phase-Change Conversion," Ultrasound Med. Biol., **38**(10), pp. 1799–1810.

[77] Kopechek, J., Park, E., Mei, C.-S., McDannold, N., and Porter, T., 2013, "Accumulation of Phase-Shift Nanoemulsions to Enhance MR-Guided Ultrasound-Mediated Tumor Ablation In Vivo," J. Healthc. Eng., **4**(1), pp. 109–126.

[78] Suslick, K. S., and Grinstaff, M. W., 1990, "Protein microencapsulation of nonaqueous liquids," J. Am. Chem. Soc., **112**(21), pp. 7807–7809.

[79] Kripfgans, O. D., Fowlkes, J. B., Miller, D. L., Eldevik, O. P., and Carson, P. L., 2000, "Acoustic droplet vaporization for therapeutic and diagnostic applications," Ultrasound Med. Biol., **26**(7), pp. 1177–1189.

[80] Martz, T. D., Sheeran, P. S., Bardin, D., Lee, A. P., and Dayton, P. A., "Precision Manufacture of Phase-Change Perfluorocarbon Droplets Using Microfluidics," Ultrasound Med. Biol., (0).

[81] Nishihara, M., Imai, K., and Yokoyama, M., 2009, "Preparation of Perfluorocarbon/Fluoroalkyl Polymer Nanodroplets for Cancer-targeted Ultrasound Contrast Agents," Chem. Lett., **38**(6), pp. 556–557.

[82] Pitt, W. G., Singh, R. N., Perez, K. X., Husseini, G. A., and Jack, D. R., 2014, "Phase transitions of perfluorocarbon nanoemulsion induced with ultrasound: A mathematical model," Ultrason. Sonochem., **21**(2), pp. 879–891.

[83] Shpak, O., Verweij, M., Vos, H. J., Jong, N. de, Lohse, D., and Versluis, M., 2014, "Acoustic droplet vaporization is initiated by superharmonic focusing," Proc. Natl. Acad. Sci., **111**(5), pp. 1697–1702.

[84] Reznik, N., Shpak, O., Gelderblom, E. C., Williams, R., de Jong, N., Versluis, M., and Burns, P. N., 2013, "The efficiency and stability of bubble formation by acoustic vaporization of submicron perfluorocarbon droplets," Ultrasonics, **53**(7), pp. 1368–1376.

[85] Kawabata, K., Sugita, N., Yoshikawa, H., Azuma, T., and Umemura, S., 2005, "Nanoparticles with Multiple Perfluorocarbons for Controllable Ultrasonically Induced Phase Shifting," Jpn. J. Appl. Phys., **44**, pp. 4548–4552.

[86] Sheeran, P. S., Wong, V. P., Luois, S., McFarland, R. J., Ross, W. D., Feingold, S., Matsunaga, T. O., and Dayton, P. A., 2011, "Decafluorobutane as a Phase-Change Contrast Agent for Low-Energy Extravascular Ultrasonic Imaging," Ultrasound Med. Biol., **37**(9), pp. 1518–1530.

[87] Noguez, C., and Garzón, I. L., 2009, "Optically active metal nanoparticles," Chem. Soc. Rev., **38**(3), pp. 757–771.

[88] Pissuwan, D., Valenzuela, S. M., and Cortie, M. B., 2006, "Therapeutic possibilities of plasmonically heated gold nanoparticles," Trends Biotechnol., **24**(2), pp. 62–67.

[89] Park, J. I., Jagadeesan, D., Williams, R., Oakden, W., Chung, S., Stanisz, G. J., and Kumacheva, E., 2010, "Microbubbles Loaded with Nanoparticles: A Route to Multiple Imaging Modalities," ACS Nano, **4**(11), pp. 6579–6586.

[90] Strohm, E., Rui, M., Gorelikov, I., Matsuura, N., and Kolios, M., 2011, "Vaporization of perfluorocarbon droplets using optical irradiation," Biomed. Opt. Express, **2**(6), pp. 1432–1442.

[91] Wei, C., Lombardo, M., Larson-Smith, K., Pelivanov, I., Perez, C., Xia, J., Matula, T., Pozzo, D., and O'Donnell, M., 2014, "Nonlinear contrast enhancement in photoacoustic molecular imaging with gold nanosphere encapsulated nanoemulsions," Appl. Phys. Lett., **104**(3), p. 033701.

[92] Wei, C., Xia, J., Lombardo, M., Perez, C., Arnal, B., Larson-Smith, K., Pelivanov, I., Matula, T., Pozzo, L., and O?Donnell, M., 2014, "Laser-induced cavitation in nanoemulsion with gold nanospheres for blood clot disruption: in vitro results," Opt. Lett., **39**(9), pp. 2599–2602.

[93] Dove, J. D., Mountford, P. A., Murray, T. W., and Borden, M. A., 2014, "Engineering optically triggered droplets for photoacoustic imaging and therapy," Biomed. Opt. Express, **5**(12), p. 4417.

[94] Sheeran, P. S., Luois, S., Dayton, P. A., and Matsunaga, T. O., 2011, "Formulation and Acoustic Studies of a New Phase-Shift Agent for Diagnostic and Therapeutic Ultrasound," Langmuir, **27**(17), pp. 10412–10420.

[95] Sheeran, P. S., Luois, S., Matsunaga, T. O., and Dayton, P. A., 2011, "Submicron decafluorobutane phase-change contrast agents generated by microbubble condensation," Ultrasonics Symposium (IUS), 2011 IEEE International, pp. 636–639.

[96] Kim, S. H., and Franses, E. I., 2005, "New protocols for preparing dipalmitoylphosphatidylcholine dispersions and controlling surface tension and competitive adsorption with albumin at the air/aqueous interface," Colloids Surf. B Biointerfaces, **43**(3-4), pp. 256–266.

[97] Sheeran, P. S., Luois, S. H., Mullin, L. B., Matsunaga, T. O., and Dayton, P. A., 2012, "Design of ultrasonically-activatable nanoparticles using low boiling point perfluorocarbons," Biomaterials, **33**(11), pp. 3262–3269.

[98] Moyer, L. C., Timbie, K. F., Sheeran, P. S., Price, R. J., Miller, G. W., and Dayton, P. A., 2015, "High-intensity focused ultrasound ablation enhancement in vivo via phase-shift nanodroplets compared to microbubbles," J. Ther. Ultrasound, **3**(1), p. 7.

[99] Felizardo, M., Martins, R. C., Ramos, A. R., Morlat, T., Girard, T. A., Giuliani, F., and Marques, J. G., 2008, "New acoustic instrumentation for the SIMPLE superheated droplet detector," Nucl. Instrum. Methods Phys. Res. Sect. Accel. Spectrometers Detect. Assoc. Equip., **589**(1), pp. 72–84.

[100] Boukhira, N., Boussaroque, I., Gornea, R., Di Marco, M., Lessard, L., Pagé, V., Vinet, J., and Zacek, V., 2000, "Suitability of superheated droplet detectors for dark matter search," Astropart. Phys., **14**(3), pp. 227–237.

[101] Apfel, R. E., 1979, "The superheated drop detector," Nucl. Instrum. Methods, **162**(1–3), pp. 603–608.

[102] Hamel, L. A., Lessard, L., Rainville, L., Zacek, V., and Sur, B., 1997, "A superheated droplet detector for dark matter search," Nucl. Instrum. Methods Phys. Res. Sect. Accel. Spectrometers Detect. Assoc. Equip., **388**(1–2), pp. 91–99.

The laws of thermodynamics, as empirically determined, express the approximate and probable behavior of systems of a great number of particles, or, more precisely, they express the laws of mechanics for such systems as they appear to beings who have not the fineness of perception to enable them to appreciate quantities of the order of magnitude of those which relate to single particles, and who cannot repeat their experiments often enough to obtain any but the most probable results.

- J. Willard Gibbs (1902)

Chapter 2

Condensation and Vaporization of Pure Fluorocarbons

2.1 Introduction

The pressures required for the condensation of lipid-coated fluorocarbon microbubbles have not been documented. Microbubble condensed nanodrops have been vaporized with acoustic and optical energy.[1] Their ultrasound and optical fluence intensities have been recorded.[2,3] There has not been an attempt to predict the conditions required for microbubble condensation. During the invention of microbubble condensed nanodrops, an attempt to predict the vaporization temperatures for multiple fluorocarbon droplets of different sizes was made based on the Laplace pressure and the Antoine vapor pressure equation.[4] This study predicted low-boiling point nanoscale fluorocarbon droplets should vaporize around physiological temperature (37 °C), and yet somehow they have been shown to be stable *in vivo*.[5] On top of being superheated, condensed nanoemulsions have required additional acoustic and optical energy for vaporization.[3,6] The molecular mechanism responsible for the superheated droplet stabilities

observed in these studies needs to be understood so condensed nanoemulsions can be better applied to current theranostic applications.

This chapter predicts the phase-change conditions of pure fluorocarbon droplets using superstate molecular thermodynamics for macroscopic materials. Initially, classical thermodynamic phase transitions are studied from an intermolecular perspective to provide a fundamental understanding of traditional macroscopic condensation and vaporization. Gaps pertaining to supersaturated and superheated phase transitions are identified in classical thermodynamics. The effect of droplet size on condensation and vaporization is examined to confirm previous findings.[1] Secondly, the homogeneous nucleation processes of supersaturated bubbles and superheated droplets are examined to better understand supercooled and superheated metastability, respectively. Finally, the kinetic limits of supersaturation and superheat are defined based on previously reported macroscopic methods. The derivations in this chapter are based on Carey[2] and Davies[3] calculations for supersaturated and superheated homogeneous nucleation. For this work, homogeneous condensation takes place within a supersaturated microbubble, and homogeneous vaporization occurs within a superheated nanodrop.

2.2 Classical Phase-Shift Thermodynamics

2.2.1 Intermolecular Forces

Condensation and vaporization are phase transitions governed by the stability of molecules existing amidst two preferred physical states, liquid and gas. Gas is the state of matter in which the molecular orientation provides no constant shape or volume, where as a liquid retains constant volume with no constant shape. In order to move molecules from a more chaotic (gaseous) and separated state to a more confined and organized (liquid) state the kinetic energy of the molecules

must be reduced. Alternatively, to move from a liquid to a gas the kinetic energy must be increased. Decreasing molecular kinetic energy allows intermolecular attraction forces to dominate. Intermolecular attraction and repulsion can be described by the Lennard-Jones 6-12 potential (ϕ_{LJ}) as:

$$\Phi_{LJ} = 4\varepsilon\left[\left(\frac{r_o}{r}\right)^{12} - \left(\frac{r_o}{r}\right)^{6}\right] \tag{2.1}$$

with ε being the depth of the molecular potential energy well, r being the distance between the center of molecules and r_o being the equilibrium distance between molecules where the potential reaches a minimum.[2] This potential can be seen in Figure 1A.[4]

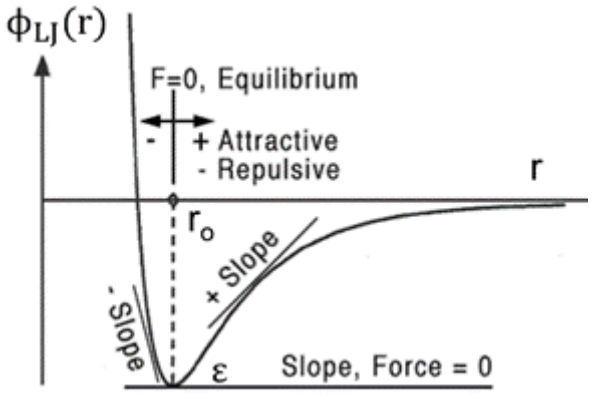

Figure 2.1. Lennard-Jones 6-12 potential diagram.[9]

The Lennard-Jones potential illustrates the potential energy between molecules and originates from the electrostatic interactions between them. This potential is predominantly a combination of hard sphere repulsion and an attractive long-range potential.[5] The attractive long-range potential comes from the van der Waals attraction forces. To elaborate, the van der Waals forces include the force between two permanent dipoles (Keesom energy), a permanent dipole and an induced dipole (Debye energy) and between two induced dipoles (London dispersion energy).[5] Note that the 6-12 potential (Equation 2.1) only takes into account London dispersion

energy. Taking away or overcoming any attraction forces drive molecules apart indefinitely directing the matter into an infinitely disperse gaseous state. Conversely, by increasing the attractive potential and changing the Lennard-Jones potential well, molecules can be forced closer together in a more condensed state. Molecules favor a state of minimum energy along with the ability to move with a maximum number of degrees of freedom.[6] This behavior is why molecules want to disperse without the presence of attractive forces. Changing the energy of a system (temperature and pressure) can manipulate kinetic energy relative to van der Waals potential energy and dictate their state of matter.

2.2.2 Macroscopic Phase Change Behavior

The Lennard-Jones potential describes how molecules interact at a given distance. It does not explain what happens to a material when its molecules are set into motion by thermal (kinetic) energy. To clarify how intermolecular forces dictate the state of matter of a material, statistical and classical phase-change thermodynamics will be reviewed. Starting with statistical thermodynamics, a relation between pressure (P), temperature (T) and a materials phase can be found from the van der Waals equation of state:

$$P = k_B T \left(\frac{\partial \ln Q}{\partial V} \right)_{T,N} \tag{2.2}$$

where k_B is the Boltzmann constant, V is volume, N is the number of moles and lnQ is the canonical partition function as described by Carey[2]. The canonical partition function takes into account all possible molecular orientations (canonical ensemble) that can exist when a system is in thermal equilibrium.[7]

Upon combining the van der Waals equation of state with the canonical partition function and normalizing by the number of moles (N) and the molecular mass ($\overline{M}$), the pressure of a system is related to temperature and volume through:

$$P = \frac{BT}{v - b_v} - \frac{a_v}{v^2} \tag{2.3}$$

where B is the universal gas constant ($=N_A k_B/\overline{M}$, N_A being Avogadro's number (6.022×10^{23} mol^{-1})), v is the specific volume and a_v and b_v are mass-specific van der Waals constants equal to:

$$a_v = \frac{27(\overline{B}/\overline{M})^2 T_C^2}{64 P_C} \tag{2.4a}$$

$$b_v = \frac{(B/\overline{M})T_C}{8P_C} \tag{2.4b}$$

Equations 2.4a&b both have new pressure and temperature terms (P_C and T_C) which are the critical pressure and temperature terms, respectively. The critical temperature is the temperature at which no amount of a gas can exist in the liquid phase unless at its critical pressure.[8] Combining 2.3 with 2.4 gives:

$$P_r = \frac{8T_r}{3v_r - 1} - \frac{3}{v_r^2} \tag{2.5}$$

which is the reduced equation of state where T_r, P_r and v_r are the reduced temperature, pressure and specific volume respectively. A reduced property is the measure of the current property over the critical property (i.e. $T_r = T/T_c$). This statistical thermodynamic relation between pressure, temperature and specific volume can be examined in Figure 2.2. Upon reviewing the van der Waals equation of state plot, it can be seen for temperatures below the critical temperature (T_r=0.8 and 0.9) that there exists a local minimum and maximum for the isotherms at a given reduced pressure (P_r). This means that at a constant reduced pressure of P_r = 0.4 and a reduced temperature

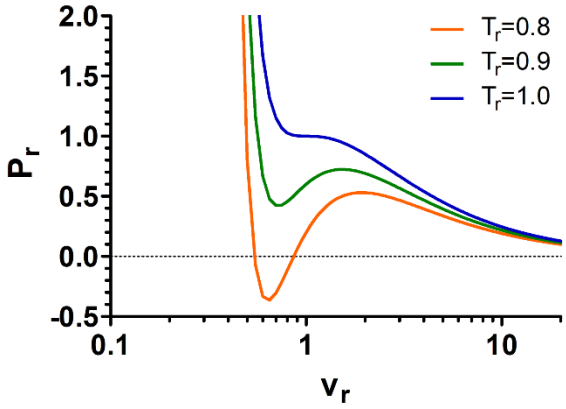

Figure 2.2. Plot presenting the relationship between reduced pressure, specific volume and temperature based on the van der Waals equation of state (Eqn. 2.8).

of $T_r = 0.8$, that the reduced specific volume of a substance can simultaneously be $v_r = 0.51$, 1.25 and 3.90 indicating the coexistence of multiple physical states. Statistical thermodynamics treats the coexistence of the multiple phases as a problem of probability allowing for the existence of two phases at constant temperature and pressure, whereas classical thermodynamics does not.

In classical thermodynamics, it is dictated that in order for a substance to undergo a phase transition it must transition through a state of equilibrium where its temperature, pressure and chemical potential are equal for both the liquid and gas phases.[9] Since the existence of two phases is not permitted and the liquid and gas properties of the substance are equivalent, the only way to reduce pressure or increase temperature is to undergo a change in phase. This means that there must be a line of constant reduced pressure to travel from the liquid to gas state as specific volume (v_r) is increased. Knowing that statistical thermodynamics treats the multiphase region as a function of probability and that reduced pressure is constant between the liquid and gas phase, an isobaric line can be drawn from the liquid to gas phase at a reduced pressure that permits the equivalent probability of the liquid and gas phases existing. To elaborate, the area below the isobaric phase transition line and above the van der Waals equation of state local minimum must

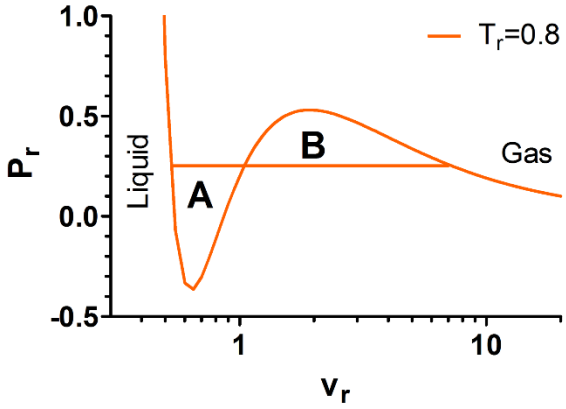

Figure 2.3. Plot representing the isobaric line for phase transition from a liquid to a gas based on classical thermodynamics. The regions A and B are equivalent and represent the probability of being in the liquid and gas phase, respectively and are predicted by statistical thermodynamics.

be equivalent to the area above the isobaric line and below the equation of state local maximum. This criteria can been visualized in Figure 2.3 where the area of region A must equal the area of region B. Constant pressure lines across the multiphase region from a liquid to gas state for a range of temperatures are used by classical theory to construct saturation curves. Traditional saturation curves represent the evaporation and condensation conditions for various liquids and gases. Figure 2.2 has been reconstructed with isobaric lines at the equilibrium phase transition

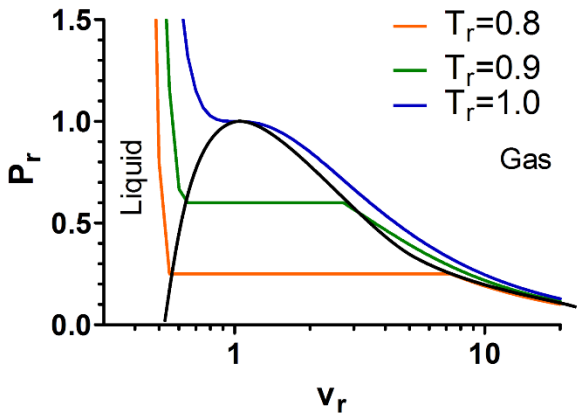

Figure 2.4. Pressure-specific volume phase diagram depicting how reduced temperature isotherms are used to construct a saturation curve (black line).

pressures to build a saturation curve (Fig. 2.4). Again this curve represents the conditions for which a substance condenses or vaporizes and neglects the possibility of multiphase existence. A traditional liquid-gas phase diagram (Fig. 2.5) has been constructed from the saturation curve to help depict how classical thermodynamics dictates the phase of a substance. It is important to reiterate that this work is primarily interested in the multiphase phenomena occurring within the saturation curve that classic theory ignores. Studies have shown stability of nanodrops at high degrees of superheat which could be due to a heightened pressure presented at the gas-liquid interface or the stable coexistence of liquid and gas during droplet heating.

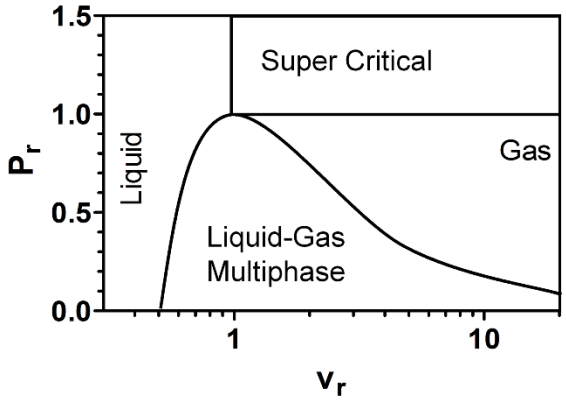

Figure 2.5. Reduced pressure-specific volume liquid-gas phase diagram for constant temperature based on classic thermodynamics.

2.2.3 The Effect of Laplace Pressure on Condensation and Vaporization

The previously covered phase-transition properties were reported for bulk macroscopic materials and did not take into account size effects associated with a nanoscale droplet. At small curved interfaces surface tension creates a heightened pressure inside the radius of curvature known as

the Laplace pressure. For a spherical interface of radius R with an interfacial surface tension γ the Laplace pressure is:

$$\Delta P = P_{in} - P_{out} = \frac{2\gamma}{R} \tag{2.6}$$

with P_{in} and P_{out} being the pressures inside and outside of a microbubble or droplet. An optimal droplet for extravasation is on the order of 100-700 nm[10] in diameter, which corresponds to a microbubble for condensation of roughly 520-3640 nm in diameter. This size range of gas microbubbles with a interfacial surface tension of ~25 mN m^{-1}[11] provides a heightened Laplace pressure ranging from 27.5-192 kPa. Adding these pressures to atmospheric (101.325 kPa) provides that a microbubble core is subjected to a 27 to 190% increase in pressure at STP. A perfluorobutane C_4F_{10} macroscopic phase diagram[12] is presented in Figure 2.6 along with predicted condensation pressures based on the Young-Laplace equation (Eqn. 2.8). C_4F_{10} is the most common material used in the core of microbubble condensed droplets.

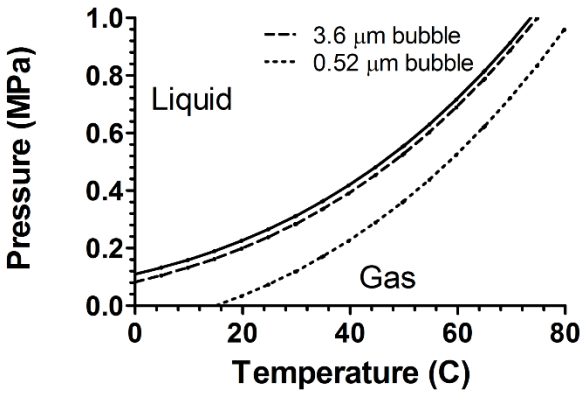

Figure 2.6. Gas-liquid phase diagram for C_4F_{10} (solid black line). The theoretical condensation pressure for 3.6 and 0.52 μm diameter bubbles with an interfacial surface tension of 25 mN m^{-1}.

A decrease in the additional pressure required for microbubble condensation results in the increase of additional temperature needed for vaporization which could be the reason for the

heightened superheat stability of condensed droplet solutions. To accurately determine the degree of superheat required for droplet vaporization, the vapor pressure of C_4F_{10} liquid in the core needs to be determined from the Antoine vapor equation. The vaporization temperature of a condensed nanodrop is determined from the Antoine equation[13] and the Laplace pressure to be:

$$T = \frac{B}{A - \log_{10}\left(P_{out} + \frac{2\gamma}{R}\right)} - C \tag{2.7}$$

where *A*, *B* and *C* are the dimensionless experimental material constants for C_4F_{10} determined from Brown and Mears[14] to be 4.1425, 982.586 and -33.624, respectively. Additionally, perfluoropropane (C_3F_8) was examined as a droplet core material with Antoine constants of 4.08856, 842.613 and -30.023, respectively.[15] The predicted vaporization temperatures of C_4F_{10} and C_3F_8 droplets are provided in Figure 2.7 for droplets 0.1 to 0.8 µm in diameter (size of droplets created from 0.5 to 4.0 µm diameter bubbles assuming no dissolution during condensation).

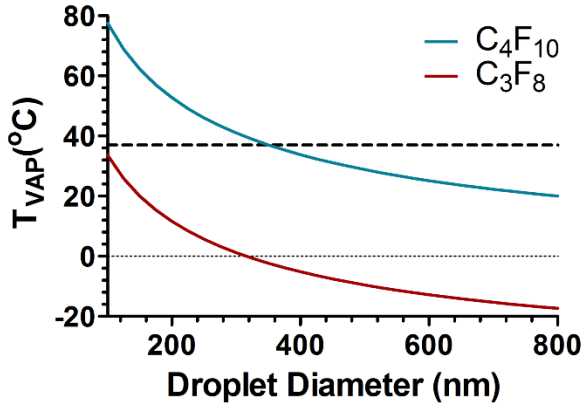

Figure 2.7. The predicted droplet vaporization temperature for C_4F_{10} (blue) and C_3F_8 (red) droplets with an interfacial surface tension 25 mN m^{-1}. The dotted and dashed lines represent freezing (0 °C) and physiological temperature (37 °C), respectively.

These predicted temperatures show that only C_4F_{10} drops are stable at physiological temperature when 300 nm in diameter or smaller and that C_3F_8 drops are not stable at any size over

100 nm. Again, researchers have confirmed stability of C_4F_{10} and C_3F_8 nanodrops at or above 37 °C.[16,17] A potential reasoning for the discrepancy in superheat stability between the Antoine equation predictions and experimental observations is that the surface tension is higher for a surfactant stabilized liquid-liquid interface than assumed (>25 mN m^{-1}). If surface tension and Laplace pressure was high enough to permit droplet stability at 37 °C, then the droplet could be subject to expedited dissolution into the surrounding liquid. Although the Laplace pressure could be responsible for droplet superheat stability, it is unlikely. It is most probable that there exists a separate mechanism in combination with the Laplace pressure acting to stabilize these droplets.

2.3 Condensation of a Supersaturated Pure Fluorocarbon

2.3.1 Homogeneous Nucleation in a Supersaturated Fluorocarbon Gas

Condensation is the change in the physical state of matter from a gas phase into a liquid phase.[18] On the molecular scale, condensation occurs at constant temperature when the gas pressure is increased so that molecular energy is reduced allowing for intermolecular attraction forces to dominate. The attraction between gas molecules causes the formation of tiny molecular clusters of the material in the form of a liquid phase. The most common example of condensation is the formation of rain, which is created when the local atmospheric pressure is increased so that water vapor in the air begins to form molecular liquid clusters.[19] Once these liquid clusters are large enough for gravity to affect them, they fall to the earth as rain. The initial liquid clusters, formed from a few molecules, are the condensation nuclei and are the origin of the gas-to-liquid phase transition for water vapor. Dust, airborne bacteria and other particulates can facilitate nucleation and cause the condensation of water vapor closer to saturation pressure.[20] In the absence of imperfections and particulates, condensation cannot occur until sufficient supersaturation

pressures, capable of forcing the liquid phase, are met. Nucleation originating on the surface of a particle or imperfection is known as heterogeneous nucleation, whereas nucleation occurring uniformly in a material is homogeneous nucleation.

Nucleation of the liquid phase in a gas is governed by the energy required to build that nucleus into a sufficient size so that condensation of the entire material can take place. The energy required to build a nucleus is determined from the free energy barrier associated with expanding a liquid-gas interface. To elaborate, a nucleus can only grow if the free energy barrier of expanding the surface area is in balance with the intermolecular attraction energy. The free energy barrier is heavily dependent upon the ratio of nucleate surface area to amount of nucleate material. The smaller a nucleate, the greater the surface area to volume ratio and free energy required to expand the interface. In heterogeneous nucleation, nucleates begin to grow on particles and impurities that are relatively large with respect to individual molecules, minimizing the surface area-to-volume ratio and increasing the probability of nucleation growth. Without impurities to lower the interfacial energy barrier, nucleates have to build molecule by molecule (homogeneous nucleation) and can only grow to cause condensation if the interfacial energy barrier is overcome.

Condensation pressures of pure C_4F_{10} microbubbles have not yet been measured. Condensation pressures near that of the bulk, or predicted by the Laplace pressure (Fig. 2.6), would indicate heterogeneous nucleation. On the other hand, heightened condensation pressures would be indicative of homogeneous nucleation. The C_4F_{10} purchased for these experiments is reported to be 99% pure and free of particulates. Prior to deriving supersaturation pressures of C_4F_{10}, a clear depiction of the supersaturated system being analyzed is needed. Figure 2.8 provides a schematic of a pure PFC microbubble undergoing homogeneous nucleation while subject to a Laplace pressure. The heightened Laplace pressure inside the microbubble would work in favor

of growing liquid nucleates. Like a microbubble suspended in water, a PFC droplet formed in gaseous PFC also has an interfacial surface tension (previously reported to be ~12 mN m^{-1}).[21]

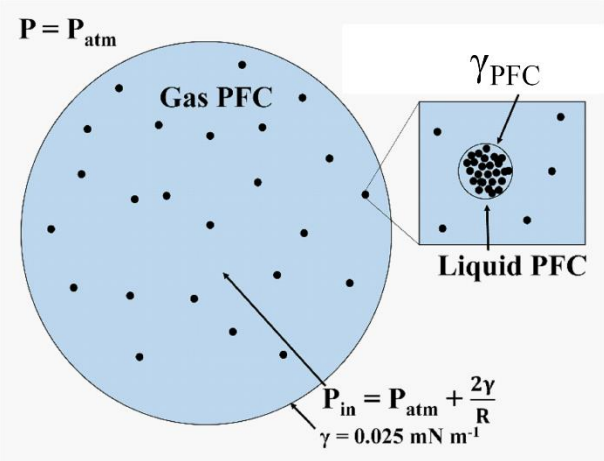

Figure 2.8. Cartoon depicting homogeneous nucleation of the liquid phase in a PFC lipid stabilized gas microbubble.

To determine the theoretical condensation pressure for a PFC microbubble undergoing supersaturated homogeneous nucleation, the energy required to form a liquid nucleate must be quantified. For a gas condensing into a liquid, the temperature and chemical potential of the vapor and liquid PFC must be equivalent (T_v=T_l, $\mu_{sat,v}$=$\mu_{sat,l}$). The pressure inside of the liquid embryo at equilibrium (P_{le}) can be defined as:

$$P_{le} = P_v + \frac{2\gamma_{PFC}}{R} \tag{2.8}$$

where P_v is the vapor pressure of gas PFC in the microbubble core and is equivalent to P_{in} in Equation 2.6. The fluorocarbon liquid-gas interfacial surface tension is defined by γ_{PFC} and is dependent of temperature as seen in Table 2.1. R_e represents the radius of the liquid embryo nucleate in equilibrium. The Gibbs-Duhem equation is used here to provide a relation between chemical potential and pressure during condensation:

$$d\mu = -sdT + vdP \tag{2.9}$$

Knowing temperature is constant provides:

$$\mu - \mu_{sat} = \int_{P_{sat}(T_v)}^{P} v dP \tag{2.10}$$

Combining 2.13 with the ideal gas law gives:

$$\mu_v = \mu_{sat,v} + BT_v \ln\left[\frac{P_{in}}{P_{sat}(T_v)}\right] \tag{2.11}$$

for the chemical potential of the vapor phase (μ_v). Here, $\mu_{sat,v}$ is the chemical potential at saturation, T_v is the vapor temperature (temperature of the microbubble) and $P_{sat}(T_v)$ is the saturation pressure of the material. The chemical potential of the liquid phase (μ_l) is:

$$\mu_l = \mu_{sat,l} + v_l\left[P_{le} - P_{sat}(T_v)\right] \tag{2.12}$$

where $\mu_{sat,l}$ is the chemical potential at saturation and v_l is the specific volume of the liquid phase. With the saturation chemical potential of the vapor and liquid phases being equivalent ($\mu_{sat,l} = \mu_{sat,v}$) and knowing that $\mu_v = \mu_l$ during condensation, 2.11 and 2.12 can be combined with 2.8 to give:

$$P_{in} = P_{sat}(T_v)\exp\left\{\frac{v_l\left[P_{in} - P_{sat}(T_v) + 2\gamma_{PFC}/R_e\right]}{BT_v}\right\} \tag{2.13}$$

Note that $\mu_v = \mu_l$ only during a phase transformation process. Equation 2.13 can be rearranged to solve for the equilibrium radius of liquid nucleate embryo in a supersaturated microbubble:

$$R_e = \frac{2\gamma_{PFC}}{(BT_v/v_l)\ln[P_{in}/P_{sat}(T_v)] - P_{in} + P_{sat}(T_v)} \tag{2.14}$$

This radius is of the size for which a liquid nucleate needs to form to create an embryo large enough to grow and cause condensation of the entire supersaturated vapor at temperature T_v and pressure P_{in}.

Temperature [K]	C_3F_8 Surface Tension (γ_{PFC})[N m^{-1}]	C_3F_8 Liquid Density (ρ_L)[kg m^{-3}]	C_4F_{10} γ_{PFC}	C_4F_{10} ρ_L	C_5F_{12} γ_{PFC}	C_5F_{12} ρ_L
230	0.0113	1636.2				
240	0.0101	1597.2				
250	0.00893	1556.7	0.0122	1656.1		
260	0.0078	1514.3	0.0111	1626.1	0.0134	1740.9
270	0.00669	1469.4	0.0101	1594.8	0.0124	1708.6
280	0.00562	1421.5	0.00902	1561.8	0.0114	1675.8
290	0.00459	1369.6	0.008	1527	0.0104	1642.1
300	0.00359	1312.4	0.00701	1490	0.00949	1607.4
310	0.00264	1247.8	0.00604	1450.4	0.00856	1571.7
320	0.00175	1171.8	0.0051	1407.5	0.00764	1534.5
330	0.000941	1075.3	0.00418	1360.5	0.00673	1495.6
340	0.000247	923	0.0033	1308.1	0.00585	1454.6
350			0.00246	1248.1	0.00499	1411
360			0.00167	1176.5	0.00416	1364.2
370					0.00335	1313
380					0.00257	1256
390					0.00183	1190.3
400					0.00114	1110.4
410					0.00051	1002.8

Table 2.1. Surface tension and liquid densities for C_3F_8, C_4F_{10} and C_5F_{12} ranging from 230 to 410 K.[22]

The energy associated with forming liquid embryo in a supersaturated gas is described through the free energy of formation by Davies[3] to be:

$$\Delta G = \frac{1}{v_l}\left(\frac{4\pi R^3}{3}\right)\left(\mu_l - \mu_v\right) + 4\pi R^2 \gamma_{PFC} \tag{2.15}$$

This energy is the energy balance between liquefying the volume of the embryo and expanding the embryos interfacial area. Combining 2.15 with 2.11 and 2.12 provides the following relation between liquid embryo radius and the Gibbs free energy at the bulk saturation pressure (265 kPa) at constant room temperature (25 °C) in Figure 2.9. Note that although the hydrostatic and ambient

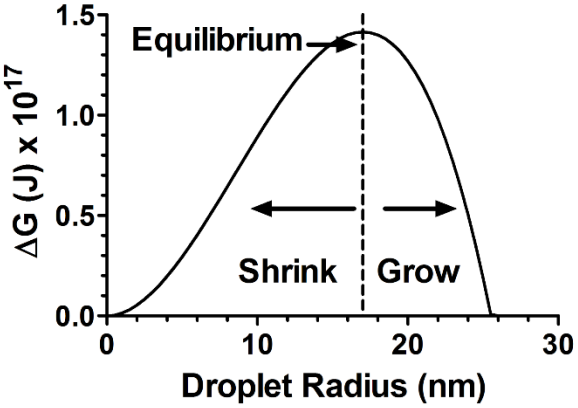

Figure 2.9. Free energy barrier for C_4F_{10} droplet formation in a supersaturated gas microbubble at saturation pressure (265 kPa at 25 °C). The free energy maximum represents the energy required to form a droplet of sufficient size for condensation of the entire microbubble.

pressure is 265 kPa, the vapor pressure inside the bubble is 290 kPa due to the gas-water surface tension (γ=0.025 N m^{-1}), and the pressure inside the droplet nucleate is even higher due to the liquid-gas PFC surface tension. The radius for which the free energy is at a maximum is the equilibrium radius (R_e, Eqn. 2.14), and any droplet formed smaller than that radius will shrink due to the positive slope of the free energy barrier, whereas larger droplets will grow because of the negative slope. The free energy at the equilibrium radius is the free energy of formation required to onset condensation of the supersaturated microbubble and is determined by setting the derivative of 2.15 with respect to the radius equal to zero and solving for the radius (R_e). The derivative of 2.15 is:

$$\frac{d\Delta G}{dR} = \frac{4\pi R^2}{v_l}(\mu_l - \mu_v) + 8\pi R\gamma_{PFC} \tag{2.16}$$

which when set equal to zero provides an equilibrium radius of:

$$R_e = \frac{2v_l\gamma_{PFC}}{(\mu_v - \mu_l)} \tag{2.17}$$

which is equivalent to 2.14. Setting the chemical potentials of the gas and liquid phases equal for equilibrium ($\mu_l = \mu_v$) turns 2.15 into:

$$\Delta G_e = \frac{4\pi R_e^2 \gamma_{PFC}}{3} \tag{2.18}$$

This is the supersaturation point at which the difference in the liquid and gas chemical potentials ($\mu_l - \mu_v$) equates to the energy required to expand the liquid interfacial area in the gas phase. The critical size and energy required for liquid nucleation for condensation is described, but the condensation pressure of a pure gaseous PFC droplet has yet to be defined.

2.3.2 Supersaturation Limit

Equilibrium liquid embryo formation is not a sure thing; it is subject to probability just like everything else in nature. Now that the free energy barrier for condensation is known, the probability of forming a droplet in a supersaturated microbubble needs to be deduced to determine the spinodal pressure. To explore equilibrium probability, the kinetics of the molecules undergoing phase-change in the microbubble is reviewed. Inside the supersaturated microbubble, dependent on pressure, molecules are rapidly condensing and evaporating at the interface of the liquid nucleate. As pressure is increased above saturation, the ratio of molecules condensing to evaporating increases until a sufficient condensation flux is met and condensation of the bulk (microbubble) occurs. The pressure at which the condensation flux is large enough for the definite formation of an equilibrium embryo can be defined as the spinodal pressure, or the pressure at which two phases can exist stably.[22]

The number distribution of embryos at equilibrium depends on the number of molecules and is defined as:

$$N(n)_e = \rho(n)_v \exp\left\{-\frac{\Delta G(R)}{k_B T_v}\right\} \tag{2.19}$$

with $\rho(n)_v$ being the number of vapor molecules per unit volume. When the liquid embryo is at the equilibrium size, the removal of a molecule will cause the embryo to shrink. Conversely, the addition of a molecule to the nucleus will cause it to grow until the entire bubble condenses. Therefore, the equilibrium number distribution is presented as:

$$N(n)_e A(n) j(n)_c = N(n+1)_e A(n+1) j(n+1)_e \tag{2.20}$$

where A is the interfacial area of embryos with n or $n+1$ molecules, $j(n)_c$ is the number of molecules condensing and $j(n+1)_e$ is the number of molecules evaporating. Next, the number distribution for embryos not of the equilibrium size must be taken into account. The excess number of embryos is defined as:

$$J(n) = N(n)A(n)\, j(n)_c \left[\left(\frac{N(n)^*}{N(n)} \right) - \left(\frac{N(n+1)^*}{N(n+1)} \right) \right] \tag{2.21}$$

where $N(n)^*$ is the size distribution of nonequilibrium embryos forming. The rate of change in molecules for all embryos smaller than equilibrium with respect to time is:

$$\frac{\partial N(n)^*}{\partial t} = J(n-1) - J(n) \tag{2.22}$$

Note that $J(n-1)$ is the number of embryos of size $(n-1)$. Equation 2.22 can be rewritten as:

$$\frac{\partial N(n)^*}{\partial t} = -\frac{\partial J(n)}{\partial n} \tag{2.23}$$

Assuming steady state ($\partial N(n)^* / \partial t = 0$) provides that $\partial J(n) / \partial (n) = 0$ and therefore that $J(n)$ is constant (J). Again, embryos that form larger than R_e will grow rapidly, therefore only embryos smaller than equilibrium are of concern when examining the rate of embryo formation for all sizes. If the pressure is high enough, equilibrium embryo formation will be definite and the chance of forming an embryo of a different size will drop to zero ($N(n)^* = 0$ as $n = n_e$), where n_e is the number of molecules to form an equilibrium radius. Conversely, the number of

nonequilibrium embryos will approach the number of equilibrium embryos as the number of molecules present diminishes ($N(n)^* / N(n) \to 1 \text{ as } n \to 0$). Equation 2.21 can be integrated and rewritten as:

$$J = \left[\frac{N(n)^*}{N(n)} \right] \left\{ \int_{n=n}^{n=n_o} \left[N(n) A(n) j(n)_c \right]^{-1} dn \right\}^{-1} \tag{2.24}$$

where $n_o = n_e$ and $j(n)_c$ is assumed to be equivalent to $j(n_e)_c$ which is:

$$j(n_e)_c = \frac{P_{in}}{(2\pi m k_B T_v)^{1/2}} \tag{2.25}$$

with m being the mass of one molecule. To get 2.24 in terms of the droplet radius, the relation:

$$n = \frac{4\pi R^3}{3 m v_l} \tag{2.26}$$

can be differentiated to become:

$$dn = \frac{4\pi R^2}{m v_l} dR \tag{2.27}$$

Equations 2.19, 2.25 and 2.27 can be substituted into 2.24 to provide:

$$J = \left[\frac{\rho(n)_v P_{in} v_l m}{(2\pi m k_B T_v)^{1/2}} \right] \left\{ \int_0^{\infty} \exp\left[\frac{\Delta G(R)}{k_B T_v} \right] dR \right\}^{-1} \tag{2.28}$$

where the free energy for equilibrium radius formation is defined in 2.18. The net flux of droplet embryo formation required for the definite formation of an equilibrium nucleus is:

$$J = \left(\frac{\rho(n)_v P_{in} v_l}{k_B T_v} \right) \left(\frac{2\gamma_{PFC} m}{\pi} \right)^{1/2} \exp\left(\frac{-4\pi R_e^{\,2} \gamma_{PFC}}{3 k_B T_v} \right) \tag{2.29}$$

with R_e being defined in 2.14. Calculating 2.29 at the bulk saturation pressure (265 kPa) provides a net flux of 0 drops m^{-3} s^{-1}, indicating that even with an increased internal bubble pressure, the probability of nucleating is zero. This inability to nucleate is because of insufficient pressure. As

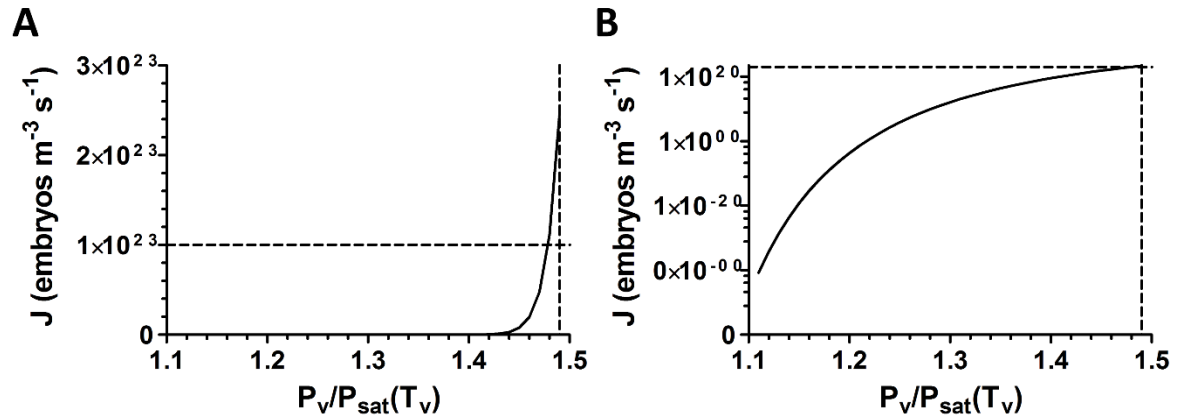

Figure 2.10. The liquid embryo formation rate versus supersaturation pressure plotted linearly (**A**) and logarithmically (**B**) for 25 °C. Dashed lines represent the 10^{23} m^{-3} s^{-1} nucleation rate experimentally determined to be sufficient for homogeneous condensation of a bubble.

pressure increases, the number of droplets formed increases, and the equilibrium droplet radius decreases, making it more likely to form an equilibrium droplet. At what pressure will there be a sufficient number of nuclei forming to create and equilibrium droplet? Figure 2.10 shows how J varies with supersaturation pressure for a PFC microbubble at 25 °C. Looking to the linear plot (Fig. 2.10A), it is difficult to determine the number of embryos forming at pressures near saturation. The logarithmic plot shows the nucleation rate varying from below 1 to ~10^{23} nucleates m^{-3} s^{-1}. From a pressure ratio ($P_{in}/P_{sat}(T_v)$) of roughly 1.42 to 1.5, the droplet formation rate rapidly increases indicating that a sufficient homogeneous nucleation condensation pressure lies near those ratios. With comparison to experimental findings, the sufficient liquid droplet formation flux for the bulk material is ~10^6 $m^{-3}s^{-1}$. [23] The volume of a microbubble (V) is on the order of 10^{-17} m^3. If it was desired to nucleate an equilibrium embryo in a microbubble within a reasonable amount of time (t=1 s), then the critical embryo formation flux (J=1/Vt) for condensation would need to be on the order of 10^{23} m^{-3} s^{-1}. This critical flux provides a hydraulic saturation pressure ratio of ~1.49, which equates to a pressure inside the bubble (P_{in}) of 420 kPa, and a hydrostatic pressure (P_{out}) of ~395 kPa. Figure 2.6 has been replotted with the predicted homogeneous condensation

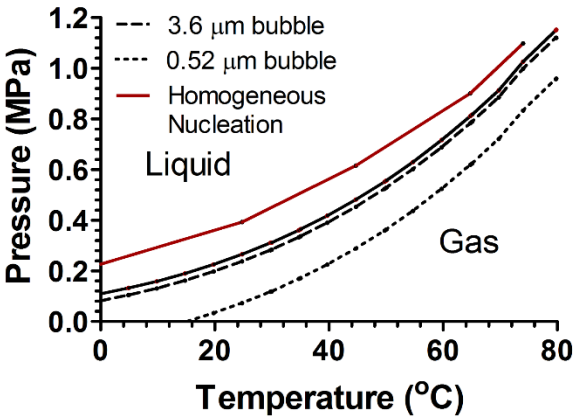

Figure 2.11. The condensation phase diagram for C_4F_{10} with the addition of the condensation pressures responsible for the homogeneous nucleation of the liquid phase in a supersaturated bubble approx. 4 μm in diameter.

curve for a 4 μm diameter bubble for comparison with bulk saturation and predicted Laplace pressures. The red line in Figure 2.11 represents the homogeneous nucleation condensation curve for a microbubble being subjected to a Laplace pressure (upper dashed line). This phase diagram supports the exceptional thermodynamic stability of pure supersaturated PFC gases.

2.4 Vaporization of a Superheated Pure Fluorocarbon

2.4.1 Homogeneous Nucleation in a Superheated Fluorocarbon Liquid

Microbubble condensed nanodrops are only useful for biomedical applications if they can be vaporized with minimal energy at 37 °C. The simplest way to gauge the energy required for vaporization is to experimentally determine the vaporization temperature through heating. Vaporizing a liquid is very similar to condensing a gas in that you must nucleate the new phase before the entire system will shift. Vaporization of a pure liquid can occur at the saturation temperature by evaporation due to heating or by nucleating the gas phase around particulates and impurities.[24] Like condensation, homogeneous nucleation of a pure (99%) PFC liquid will most

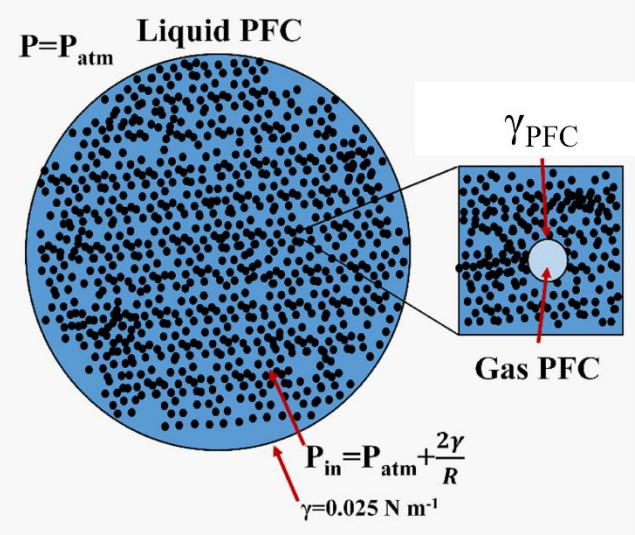

Figure 2.12. Cartoon depicting homogeneous nucleation of the gas phase in a PFC lipid stabilized liquid nanodrop.

likely occur at superheated temperatures. As temperature increases, the kinetic energy of the molecules can overcome the Lennard-Jones potential well (Eqn. 2.1).[2] Upon phase-change, the entropy of the system increases because the molecules can freely translate in the gaseous state (can mostly rotate and vibrate in liquid state).[25] This increase in entropy drops the free energy back down to a preferred minimum. Much like condensation, as a liquid is heated density fluctuations begin to occur and vapor embryos form.[26] Once a gas embryo forms at a large enough size (dependent of temperature and pressure) the vapor pocket rapidly grows and vaporization takes place.[2]

To determine the vaporization temperature of superheated pure PFC droplets, the homogeneous nucleation of vapor embryos is explored along with the kinetics of forming those gas nucleates. The homogeneous nucleation of a superheated liquid is depicted in Figure 2.12 to help in visualizing the phenomenon in this section. Like a supersaturated bubble, superheated fluorocarbon drops have a liquid-gas interfacial surface tension that is dependent of temperature (Table 2.1) that provides an increased Laplace pressure of:

$$P_{ve} = P_l + \frac{2\gamma_{PFC}}{R} \tag{2.30}$$

where P_l is equivalent to the pressure inside the droplet (P_{in}) from 2.6. As before, the chemical potential of the liquid and gas phase in equilibrium equate and provide a similar vapor pressure to 2.13:

$$P_{ve} = P_{sat}(T_l)\exp\left\{\frac{v_l\left[P_{ve} - P_{sat}(T_l) + 2\gamma_{PFC}/R_e\right]}{BT_l}\right\} \tag{2.31}$$

with T_l being the temperature of the superheated liquid. The vapor pressure for an equilibrium size gas embryo can be rearranged to solve for the equilibrium radius as:

$$R_e = \frac{2\gamma_{PFC}}{P_{sat}(T_l)\exp\left\{v_l\left[P_{in} - P_{sat}(T_l)\right]/BT_l\right\} - P_{in}} \tag{2.32}$$

The Gibbs free energy for forming an equilibrium size bubble embryo in a superheated liquid is equivalent to forming a droplet in a supersaturated gas (Eqn. 2.18). Combining 2.32 with 2.18 provides:

$$\Delta G_e = \frac{16\pi\gamma_{PFC}^{\ 3}}{3\left[P_{sat}(T_l)\exp\left\{v_l\left[P_{in} - P_{sat}(T_l)\right]/BT_l\right\} - P_{in}\right]^2} \tag{2.33}$$

Again, the energy required to form an equilibrium gas bubble of radius R_e is equivalent to the free energy barrier inhibiting the formation of the gas phase defined by:

$$\Delta G = \frac{1}{v_l}\left(\frac{4\pi R^3}{3}\right)\left(\mu_v - \mu_l\right) + 4\pi R^2\gamma_{PFC} \tag{2.34}$$

which is identical to 2.17, except that the chemical potentials have been switched. The Gibbs free energy barrier for a 0.8 μm superheated PFC droplet at 37 °C with an interfacial surface tension of 6 mN m^{-1} is plotted versus gas embryo radius in Figure 2.13. Here, the energy required to nucleate

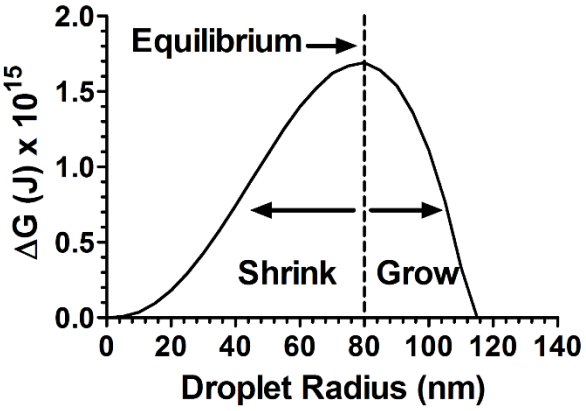

Figure 2.13. Free energy barrier for C_4F_{10} bubble formation in a superheated liquid nanodrop at physiological temperature (37 °C). The free energy maximum represents the energy required to form a droplet of sufficient size for vaporization of the entire condensed nanodrop.

an equilibrium bubble is high as compared to the energy required to grow a droplet for condensation (Fig. 2.9). Also, the equilibrium droplet is of similar size to the condensed droplet (400 nm radius). Due to an enhanced Laplace pressure on the liquid droplet as well as insufficient energy, formation of an equilibrium gas embryo at 37 °C is not probable.

2.4.2 Limit of Superheat

As mentioned when determining the kinetic limit of supersaturation, superheated vaporization of a condensed nanodrop is based on the likelihood of nucleating a vapor embryo of equilibrium size (R_e). The gas bubble formation flux is similar to 2.24 being:

$$J = \left[\frac{N(n)^*}{N(n)}\right]\left\{\int_{n=n}^{n=n_o}\left[N(n)A(n)\,j(n)_e\right]^{-1}dn\right\}^{-1} \tag{2.35}$$

with the flux of molecules evaporating from an equilibrium embryo being:

$$j(n)_e = j(n_e)_e = \frac{P_v}{(2\pi m k_B T_v)^{1/2}} \tag{2.36}$$

where n_e is the number of molecules for an equilibrium radius. Equation 2.35 can be solved similarly to 2.28 with a different conversion for *dn* to *dr* defined in 2.37.

$$dn = \frac{4\pi R^2}{3}\left(\frac{P_{ve}}{BT_l m}\right)\left(2 - \frac{P_{in}}{P_{ve}}\right)dr \tag{2.37}$$

Plugging 2.36 and 2.37 along with 2.19 into 2.35 provides the vapor embryo formation flux:

$$J = \rho(N)_l \left(\frac{3\gamma_{PFC}}{\pi m}\right)^{1/2} \exp\left(\frac{-16\pi\gamma_{PFC}^3}{3k_B T_l (P_{ve} - P_{in})^2}\right) \tag{2.38}$$

Relating the critical vapor embryo formation flux (J=1x10^{12} m^{-3} s^{-1}) to nanodroplet volume (V~10^{-21} m^3) and time (t=1 s) with $J=1/Vt$ provides a critical droplet flux of 10^{33} m^{-3} s^{-1}.[27,28]

The experimental vapor formation flux threshold for homogeneous vaporization provides a relation for the reduced temperature required to meet that flux. Comparing theory to experiment has shown homogeneous nucleation to occur at a reduced temperature (T_r) of 90% the critical temperature with a corresponding vapor formation flux of J = 10^{33} m^{-3} s^{-1}. The critical temperature of C_4F_{10} is 386.35 K.[14]

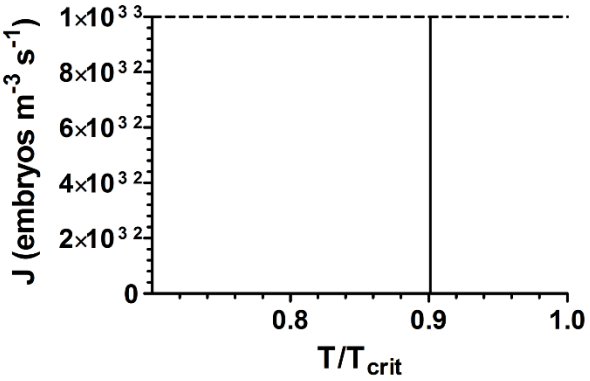

Figure 2.14. The vapor embryo formation rate versus superheated temperature plotted logarithmically for a 0.8 μm diameter droplet at atmospheric pressure.

2.5 Conclusions

Classical condensation and vaporization theories were reviewed to present the idea of two-phase equilibrium and its relation to traditional saturation. Predictions were made for lipid-stabilized microbubbles and nanodrops undergoing condensation and vaporization, respectively, while being

subjected to Laplace pressures. It was found that the Laplace pressure should decrease the condensation pressure and increase the vaporization temperature. Heterogeneous and homogeneous nucleation was introduced. Assuming homogeneous nucleation of a pure PFC microbubble provided condensation ranging from 12 to 130 kPa above macroscopic bulk condensation pressures at room temperature. The homogeneous nucleation of a gas embryo in a superheated liquid presented vaporization temperatures around 90 % of the critical temperature of the PFC. The homogeneous vaporization analysis also posed concern of how PFC surface tension varies with temperature. A predicted phase diagram is presented in Figure 2.16 to provide the possible thermodynamic conditions for microbubble condensation and droplet vaporization.

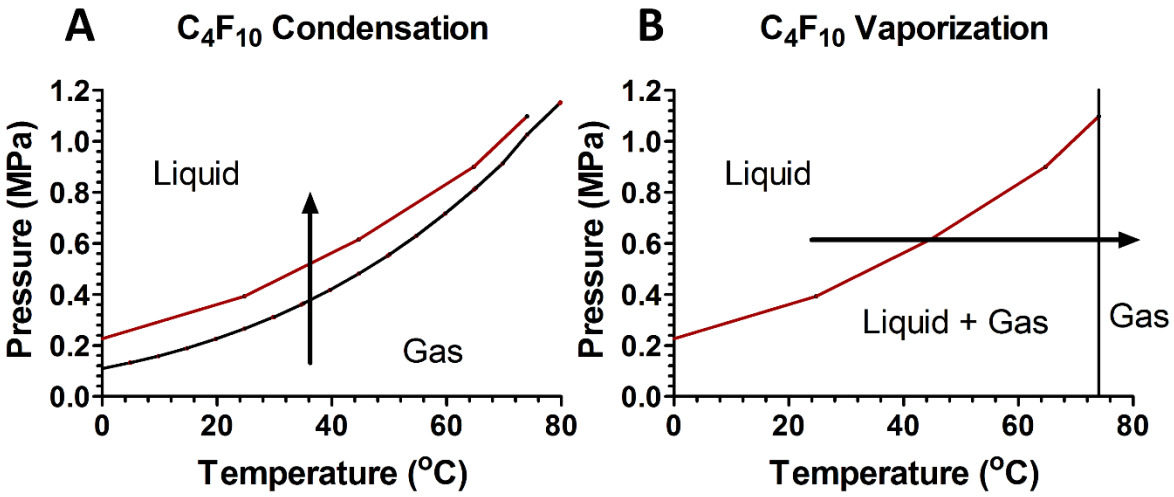

Figure 2.15. Phase diagrams for C_4F_{10} microbubbles condensing (**A**) and nanodrops vaporizing (**B**). Area between the red and black lines represent the potential multi-phase regimes originally presented in Figures 2.4 & 2.5.

References

[1] Sheeran, P. S., Wong, V. P., Luois, S., McFarland, R. J., Ross, W. D., Feingold, S., Matsunaga, T. O., and Dayton, P. A., 2011, "Decafluorobutane as a Phase-Change Contrast Agent for Low-Energy Extravascular Ultrasonic Imaging," Ultrasound Med. Biol., **37**(9), pp. 1518–1530.

[2] Carey, V. P., 2007, Liquid Vapor Phase Change Phenomena: An Introduction to the Thermophysics of Vaporization and Condensation Processes in Heat Transfer Equipment, Second Edition, CRC Press, New York.

[3] Davies, J. T., and Rideal, S. E. K., 1963, Interfacial phenomena, Academic Press.

[4] Lamberti, V. E., Fosdick, L. D., Jessup, E. R., and Schauble, C. J. C., 2002, "A Hands-On Introduction to Molecular Dynamics," J. Chem. Educ., **79**(5), p. 601.

[5] Israelachvili, J. N., 1992, Intermolecular and Surface Forces, Second Edition: With Applications to Colloidal and Biological Systems, Academic Press.

[6] Reif, F., 2008, Fundamentals of Statistical and Thermal Physics, Waveland Pr Inc.

[7] Nosé, S., 1984, "A molecular dynamics method for simulations in the canonical ensemble," Mol. Phys., **52**(2), pp. 255–268.

[8] Wiebe, R., and Gaddy, V. L., 1940, "The Solubility of Carbon Dioxide in Water at Various Temperatures from 12 to 40° and at Pressures to 500 Atmospheres. Critical Phenomena*," J. Am. Chem. Soc., **62**(4), pp. 815–817.

[9] Waldram, J. R., 1985, The Theory of Thermodynamics.

[10] Hobbs, S. K., Monsky, W. L., Yuan, F., Roberts, W. G., Griffith, L., Torchilin, V. P., and Jain, R. K., 1998, "Regulation of Transport Pathways in Tumor Vessels: Role of Tumor Type and Microenvironment," Proc. Natl. Acad. Sci., **95**(8), pp. 4607–4612.

[11] D'Arrigo, J. S., and Imae, T., 1992, "Physical characteristics of ultrastable lipid-coated microbubbles," J. Colloid Interface Sci., **149**(2), pp. 592–595.

[12] Ahmar, E. E., Valtz, A., Naidoo, P., Coquelet, C., and Ramjugernath, D., 2011, "Isothermal Vapor−Liquid Equilibrium Data for the Perfluorobutane (R610) + Ethane System at Temperatures from (263 to 353) K," J. Chem. Eng. Data, **56**(5), pp. 1918–1924.

[13] Thomson, G. W., 1946, "The Antoine Equation for Vapor-pressure Data.," Chem. Rev., **38**(1), pp. 1–39.

[14] Brown, J. A., and Mears, W. H., 1958, "Physical Properties of n-Perfluorobutane," J. Phys. Chem., **62**(8), pp. 960–962.

[15] Pace, E. L., and Plaush, A. C., 1967, "Thermodynamic Properties of Octafluoropropane from 14°K to Its Normal Boiling Point. An Estimate of the Barrier to Internal Rotation from the Entropy and Heat Capacity of the Gas," J. Chem. Phys., **47**(1), pp. 38–43.

[16] Sheeran, P. S., Luois, S. H., Mullin, L. B., Matsunaga, T. O., and Dayton, P. A., 2012, "Design of ultrasonically-activatable nanoparticles using low boiling point perfluorocarbons," Biomaterials, **33**(11), pp. 3262–3269.

[17] Dove, J. D., Mountford, P. A., Murray, T. W., and Borden, M. A., 2014, "Engineering optically triggered droplets for photoacoustic imaging and therapy," Biomed. Opt. Express, **5**(12), p. 4417.

[18] 2014, "Compendium of Chemical Terminology," Wikipedia Free Encycl.

[19] Illingworth, A. J., 1988, "The formation of rain in convective clouds," Nature, **336**(6201), pp. 754–756.

[20] Wilson, C. T. R., 1897, "Condensation of Water Vapour in the Presence of Dust-Free Air and other Gases.," Proc. R. Soc. Lond., **61**(369-377), pp. 240–242.

[21] Tsige, M., and Grest, G. S., 2008, "Surface Tension and Surface Orientation of Perfluorinated Alkanes," J. Phys. Chem. C, **112**(13), pp. 5029–5035.

[22] Lemmon, E. W., Huber, M. L., and McLinden, M. O., 2002, NIST reference fluid thermodynamic and transport properties–REFPROP, Version.

[23] Cahn, J. W., 1961, "On spinodal decomposition," Acta Metall., **9**(9), pp. 795–801.

[24] Hung, C.-H., Krasnopoler, M. J., and Katz, J. L., 1989, "Condensation of a supersaturated vapor. VIII. The homogeneous nucleation of n-nonane," J. Chem. Phys., **90**(3), pp. 1856–1865.

[25] Langmuir, I., and Schaefer, V. J., 1943, "Rates of evaporation of water through compressed monolayers on water," J. Frankl. Inst., **235**(2), pp. 119–162.

[26] Kincaid, J. F., and Eyring, H., 1938, "Free Volumes and Free Angle Ratios of Molecules in Liquids," J. Chem. Phys., **6**(10), pp. 620–629.

[27] Avedisian, C. T., and Glassman, I., 1981, "High Pressure Homogeneous Nucleation of Bubbles within Superheated Binary Liquid Mixtures," J. Heat Transf., **103**(2), pp. 272–280.

[28] Kwak, H.-Y., and Lee, S., 1991, "Homogeneous Bubble Nucleation Predicted by a Molecular Interaction Model," J. Heat Transf., **113**(3), pp. 714–721.

[29] Katz, J. L., and Blander, M., 1973, "Condensation and boiling: Corrections to homogeneous nucleation theory for nonideal gases," J. Colloid Interface Sci., **42**(3), pp. 496–502.

Chapter 3

Condensation of Lipid-Coated Perfluorobutane Microbubbles

3.1 Introduction

The work presented in this chapter concentrates on exploring the stability and behavior of microbubble condensed droplets during the condensation process. An attempt to understand the fundamental reasoning for condensation is presented followed work published in Langmuir titled *"Condensation Phase Diagrams for Lipid-Coated Perfluorobutane Microbubbles"*.[1] Condensation pressures of microbubbles were measured at multiple temperatures. Condensation energy barriers dependent of microbubble shell material were quantified. A comparison to homogeneous nucleation condensation theory is made.

3.2 Motivation

While prior research has investigated the use of different fluorocarbons to form the dispersed phase in MCDs, very little is known about the effects of the lipid shell. It is possible to imagine the addition of a lipid shell at the gas-liquid interface inhibiting condensation to higher pressures and

increasing the work required to minimize the potential energy of the molecules in the microbubble core into a liquid state. It is well established that lipid shell composition and nanostructure can profoundly impact microbubble stability.[2–4] A lipid shell may therefore significantly affect the compression and condensation process used to form MCDs. In this investigation, this question was directly addressed by changing lipid acyl chain length for 4-5 μm diameter size-selected microbubbles and observing the impact on compression and condensation behavior. Bright field microscopy was used with a custom chamber employing temperature and pressure control to track the size and onset of condensation for individual perfluorobutane microbubbles being subjected to a constant rate of pressurization. Fluorescence microscopy was used to image the lipid shell during this process. These experiments allowed observation of lipid monolayers under states of lateral compression, temperature and hydrostatic pressure that is inaccessible using traditional Langmuir trough and captive bubble techniques.[3,5] Additionally, light scattering was used to measure the resulting MCD size distribution. Our results show that the lipid shell can significantly impact the compression process by providing mechanical strength and permeation resistance to gas dissolution, and that the shell also impacts the minimum pressure needed to condense the gas into a liquid. The resulting experimental data were used to construct temperature-pressure phase diagrams for microbubble condensation, which we expect will aid in the materials selection of optimal MCDs for biomedical and industrial applications.

3.3 Materials and Methods

3.3.1 Microbubble Formulation

We generated suspensions of microbubbles coated with lipids of different acyl chain lengths to probe the effect of inter-lipid van der Waals dispersion forces on microbubble condensation. All

lipids were purchased in powder form and stored at -20 °C with a nitrogen head space. Microbubbles were formulated by probe sonication of a lipid suspension containing 90 mol% saturated diacyl phosphatidylcholine (PC) and 10 mol% 1,2-disteroyl-*sn*-glycero-3-phosphoethanolamine-N-[methoxy(polyethylene glycol)-2000] (DSPE-PEG-2000) (NOF America, White Plains, NY). Six different chain lengths were examined: 1,2-dimyristoyl-*sn*-glycero-3-phosphocholine (DMPC, C:14), 1,2-dipalmitoyl-*sn*-glycero-3-phosphocholine (DPPC, C:16), 1,2-distearoyl-*sn*-glycero-3-phosphocholine (DSPC, C:18), 1,2-diarachidoyl-*sn*-glycero-3-phosphocholine (DAPC, C:20), 1,2-dibehenoyl-*sn*-glycero-3-phosphocholine (DBPC, C:22), and 1,2-dilignoceroyl-*sn*-glycero-3-phosphocholine (DLIPC, C:24) (Avanti Polar Lipids, Alabaster, AL). The lipid compositions were suspended in 100 mL of 150 mM NaCl, 0.2-µm cold-filtered phosphate buffered saline (PBS) pH 7.4 (Sigma-Aldrich) at a lipid concentration of 2 mg mL^{-1} and then heated beyond the main phase transition temperature (T_m) of the PC lipid (DMPC (23°C), DPPC (41°C), DSPC (55°C), DAPC (66°C), DBPC (75°C), and DLIPC (80°C)).[6] Microbubbles were formed using a method similar to that originally described by Klibanov et al.[7] The mixture was sonicated with an ultrasonic probe (Branson 450 Sonifier, Danbury, CT) at low power (1/10) to disperse the lipids into a suspension of unilamellar vesicles. The power was then increased (10/10) for 10 s to generate microbubbles while perfluorobutane (C_4F_{10}) (FluoroMed, L.P., Round Rock, TX) was introduced at the gas-liquid interface. The solution was then quenched in an ice bath until the solution temperature was near room temperature. Microbubbles were then size-isolated to 4-5 µm diameter using differential centrifugation, as described by Feshitan et al.,[8] and washed three times using centrifugation (Eppendorf 5804 Centrifuge, Hauppauge, NY). Size distributions and concentrations of the probe-sonicated microbubbles were measured by laser light scattering and obscuration using the Accusizer 780A (Particle Sizing Systems, Santa Barbara, CA).

3.3.2 Fluorescent Microbubble Formulation

Microbubbles were formed with fluorescent lipid coats to visualize their deformation during pressurization. DSPC and DSPE-PEG2000 at a molar ratio of 9:1 were dissolved in chloroform (Fisher, Pittsburg, PA) at a concentration of 50 mg mL^{-1}. The microbubble shell was made fluorescent by adding the lipid membrane probe DiI (Invitrogen, Grand Island, NY) at a concentration of 1 μg mg^{-1} lipid. The chloroform was then evaporated under nitrogen for 10 min and further dried under a vacuum overnight. The lipid film was then rehydrated in a 10-mL scintillation vial with 8 mL of PBS to a final lipid concentration of 2 mg mL^{-1}. Rehydrated lipids were sonicated at 60 °C for 50 min in a water bath sonicator (Branson 3510) to aid lipid mixing and form unilamellar vesicles, the suspension was pipetted to 2-mL serum vials, the vials were sealed with a septum and crimp cap, and the gas headspace was exchanged with C_4F_{10}. Microbubbles were formed by agitation of the vial using a dental amalgamator (TPC D-650, City of Industry, CA). The microbubbles were pooled into a 12-mL syringe, washed three times using centrifugation and analyzed for size distribution and concentration using the Accusizer 780A.

3.3.3 Microbubble Pressurization

Microbubble samples were observed during pressurization using a custom temperature-controlled chamber attached to a microscope stage (Olympus BX52, Center Valley, PA) (Figure 3.1). Microbubbles were diluted to 10^6 mL^{-1}. 1 mL of the suspension was injected into the sample inlet port of the chamber while the valve on the exit port remained open to allow steady laminar flow through the chamber. After microbubbles rose under buoyancy to the top coverslip, the exit-port valve was closed. The inlet port was attached to a 12-mL syringe filled with C_4F_{10}-saturated PBS and locked into a programmable syringe pump (Harvard PHD 2000, Holliston,

MA) to control pressure. The chamber temperature was recorded with a thermistor (Omega HSTH-44033, Stamford, CT) and controlled with a water bath containing a copper heat exchanger connected to a flow-through bath circulator (Fisher Sci. Isotemp 3016P). The

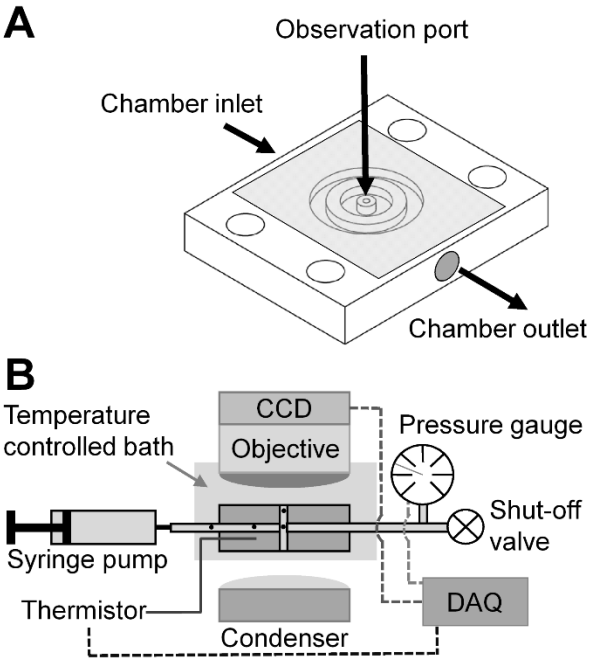

Figure 3.1. A) Pressure chamber capable withstanding 1.4 MPa of hydrostatic pressure while simultaneously viewing samples under 100x, high-numerical aperture bright-field and fluorescence microscopy. **B**) Experimental apparatus for the simultaneous control of hydrostatic pressure and temperature and observation of microbubble size and morphology.

pressure was recorded with a digital pressure gauge (Omega DPG1000). The chamber was pressurized by compressing the syringe plunger to achieve a constant pressurization rate of 34.5 kPa s^{-1} (5 psi s^{-1}), until condensation was observed. During pressurization, images of individual microbubbles were captured using a digital camera (Q-Imaging Q-Click, Surrey, BC Canada) at a 2.5 s^{-1} frame rate. Video, pressure and temperature outputs were observed and recorded through a custom LabView (National Instruments, Austin, TX) program.

3.3.4 Nanodrop Sizing

Microbubbles of 4-5 µm diameter and coated with lipids at each acyl chain length were pressurized and condensed at a concentration of 10^8 mL^{-1} and sample volume of 1.0 mL at a rate of 34.5 kPa s^{-1}(5 psi s^{-1}) at a temperature of 25 ^oC in a 3-mL syringe. The rate of pressurization was controlled with a computer-controlled syringe pump. Post pressurization, 1.0 mL of the condensed solution was pipetted into a 1.5-mL cuvette for sizing by dynamic light scattering (Malvern Nano-S90, Worcestershire, UK), in which the refractive index of the condensed droplet was assumed to be 1.276 for liquid C_4F_{10} and the surrounding media was that of water (1.3477).[9,10]

3.3.5 Image Analysis

Digital videos were processed to generate individual microbubble size-time curves. The videos were converted to binary image stacks and analyzed with in LabView as particles to determine the maximum feret diameter, cross-sectional area and perimeter. The grayscale pixel threshold value for tracking bubbles during compression for image analysis was determined to be the minimum threshold that converted bubbles to traceable particles, but did not convert and track

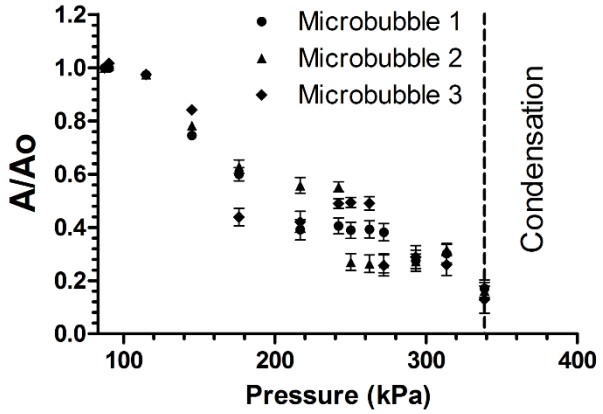

Figure 3.2. Relative cross-sectional area plot for three DSPC:DSPE-PEG2K (9:1) coated, size-isolated microbubbles analyzed and measured at four different pixel intensity thresholds (70, 80, 90, 100/255).

any background noise. Binary video conversion set microbubbles to be white (000/255) and the background to be black (255/255). Accuracy of the conversion to binary images was confirmed by manually comparing the particle size to that of the original microscopy video. For determining the uncertainty of the microbubble size measurement, the pixel intensity threshold was changed in steps of 10/255 from a value at which none of the background was identified (100/255) to a value for which none of the bubble was neglected (70/255). The maximum average uncertainty of microbubble radius was observed to be %7.6 at the smallest microbubble size immediately before condensation. The plot showing the error associated with the binary image analysis is presented in Figure 3.2. A custom cross-correlation particle tracking LabView program was developed to monitor microbubbles in the case of movement and to exclude any microbubbles that traveled into or out of the field of view during the pressurization experiment. The reported microbubble radius was determined by averaging the radii provided by the maximum feret diameter, area and perimeter measurements for each video frame.

3.3.6 Microbubble Compression Model

To determine the mode of microbubble compression prior to condensation, all samples were compared to the compression of an ideal gas bubble (no dissolution) and a free bubble (full dissolution). Microbubble volume during compression is described by the ideal gas law to be:

$$V(t)P_g(t) = n(t)BT \tag{3.1}$$

where V is the microbubble volume, P_g is the gas pressure inside the microbubble, n is the number of moles of C_4F_{10} present in the core, B is the ideal gas constant (8.314 Pa m^3 mol^{-1} K^{-1}), T is the solution temperature, and t is time in seconds. Prior to pressurization, microbubbles were assumed to be in a slightly compressed and buckled state indicating a non-existent surface tension at the gas-liquid interface.[11] For comparing a microbubble and an ideal gas undergoing isothermal

compression, the pressure inside the microbubble was assumed to equal the hydrostatic pressure (P_l), described as:

$$P_g(t) = P_l(t) = P_o + \dot{P}_r \cdot t \tag{3.2}$$

where P_o is the initial hydrostatic pressure (83.8 kPa in Boulder, CO) and P_r is the rate of pressurization. Differentiation of the ideal gas law relation provides the change in microbubble volume with respect to time as being:

$$\frac{dV(t)}{dt} P_g(t) + \frac{dP_g(t)}{dt} V(t) = \frac{dn(t)}{dt} BT \tag{3.3}$$

where

$$\frac{dV}{dt} = 4\pi R(t)^2 \frac{dR}{dT} \tag{3.4}$$

Combining (3) and (4) gives:

$$4\pi R(t)^2 \frac{dR}{dt} P_g(t) + \dot{P}_r \frac{4}{3} \pi R(t) = \frac{dn(t)}{dt} BT \tag{3.5}$$

where R is the microbubble radius. From the ideal gas law:

$$\frac{4}{3} \pi R(t)^3 = \frac{n(t)BT}{P_g(t)} \tag{3.6}$$

Combining (5) and (6):

$$4\pi R(t)^2 \frac{dR(t)}{dt} P_g(t) + \frac{\dot{P}_r \, n(t)BT}{P_g(t)} = \frac{dn(t)}{dt} BT \tag{3.7}$$

Solving for the differential of the microbubble radius with respect to time:

$$\frac{dR(t)}{dt} = \frac{BT}{P_g(t) 4\pi R(t)^2} \left(\frac{dn(t)}{dt} - \frac{\dot{P}_r \cdot n(t)}{P_g(t)} \right) \tag{3.8}$$

For an ideal gas microbubble undergoing isothermal compression (no dissolution), the *n* term is constant and the ordinary differential equation reduces to:

$$\frac{dR(t)}{dt} = -\frac{\dot{P_r} \cdot n(t) BT}{P_g(t)^2 4\pi R(t)^2} \tag{3.9}$$

Microbubbles that experience slight or full dissolution during compression are modeled as having a loss in moles of gas to the surroundings. Equation (8) expresses the change in radius with respect to time for these microbubbles. The change in microbubble gas content with respect to time is defined as:

$$\frac{dn(t)}{dt} = -\frac{4\pi R(t)^2 K_H}{\Omega_{shell} + \frac{R(t)}{D}} (P_g(t) - f \cdot P_o) \tag{3.10}$$

by Borden and Longo,[12] where K_H is the Henry's constant for C_4F_{10} at 25°C (6.9×10^{-5} [g m^{-3} Pa^{-1}]), Ω_{shell} is the shell resistance to gas permeation and D is the diffusivity of C_4F_{10} at 25°C (4.935×10^{-10} [m^2 s^{-1}]). For a free bubble with no resistance to gas permeation through the shell, Ω_{shell} goes to zero and the change in moles with respect to time turns to:

$$\frac{dn(t)}{dt} = -4\pi R(t) K_H D \cdot (P_g(t) - f \cdot P_o) \tag{3.11}$$

Comparing these two models (bubbles able to dissolve verse non-dissolvable) to experimental results provides the potential to extract the shell permeation properties. However, the shell may also have mechanical viscoelastic properties that resist compression, which are unknown at this time, making this analysis more complex.

3.3.7 Controlling Dissolved C_4F_{10} Gas Content

PBS solutions were made with different dissolved C_4F_{10} gas contents to determine the effect on microbubble condensation. We investigated under-saturated, saturated and super-saturated C_4F_{10}

in PBS solutions, where the saturation level was controlled by equilibrating the solution at one temperature and then rapidly bringing the solution back to room temperature (25 °C). In each case, 1.0 L of 150 mM NaCl, 0.2-μm cold-filtered was degassed under house vacuum and stirred for 24 h, and then C_4F_{10} was used to fill the headspace. Under-saturated C_4F_{10} solutions were equilibrated at 45 °C, saturated solutions were equilibrated at 25 °C, and super-saturated C_4F_{10} solutions were equilibrated at 4 °C. All C_4F_{10} solutions were equilibrated for 24 h before bringing them back to room temperature just prior to the microbubble condensation experiments. This experiment was designed to change the driving force for dissolution: the fractional gas concentration ($f = C_0/C_s$) defined by Epstein and Plesset[13,14] where C_0 is the dissolved gas concentration and C_s is the concentration at saturation.

3.3.8 Construction of Microbubble Temperature-Pressure Phase Diagrams

Condensation of microbubbles into nanodrops was determined from video analysis to be the point at which the MCD refractive index (1.0015 for C_4F_{10} gas[9]) converted to a value closer to that of water, and the droplets disappeared. To construct condensation phase diagrams for C_4F_{10} microbubbles, temperature was held constant at 5 °C increments from 5 to 75 °C, and pressure was increased at 34.5 kPa s^{-1}. Temperature-pressure phase diagrams were constructed for PC lipids with acyl chain lengths of C:14, C:16, C:18, C:20, C:22 and C:24. The condensation pressure for each chain length was measured at each temperature for at least 3 microbubbles/batch obtained from no less than 3 batches.

The experimental condensation diagrams were compared to the theoretical diagram obtained for macroscopic C_4F_{10}.[15] Discrepancies between the experimental condensation pressure (defined here as the pressure outside the microbubble, P_{out}) and theoretical value (defined here as the pressure of the microbubble core, P_{in}) were assumed to be due to “surface tension” in

the shell, which could inhibit or promote condensation. If the shell inhibits condensation, then the surface tension value is negative. Such a situation may arise where appreciable work is required to mechanically deform the fully compressed shell to accommodate the shrinking core. In contrast, an uncompressed shell that promotes condensation provides a positive surface tension. This latter situation aligns with the conventional view of a gas/liquid interface. If we assume that the gas condenses at the theoretical condensation pressure, then the pressure difference between the chamber and the gas core can be described by the Laplace pressure to be:

$$\Delta P = P_{out} - P_{in} = \frac{2\sigma}{R} \tag{3.12}$$

where σ is the surface tension at the radius R immediately before the gas core undergoes the phase transformation to a liquid. According to convention[16], the surface pressure, π, is defined relative to the surface tension of a free gas/liquid interface, σ_o, as:

$$\pi = \sigma_o - \sigma \tag{3.13}$$

In our experiment, the microbubble surface pressure just prior to condensation is estimated by:

$$\pi = \sigma_o - \frac{R\Delta P}{2} \tag{3.14}$$

Note that for a shell that resists compression, the interior pressure is less than the hydrostatic pressure ($\Delta P > 0$), and the surface pressure exceeds the surface tension of a clean gas/liquid interface ($\pi > \sigma_o$). In this case, we can define a new surface over-pressure term (Π):

$$\Pi = \pi - \sigma_o = -\sigma \tag{3.15}$$

The surface over-pressure does not force an expansion of the bubble, but rather it mechanically resists compression of the microbubble to a nanodrop. Thus, Π, π and σ are force terms (specifically, force/distance) that depend on the mechanical properties of the lipid shell and the

mechanism (or path) of the deformation. Π and π are not equilibrium energy terms, even though they contain a surface free energy term, σ_o.

3.4 Results and Discussion

3.4.1 Condensation of Microbubbles into Nanodrops

Condensation of microbubbles to nanodrops was observed as an abrupt change in the appearance of the suspension from milky white to transparent. To better characterize this process, we imaged individual microbubbles during the condensation process. To our knowledge, this study is the first to verify the formation of individual MCDs through real-time microscopic

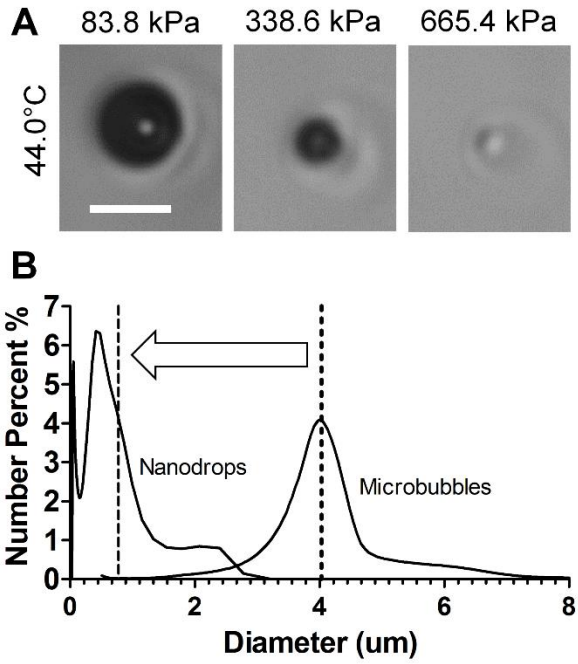

Figure 3.3. A Compression and condensation of a DPPC:DSPE-PEG2k (9:1) coated microbubble undergoing pressurization (ṗ=34.5 kPa s^{-1}) at 45℃. Larger microbubbles (~12 µm) yield visible condensed nanodrops under 50x brightfield microscopy. Scale bar represents 10 µm. **B** Accusizer size distribution for DPPC:DSPE-PEG2K (9:1) coated, size-isolated 4-5 µm microbubbles along with the DLS size distributions for microbubble-condensed nanodrops. Arrow shows the condensation shift from the average microbubble size (dotted black line) to the theoretical nanodrop size (dashed black line).

observation. Figure 3.3A shows a large (approx. 12μm in diameter) DPPC:DSPE-PEG2k (9:1) coated microbubble undergoing pressurization ($\dot{p}$=34.5 kPa s^{-1}) at 44 °C under bright field illumination. Initially, the gas core of the microbubble provided a strong contrast with the surrounding PBS. The dark appearance of the microbubble continued up to a pressure just below 665.4 kPa. At 665.4 kPa, the particle suddenly changed appearance to become more translucent, but it was still identifiable due to the relatively large diameter (~2 μm) of the droplet. This is consistent with a gas-to-liquid phase transition, where the index of refraction is expected to change from n_{gas} = 1.002 to n_{liq} = 1.276,[9] which is close to the value for water (n_{water} = 1.348).[10] The droplet was still visible because the index of refraction of the liquid C_4F_{10} droplet was not equal to that of water. Nanodrops generated by 4-5 μm diameter microbubbles, which are relevant to biological applications,[17] had a much smaller diameter (100-750 nm). These MCDs were not visible under microscopy because their cross-section is below the diffraction limit of the microscope.[18]

To verify microscopy observations, we measured the size distributions of microbubble and nanodrop suspensions. Figure 3.3B shows the initial microbubble size distribution of DPPC:DSPE-PEG2k (9:1) microbubbles prior to pressurization. The pre-condensation DPPC microbubble size distribution provided a mean diameter of 4.03 ± 0.81 μm. Also shown is the size distribution of the resulting nanodrops following pressurization of the same microbubbles, where the mean droplet diameter was measured to be 426 ± 384 nm. In theory, the diameter of a condensed nanodrop should be about 5.2 times smaller than that of its microbubble origin at STP due to the shift in C_4F_{10} density from a gas to a liquid.[19] Here, we found that the condensed nanodrop diameters were smaller than predicted (778 nm), which we attributed to C_4F_{10} dissolution

during the slow compression. The microbubble and nanodrop size distributions for C14 and C18-24 are provided in Figure 3.4.

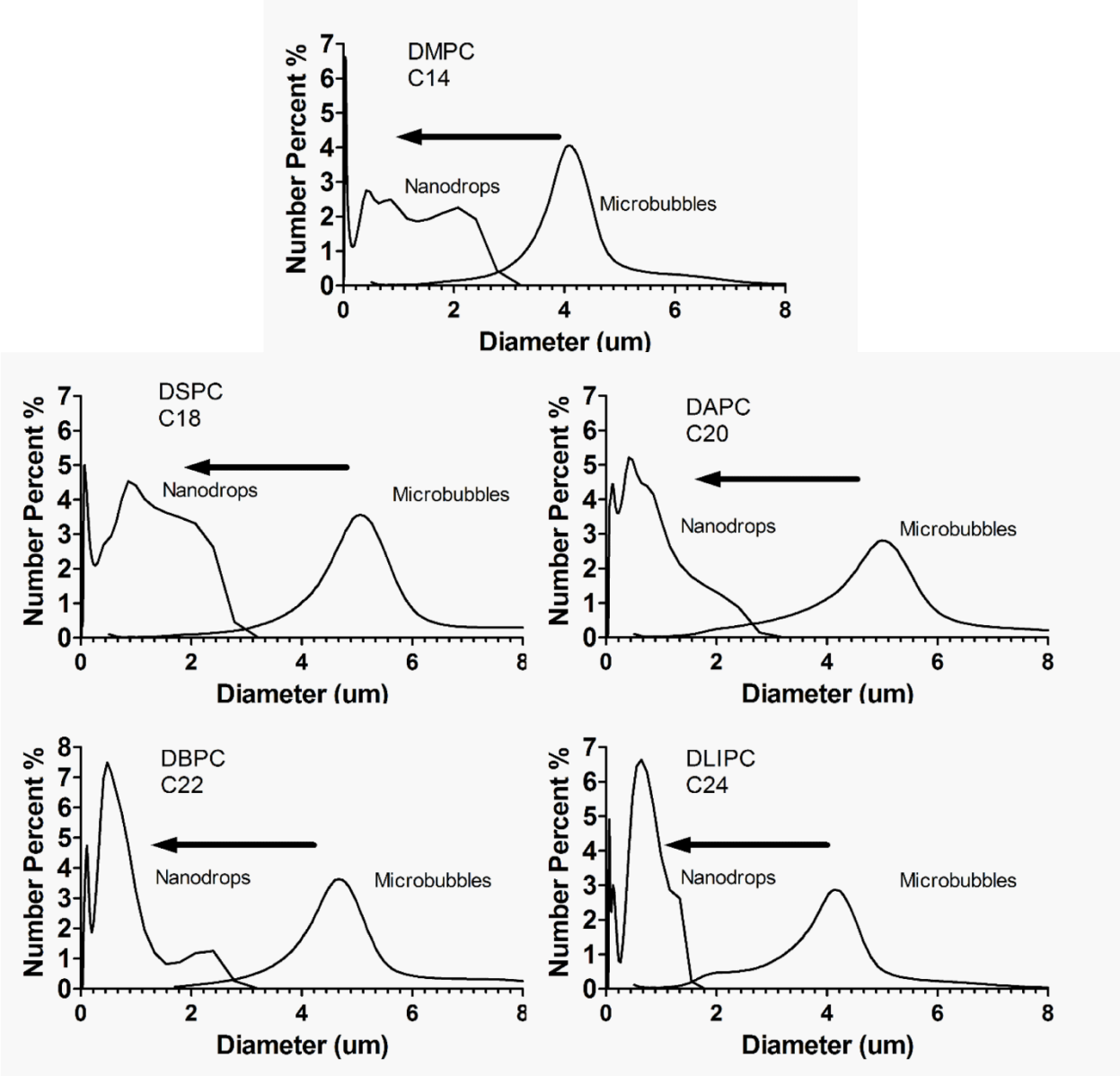

Figure 3.4. Accusizer size distribution for C14 and C18-24 shelled, size-isolated microbubbles along with the DLS size distributions for microbubble-condensed nanodrops.

3.4.2 Lipid Shell Behavior during Pressurization

Fluorescence microscopy was used to observe the lipid shell during the pressurization process. Figure 3.5 shows bright field and fluorescence images of a larger (~10 μm diameter) DiI:DSPC:DSPE-PEG2000 coated microbubble undergoing compression and condensation into a microdrop (~2 μm diameter). Figures 3.5A,B show the microbubble having a smooth surface at STP. Figures 3.5C-E show the surface wrinkling and collapsing during pressurization, denoted by white arrows. This wrinkling behavior indicates the shell is in a buckled state and that the effective surface tension is very low or possibly negative in magnitude. A negative surface tension would

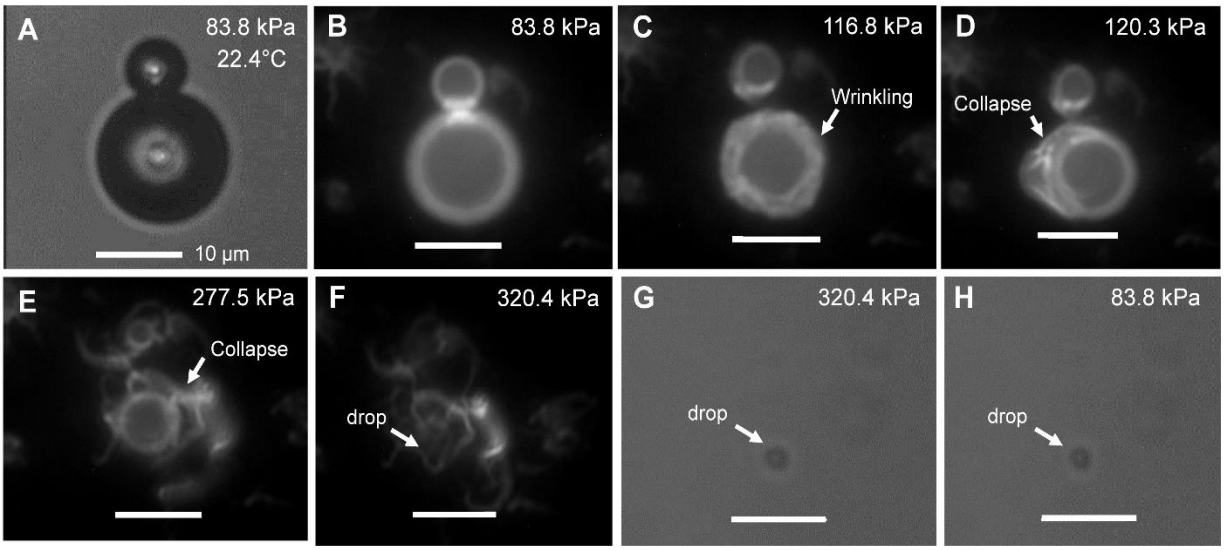

Figure 3.5. Microscopy images of DiI, DSPC:DSPE-PEG2K (9:1) coated microbubbles undergoing condensation ($\dot{p}$=34.5 kPa s^{-1}). The microbubbles were initially resting at 25 ˚C and 83.8 kPa. **A** In bright field microscopy, there was a strong contrast between the gas-filled microbubbles and the surrounding aqueous phase. **B** In fluorescence images, the microbubble shells often appeared uniformly fluorescent. In some cases, dark domains were observed on the microbubble surface (not shown). **C**,**D**,**E**,**F** The microbubbles were observed with fluorescence microscopy as they were pressurized. Arrows denote wrinkling and collapse morphologies of the lipid shell of the larger bubble on bottom. **G**,**H** Bright field microscopy showed loss of strong optical contrast at 320.4 kPa, which is consistent with a gas-to-liquid phase transition in the perfluorobutane core. The droplet was metastable and did not vaporize upon bringing the pressure back down to 83.8 kPa. The lipid shell of the droplet is denoted with an arrow in **F** with a surrounding "cloud" of sinuous lipid collapse structures. Collapse structures are also seen in **F** for the smaller bubble on top, but the condensation droplet could not be viewed at this magnification (100x). Scale bars represent 10 μm.

indicate that the shell is resisting compression due to the required work to deform and collapse the shell. Figures 3.5F,G show the proximity of the lipid to the nanodrop after condensation. The collapsed lipid appears to be connected to the nanodrop surface as long, sinuous strands, which likely comprise one or more bilayer lamella. Some collapsed lipid stands also appear to have detached from the droplet shell. Figure 3.5H presents the MCD at STP in droplet form verifying the ability of the droplet to remain stable in the super-heated state. The metastability of the MCD could be due to an energy barrier required to expand the surface area, for example due to the van der Waals cohesion energy of the lipid monolayer shell. At the 100-1000 nm diameter length scale, the surface-area-to-volume ratio is very high, which might explain the inhibited transformation of the MCD back into a microbubble at STP.

3.4.3 PFC Gas Core Behavior during Pressurization

Microscopy was also used to observe the morphology and projected area-time curves for microbubbles of different coatings and at different temperatures during pressurization. The behavior was classified into two categories: 1) complete dissolution or 2) partial dissolution and condensation. To differentiate between the two categories, the microbubble projected area-time curves were measured during pressurization. Microbubbles that disappeared from observation before the theoretical bulk condensation pressure were assumed to have completely dissolved. Microbubbles resisting condensation up until or past the theoretical bulk condensation pressure, and then suddenly disappearing, were assumed to have condensed. Figure 3.6 shows typical examples of these phenomena. Figure 3.6A shows a DSPC:DSPE-PEG2000 coated microbubble at 45 ^{o}C fully dissolving, while Figure 3.6B shows a DBPC:DSPE-PEG2000 coated microbubble at the same temperature compressing, dissolving and finally condensing. This can be seen more clearly in Figure 3.6C, which shows the relative projected areas (A/A_0) versus pressure for the two

microbubbles. The dashed line shows the theoretical bulk condensation pressure for C_4F_{10} at 45 °C.

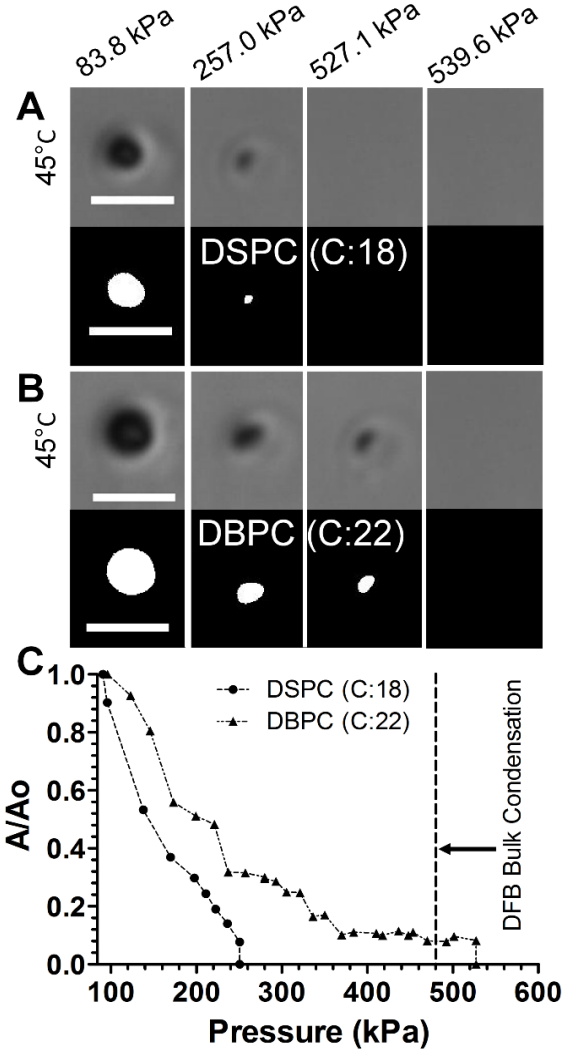

Figure 3.6. The conversion of bright field microscopy images to binary images for microbubble size measurement. **A** Full dissolution of a DSPC:DSPE-PEG2K (9:1) microbubble at 45°C under increased hydrostatic pressure ($\dot{p}$=34.5 kPa s^{-1}), and **B** condensation of a DBPC:DSPE-PEG2K (9:1) microbubble into a nanodrop under the same conditions. Scale bars represent 10 µm. **C** Relative area versus pressure plot for the DSPC:DSPE-PEG2K (9:1) and DBPC:DSPE-PEG2K (9:1) microbubbles seen in A and B. Dissolution was observed as a continuous decrease in size until the bubble became smaller than optical resolution at a pressure that is below the bulk C_4F_{10} condensation pressure (vertical dashed line) at this temperature. Another hallmark of dissolution was that each bubble disappeared at a different time, with smaller bubbles disappearing sooner than larger bubbles. Condensation, on the other hand, was observed as an abrupt change in bubble radius, often at a pressure above the bulk C_4F_{10} condensation pressure. Another indicator of condensation was that all bubbles in the video frame disappeared simultaneously, independent of initial size.

The DSPC (C16) microbubble showed a rapid and continuous reduction in projected area to a value of zero before the theoretical bulk condensation pressure. In contrast, the DBPC (C24) microbubble showed a slower rate of area reduction and stabilized at a low projected area (corresponding to a diameter of ~1 μm), eventually disappearing at a pressure beyond the bulk C_4F_{10} condensation pressure. Stabilization at small diameters has been previously observed for microbubbles undergoing acoustic pulsing[20] and gas exchange[21–23] at STP. The results here indicate that the "stable diameter" can persist even under significant pressurization. These two different behaviors (full-dissolution *vs.* condensation) were easily delineated by this method. The threshold temperature for full dissolution was recorded and used to construct the temperature-pressure phase diagrams below.

3.4.4 Effect of Dissolved Gas Content on Microbubble Stability

To further characterize the dissolution behavior and the conditions that promote condensation, we investigated the effect of C_4F_{10} concentration in the PBS surrounding the microbubble during pressurization. Figure 3.7A shows the relative projected area versus pressure curve for DPPC:DSPE-PEG2000 coated microbubbles undergoing compression ($\dot{p}$=34.5 kPa s^{-1}) while suspended in super-saturated, saturated or under-saturated C_4F_{10} in PBS. The rate of microbubble shrinkage during pressurization decreased with increasing dissolved C_4F_{10} content in the bulk. This result points to the significant role of dissolution in the compression process, and that super-saturated media can be used to minimize this effect during microbubble compression. For the remainder of the study, however, we chose to use saturated C_4F_{10} in PBS as the suspension media to minimize the possibility of microbubble growth prior to pressurization, which would complicate the analysis of temperature and shell composition effects.

Figure 3.7B shows the effect of dissolved C_4F_{10} content on the temperature-pressure phase diagram for DPPC:DSPE-PEG2000 microbubbles. As expected, increasing the dissolved gas content shifted the transition from condensation to full dissolution to higher temperatures. This

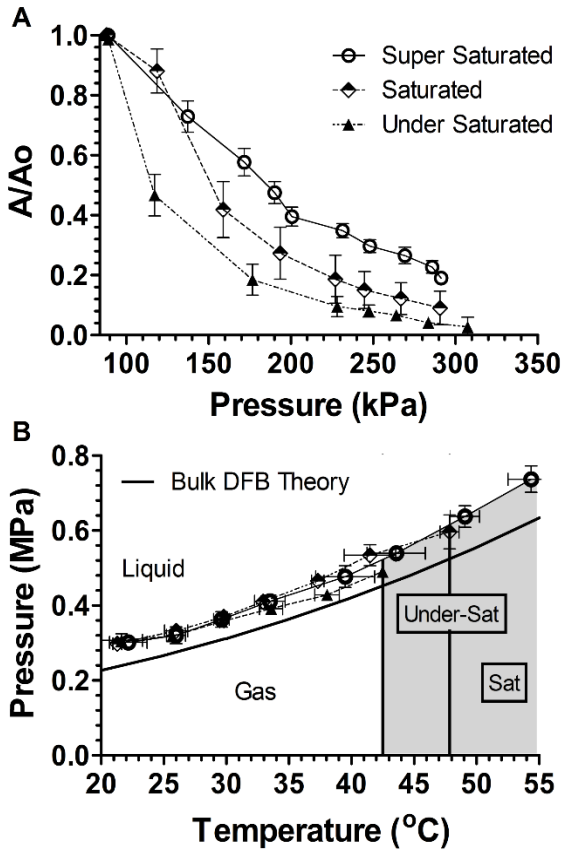

Figure 3.7. Effect of dissolved C_4F_{10} gas content on microbubble dissolution and condensation. **A** Relative area versus absolute pressure plot DPPC:DSPE-PEG2K (9:1) coated 4-5 µm size-isolated microbubbles compressing at 34.5 kPa s^{-1} while suspended in super-saturated (4℃, open circles), saturated (25℃, diamonds) and under-saturated (45℃, triangles) C_4F_{10} in PBS. **B** Microbubble phase diagram showing the vapor-to-liquid phase transition for bulk macroscopic C_4F_{10} (dashed line) and for 4-5 µm size-isolated microbubbles (solid lines fit to data points). The lines at 42 and 48 °C and the shaded region represent the temperatures at which the bubble response to pressurization transitioned from condensation to dissolution for under-saturated (shaded white) and saturated (shaded grey) solutions, respectively. Super-saturated solutions exhibited condensation for the entire temperature range tested here.

transition temperature increased from 42 to 47 ºC for under-saturated to saturated media, and the transition to full dissolution for super-saturated media was shifted to a temperature beyond 55 ºC.

However, the condensation pressure at each temperature below the dissolution transition was not much affected by dissolved C_4F_{10} content.

3.4.5 Microbubble Dissolution Prior to Condensation

More information on the dissolution behavior of the microbubbles was discerned from the size *vs.* time plots during isothermal compression ($\dot{p}$=34.5 kPa s^{-1}). Figure 3.8A shows the isothermal compression of microbubbles coated with several lipids (C14, C18 and C22) at a reduced temperature ($T_r = T/T_m$) equal to 0.4. First, note that the data for the different lipids do not collapse

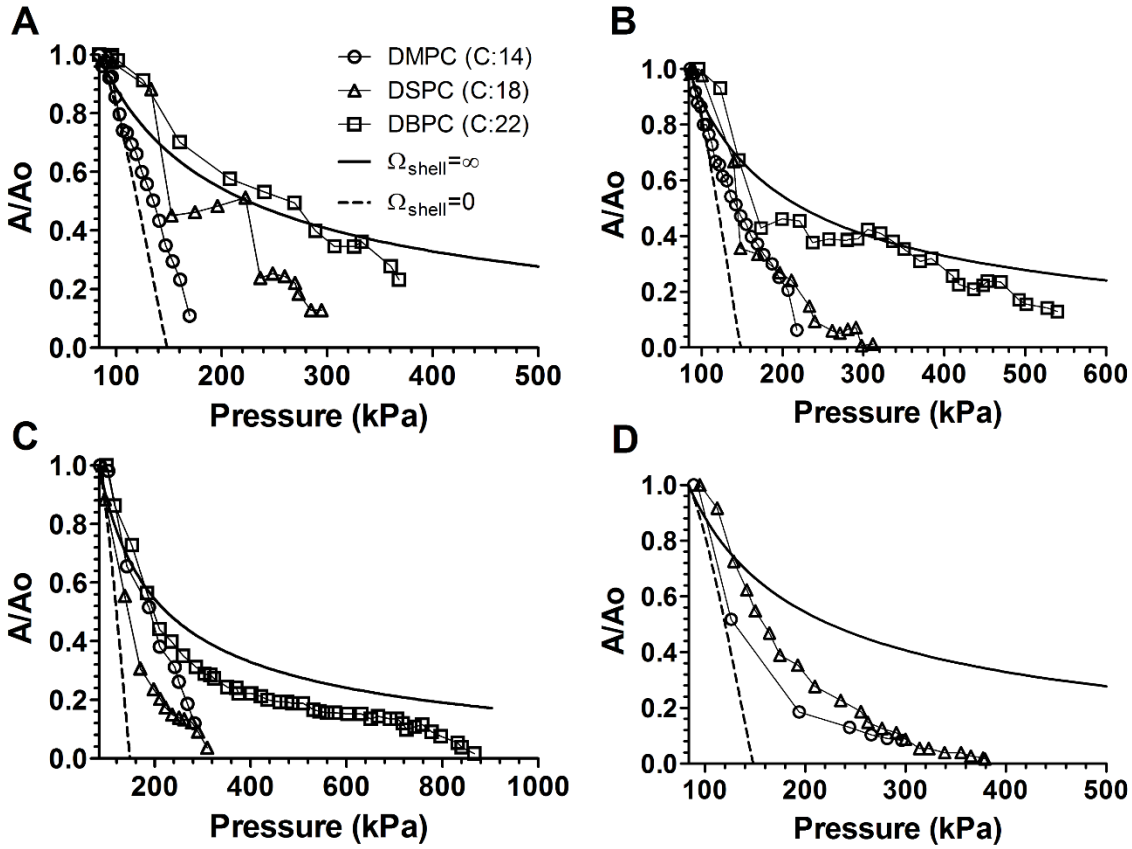

Figure 3.8. Effect of the lipid shell on microbubble compression and condensation. Shown are the relative area versus pressure ($\dot{p}$=34.5 kPa s^{-1}) plots for DMPC (circles), DSPC (triangles) and DBPC (Squares) : DSPE-PEG2K (9:1) coated 4-5 μm size-isolated microbubbles at reduced temperatures of **A** 0.4, **B** 0.6, **C** 0.8 and **D** 1.0. Also shown are the predicted projected area curves assuming compression and dissolution with zero shell resistance to gas transfer (dashed line) and ideal gas compression with no gas loss (solid line).

to a single curve, and the size decreases more rapidly for the shorter chain lipids. This indicates

that the gas permeation and mechanical properties of the lipid shells were different, even at the same reduced temperature. This was a curious result that was also found to be true at T_r = 0.6, 0.8 and 1.0 (Figures. 3.8B-D). To better visualize the effect of reduced temperature on microbubble

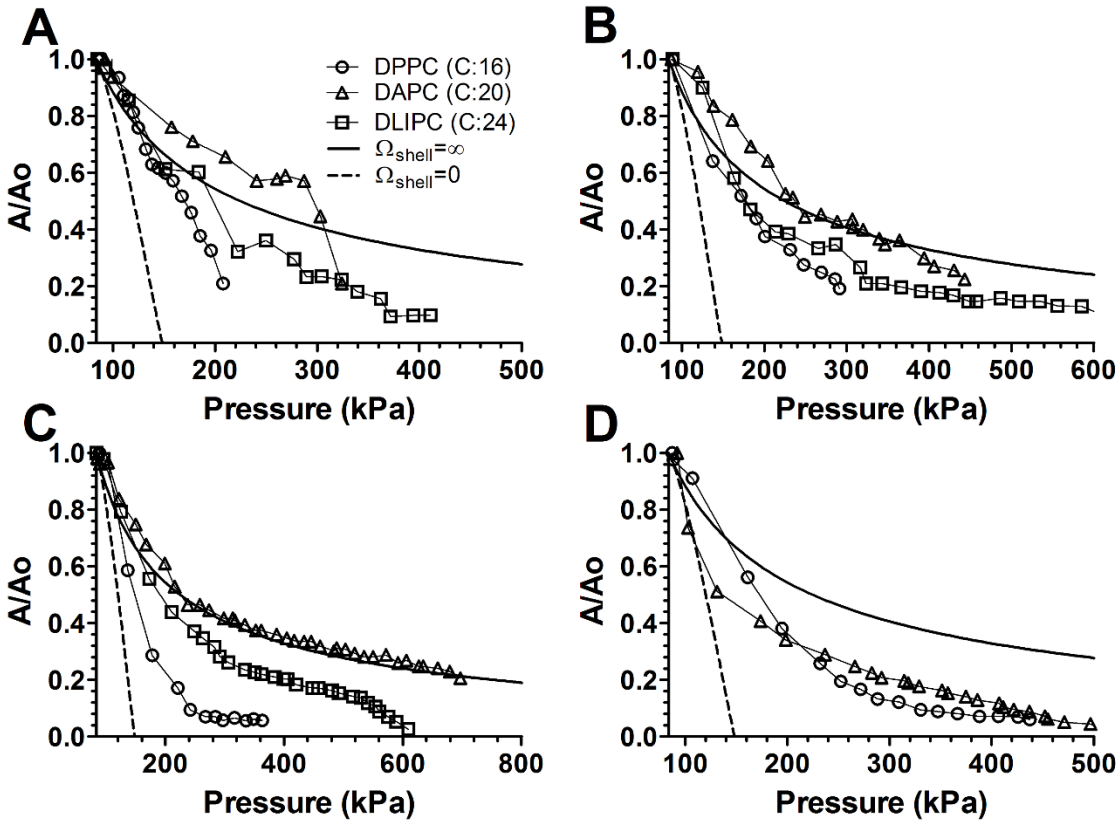

Figure 3.9. Effect of the lipid shell on microbubble compression and condensation. Shown are the relative area versus pressure ($\dot{p}$=34.5 kPa s^{-1}) plots for DPPC (circles), DAPC (triangles) and DLIPC (Squares) : DSPE-PEG2K (9:1) coated 4-5μm size-isolated microbubbles at reduced temperatures of **A** 0.4, **B** 0.6, **C** 0.8 and **D** 1.0. Also shown are the predicted projected area curves assuming compression and dissolution with zero shell resistance to gas transfer (dashed line) and ideal gas compression with no gas loss (solid line).

compression, the isothermal compression of (C16, C20 and C24) coated microbubbles is plotted in Figure 3.9. We expected that the chain length dependence would be eliminated by comparing the curves at the same T_r, a procedure which is meant to remove differences in the ratio of the thermal energy to the intermolecular van der Waals cohesion energy. Our result suggests that gas

permeation and mechanical properties of the lipid coats are not solely dependent on the van der Waals cohesion energy. It is well known that these properties also tend to depend on details of the

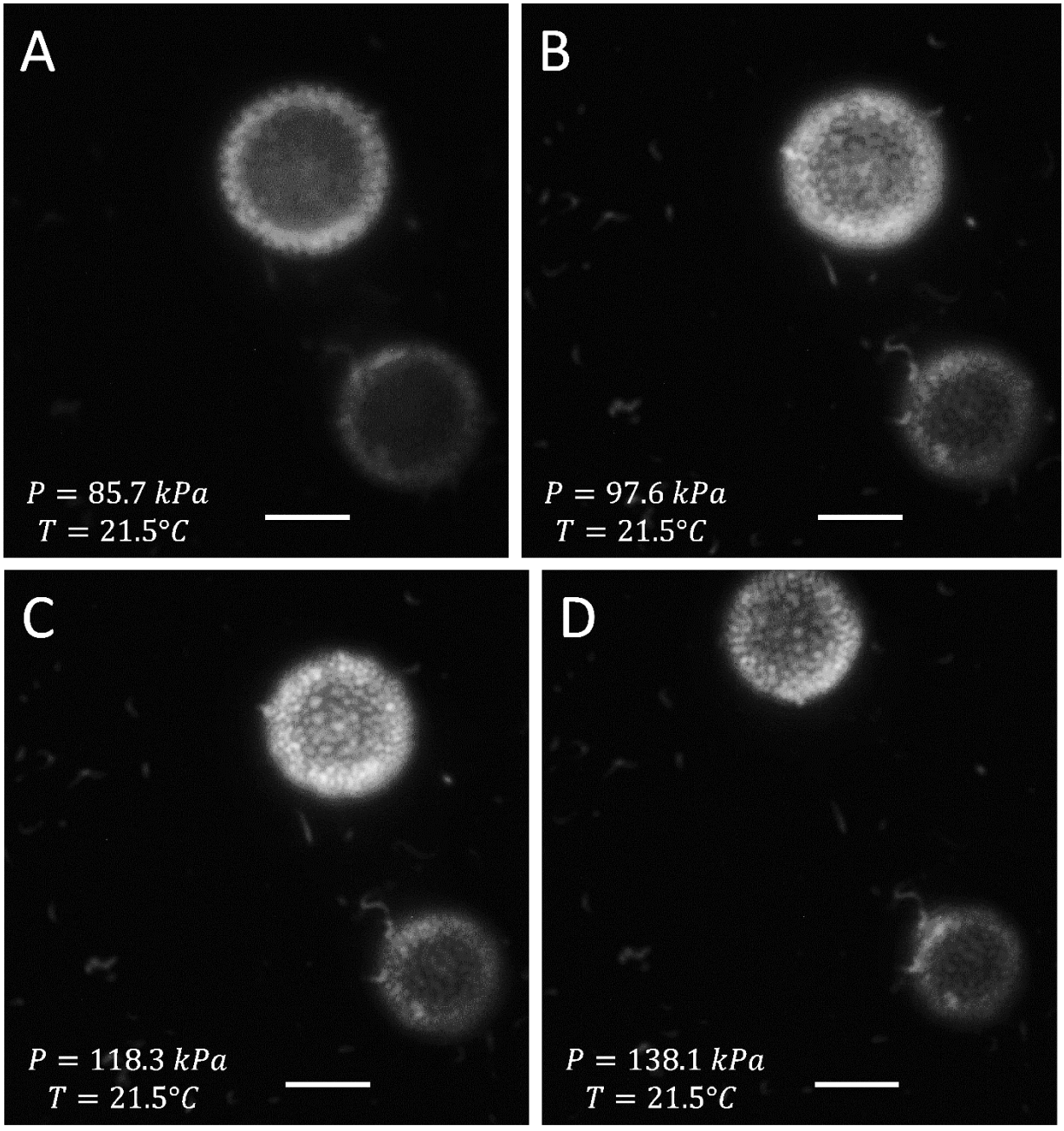

Figure 3.10. DiI fluorescent images of lipid domains forming on the surface of microbubbles due to phase separation of the monolayer.

nanostructure,[3,12] which may be different for these lipids. Certainly, membrane thickness

increases with acyl chain length. There are also likely to be heterogeneities in the monolayer plane, such as lateral phase separation,[24] that may impact the gas permeation and mechanical properties of the microbubble shells. The phase-separated monolayer can be seen in Figure 3.10, where C18 coated fluorescent microbubbles are undergoing pressurization and being forced to create new domains as the interfacial surface area decreases. Clues for this can also be found in data obtained for the acyl chain length dependence of microbubble *in vivo* circulation persistence,[4] where it was found that microbubbles coated with C24 are less stable than those coated with shorter chain lipids, a result that was attributed to hydrophobic mismatch between DLIPC and DSPE-PEG2000. We also documented differences in the crumpling behavior of individual microbubbles coated with DPPC compared to those coated with lung surfactant, which contains mainly DPPC as well as proteins and other lipids that provide lateral nanostructure.[25]

Also plotted in Figure 3.8 & 3.9 are the theoretical projected area-pressure curves for a microbubble with no shell ($\Omega_{shell} = 0$) and with a gas-impermeable shell ($\Omega_{shell} = \infty$) based on the dissolution model (Equations 3.11 and 3.9, respectively). In most cases, the data fall between these two extremes, indicating partial dissolution of the gas core (Figure 3.11A) It has been shown mathematically that the shell elasticity reduces interfacial surface tension as microbubble size decreases to stabilize the gas-liquid interface.[26] As already mentioned above, the lipid shells shifted the condensation pressures above the theoretical values for bulk C_4F_{10}. The reduction in interfacial surface tension with microbubble size could be responsible for heightened microbubble condensation pressures. A careful inspection of Figure 3.8A shows that a portion of the projected area curve for DBPC lies above that predicted for compression of a non-dissolving bubble, indicating a mechanical resistance to compression. Additionally, the curve for DSPC at $T_r = 0.4$ shows flattening and snapping of the bubble, which is striking evidence for a solid-like response

involving a mechanical instability. Thus, while the mechanical properties appear to play a significant role, the mechanism and constitutive equations to describe the deformation are unknown, making it difficult to isolate the gas permeation term.

Finally, we note that the projected area-pressure curves became smoother and more consistent between lipids as the reduced temperature was increased. The increase in T_r (ratio of the thermal energy to van der Waals cohesion energy) causes an increase in fluidity of the lipid shell. As the shells became soft, they exhibited less mechanical strength and more dissolution. The drop in lipid-to-lipid variability at high T_r indicated that effects of microstructural defects were reduced, and the van der Waals cohesion energy between the lipids became a better determinant of the overall microbubble behavior.

3.4.6 Shell Resistance to Diffusion and Rate of Pressurization

Dissolution of a microbubble versus shell resistance to gas permeation and pressurization rate is modeled in Figure 3.11. Figure 3.11A presents 4 μm diameter bubble subjected to a pressure ramp of 34.5 kPa s^{-1} with a shell resistance ranging from 0 (Eqn. 3.11) to 750 s cm^{-1}. When the microbubble lacks resistance to diffusion (0 s cm^{-1}) it dissolves after ~ 5 s. If the microbubble has a high resistance to permeation (> 250 s cm^{-1}) then it behaves like an ideal gas ($\Omega_{shell} = \infty$) and losses none of the core material prior to condensation. Figure 3.11B presents the critical shell resistance versus the rate of pressurization of the solution. The critical shell resistance permits a 5 % loss in core material or less prior to reaching the bulk saturation pressure (265 kPa at 25 °C) during microbubble compression. Clearly, as the pressurization rate is increased, shell resistance to gas permeation becomes less influential to dissolution due to expedited condensation times. For the pressurization rate used in this study (34.5 kPa s^{-1}) an effective shell resistance to gas permeation of ~1000 s cm^{-1} is required to only lose 5 % of C_4F_{10} during compression. This

prediction indicates that there is most likely a moderate loss of core PFC material during condensation.

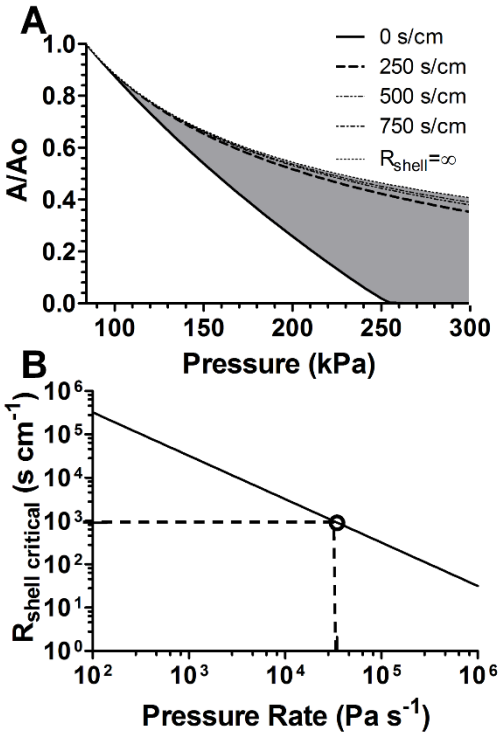

Figure 3.11. Theoretical effect of dissolution on microbubble compression and condensation. **A**) Relative area versus pressure plot for a 4-µm diameter bubble undergoing constant pressurization ($\dot{p}$=34.5 kPa s^{-1}) and subject to shell resistances of 0, 250, 500, 750 and ∞ s cm^{-1}. The shaded region shows the divergence in relative volume behavior between a dissolving bubble and one without gas loss. **B**) A plot of the critical shell resistance, defined as the resistance at which the loss of microbubble core gas content is less than 5%, versus the rate of pressurization. This study's critical shell resistance (horizontal dashed line) required for only 5% gas loss during compression at $\dot{p}$=34.5 kPa s^{-1} (vertical dashed line) marked by the circle.

3.4.7 Microbubble Condensation Phase Diagrams

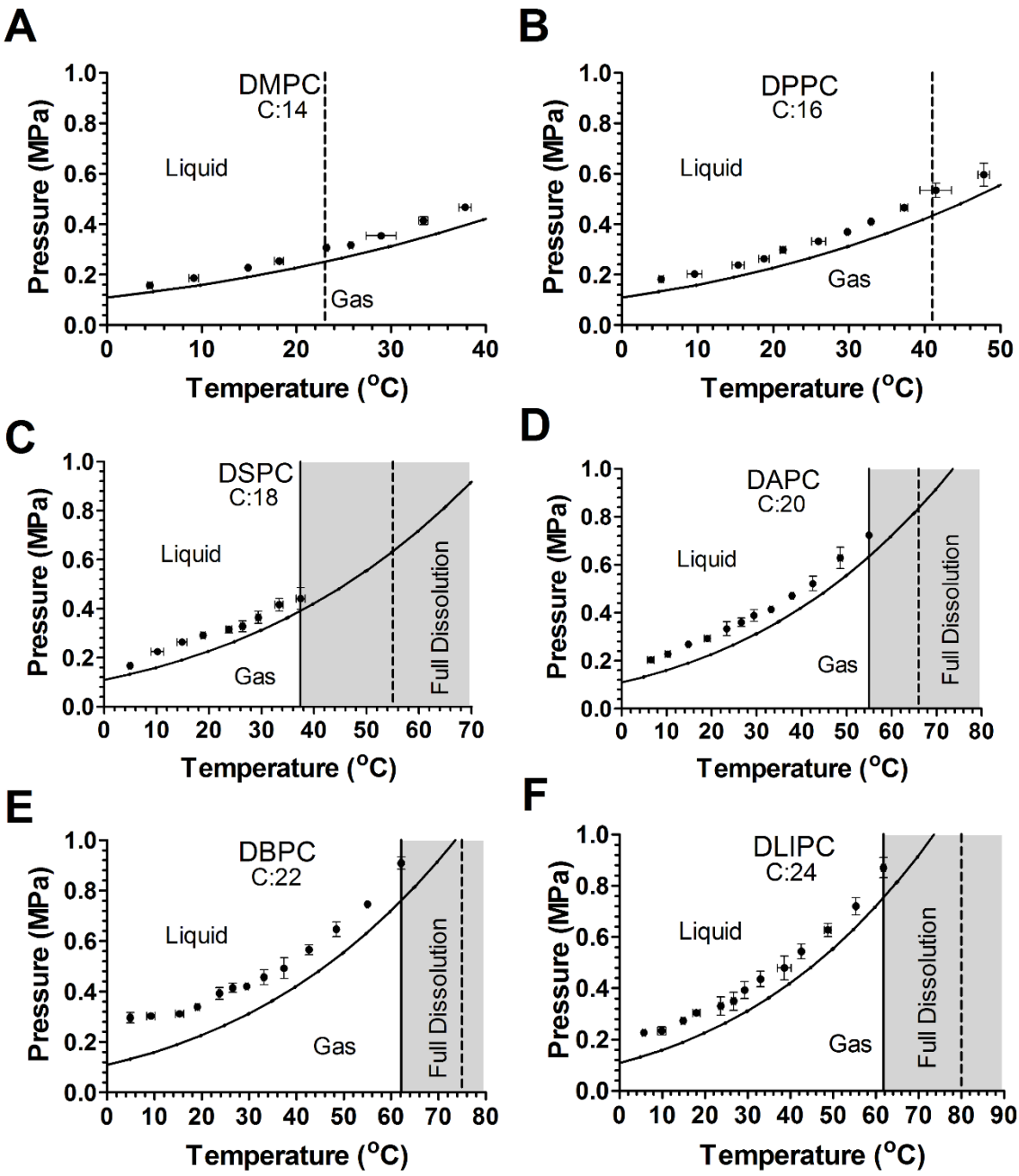

Figure 3.12. Microbubble condensation phase diagrams. Shown are the experimental points for [DMPC (**A**), DPPC (**B**), DSPC (**C**), DAPC (**D**), DBPC (**E**), and DLIPC (**F**)] : DSPE-PEG2K (9:1) coated, C4F10-core microbubbles with mean diameters of 4-5 μm. Also shown is the bulk macroscopic C4F10 condensation curve (solid black line). Vertical dashed lines show the main phase transition temperature of the coating lipid. The shaded regions to the right represent the conditions where microbubbles fully dissolved rather than condensing. The difference between the experimental microbubble condensation pressure and the bulk theory was statistically significant utilizing a P-value of 0.001 with a paired t-test.

We next investigated the condensation behavior of C_4F_{10} microbubbles coated with different lipid shells by constructing temperature-pressure phase diagrams that demark the boundaries between gas microbubbles and liquid nanodrops and between condensation (with partial dissolution) and full dissolution (Figure 3.12). Note that we only observed condensation at $\dot{p}$=34.5 kPa s^{-1}; these diagrams do not include the conditions for re-vaporization.

The plots in Figure 3.12 show the experimental microbubble data, the measured condensation curves for macroscopic C_4F_{10} (solid line) and the lipid main phase transition temperatures (vertical dashed lines). The shaded regions to the right of the vertical lines demark the onset of complete dissolution. The plots in Figure 3.12 show a consistent difference between the experimental and theoretical condensation pressures across all chain lengths. In each case, the pressure required for condensation was statistically greater ($P \leq 0.001$) than that predicted for macroscopic C_4F_{10}. This increased over-pressure, as mentioned previously, is the negative of surface tension. It has been proposed that a negative surface tension is necessary for microbubbles to remain stable below their equilibrium radius.[26–28] As mentioned above, this resistance to condensation could also be due to additional work needed to wrinkle and collapse the lipid monolayer shell. The plots in Figure 3.12 also show that the behavior of the microbubbles coated with longer lipids (C18, C20, C22 and C24) transitioned from condensation (with partial dissolution) to full dissolution as the temperature approached the lipid T_m (equivalently, an increase in T_r). This was expected because lipid shells become weaker and more permeable as they soften.[4,12] Surprisingly, C18 microbubbles appeared to be more prone to dissolution relative to its T_m under these conditions. Additionally, only C14 or C16 microbubbles were able to condense above their T_m. These results were highly reproducible experimentally.

The difference between the experimental and theoretical condensation pressures (ΔP) is plotted in Figure 3.13A for different lipid acyl chain lengths at T_r = 0.4, 0.6, 0.8 and 1.0. The magnitude of ΔP ranged from 20 to 150 kPa. Note that, for a given reduced temperature (e.g., T_r = 0.4), the pressure difference tended to increase with acyl chain length, except for C24. The trend is seen more clearly when comparing the surface over-pressure (Π) in Figure 3.13B. This trend is

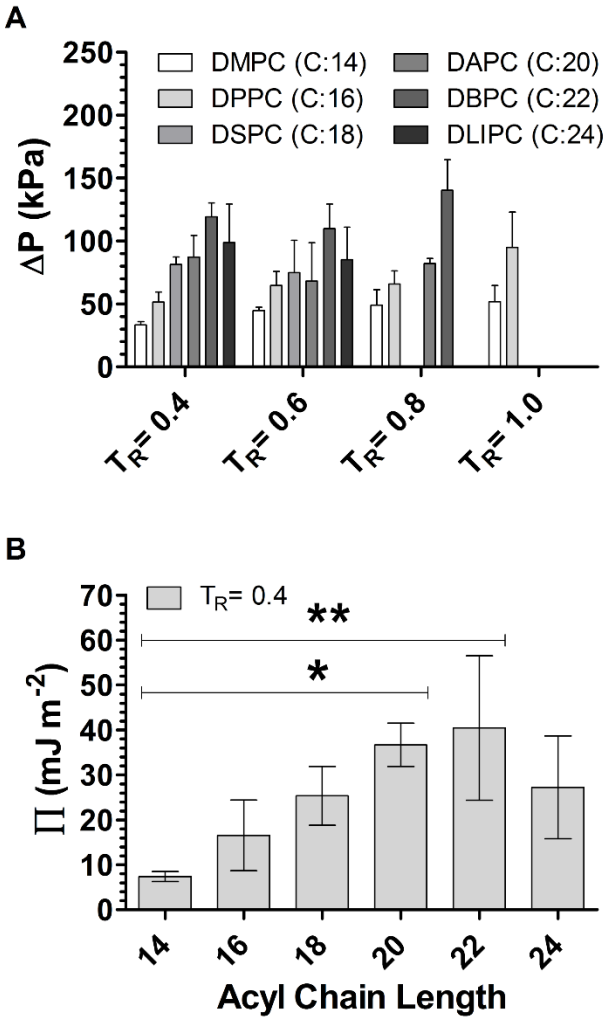

Figure 3.13. Effect of the lipid shell on the pressure required for microbubble condensation. **A** Difference between the experimentally determined microbubble condensation pressure and the theoretical macroscopic bulk C4F10 condensation pressure plotted versus reduced temperature for various lipid encapsulations. **B** The calculated surface pressure assuming a Laplace-Young relationship as a function of lipid acyl chain length for a reduced temperature of T_R = 0.4. * denotes a P-value < 0.05; ** denotes a P-value < 0.01 compared to DMPC : DSPE-PEG2K (9:1).

consistent with prior observations of *in vivo* microbubble circulation,[4] although those experiments were done at constant T instead of constant T_r. C24 is predicted to phase separate from the C18 emulsifier owing to hydrophobic mismatch of the acyl chains. This anomalous result for C24 demonstrates the importance of domain nanostructure on the microbubble shell mechanics.

3.4.8 Comparison to Homogeneous Nucleation for Condensation

In Chapter 2, Section 2.3.2 the theoretical condensation pressure, as a function of temperature, for a pure C_4F_{10} 4 µm diameter bubble undergoing supersaturated homogeneous nucleation is presented. Referring to Figures 3.12 D & F, it can be seen that C20 and C22 provide a substantial resistance to condensation comparable (Fig. 3.14) to the homogeneous nucleation condensation pressures seen in back in Figure 2.11. All of the experimental data points for C20 fall within the limits of the bulk condensation pressure and the pressures predicted by supersaturation homogeneous nulceation theory whereas C22 pressures rise above the supersaturation limit when

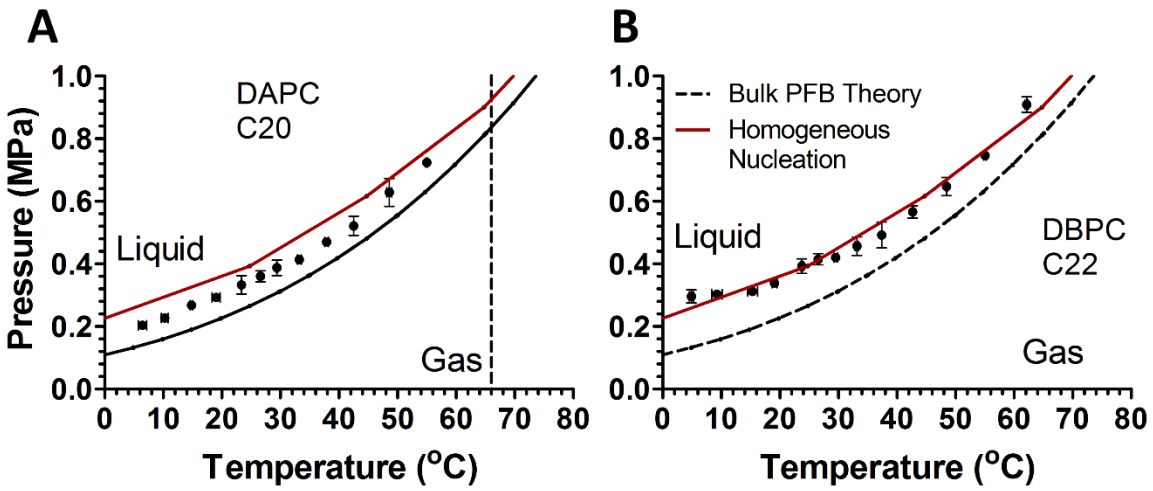

Figure 3.14. Microbubble condensation phase diagrams for (**A**) DAPC and (**B**) DBPC: DSPE-PEG2K (9:1) coated, C_4F_{10}-core microbubbles with mean diameters of 4-5 μm. Also shown is the bulk macroscopic C_4F_{10} condensation curve (solid black line). The theoretical condensation pressure based on the homogeneous nucleation of the liquid phase in a supersaturated vapor is shown (red line) for a 4 µm diameter bubble. Vertical dashed lines show the main phase transition temperature of the coating lipid.

T = 5 and 10 °C. This indicates that heightened condensation pressures of the microbubbles is due to a combination of both shell strength (Figure 3.13) and supersaturation stability. For C22, the lower temperatures possibly provided greater stability which resulted in resistance to condensation past the supersaturation limit. Also, curve for homogeneous nucleation doesn't account for dissolution and a reduction in cross-section. If microbubble condensation pressure could be recorded without dissolution of the microbubble core then perhaps the mechanism responsible for the heightened condensation pressures could be identified.

3.5 Conclusions

Condensation phase diagrams were constructed by tracking individual microbubbles as they were pressurized in a temperature-controlled microscopic viewing chamber, allowing the delineation of regions of microbubble-to-nanodrop condensation and full dissolution. The onset of full dissolution was shifted to higher temperatures with the use of longer acyl chain lipids or supersaturated media. Longer chain lipid shells resisted both mechanical compression and dissolution of the gas core through a pronounced wrinkling-to-collapse transition, thus providing a wider temperature regime for condensation. Surprisingly, the lipid shell may have also provided a mechanical resistance to condensation, shifting the vapor-to-liquid transition to higher pressures than for bulk perfluorobutane and indicating that the lipid shell can provide a negative apparent surface tension under compression. These heightened condensation pressures may have also been a result of the gas core being unable to nucleate liquid phase until higher supersaturation pressures were met. Overall, these phase diagrams will aid in the design and manufacture of vaporizable fluorocarbon nanodrops for various applications, such as diagnostic ultrasound imaging, targeted drug delivery and thermal ablation.

References

[1] Mountford, P. A., Sirsi, S. R., and Borden, M. A., 2014, "Condensation Phase Diagrams for Lipid-Coated Perfluorobutane Microbubbles," Langmuir, **30**(21), pp. 6209–6218.

[2] Borden, M. A., and Longo, M. L., 2004, "Oxygen Permeability of Fully Condensed Lipid Monolayers," J. Phys. Chem. B, **108**(19), pp. 6009–6016.

[3] Kim, D. H., Costello, M. J., Duncan, P. B., and Needham, D., 2003, "Mechanical Properties and Microstructure of Polycrystalline Phospholipid Monolayer Shells: Novel Solid Microparticles," Langmuir, **19**(20), pp. 8455–8466.

[4] Garg, S., Thomas, A. A., and Borden, M. A., 2013, "The effect of lipid monolayer in-plane rigidity on in vivo microbubble circulation persistence," Biomaterials, **34**(28), pp. 6862–6870.

[5] McConnell, H. M., Tamm, L. K., and Weis, R. M., 1984, "Periodic structures in lipid monolayer phase transitions," Proc. Natl. Acad. Sci., **81**(10), pp. 3249–3253.

[6] Marsh, D., 2013, Handbook of Lipid Bilayers, Second Edition, CRC Press.

[7] Morgan, K. E., Allen, J. S., Dayton, P. A., Chomas, J. E., Klibaov, A. L., and Ferrara, K. W., 2000, "Experimental and theoretical evaluation of microbubble behavior: effect of transmitted phase and bubble size," IEEE Trans. Ultrason. Ferroelectr. Freq. Control, **47**(6), pp. 1494 –1509.

[8] Feshitan, J. A., Chen, C. C., Kwan, J. J., and Borden, M. A., 2009, "Microbubble size isolation by differential centrifugation," J. Colloid Interface Sci., **329**(2), pp. 316–324.

[9] L'Annunziata, M. F., 2012, Handbook of radioactivity analysis.

[10] Lide, D. R., 1999, CRC Handbook of chemistry and physics: a ready-reference book of chemical and physical data, CRC press, Boca Raton [etc.].

[11] Marmottant, P., Meer, S. van der, Emmer, M., Versluis, M., Jong, N. de, Hilgenfeldt, S., and Lohse, D., 2005, "A model for large amplitude oscillations of coated bubbles accounting for buckling and rupture," J. Acoust. Soc. Am., **118**(6), pp. 3499–3505.

[12] Borden, M. A., and Longo, M. L., 2002, "Dissolution Behavior of Lipid Monolayer-Coated, Air-Filled Microbubbles: Effect of Lipid Hydrophobic Chain Length," Langmuir, **18**(24), pp. 9225–9233.

[13] Epstein, P. S., and Plesset, M. S., 1950, "On the Stability of Gas Bubbles in Liquid-Gas Solutions," J. Chem. Phys., **18**(11), p. 1505.

[14] Duncan, P. B., and Needham, D., 2004, "Test of the Epstein−Plesset Model for Gas Microparticle Dissolution in Aqueous Media: Effect of Surface Tension and Gas Undersaturation in Solution," Langmuir, **20**(7), pp. 2567–2578.

[15] Ahmar, E. E., Valtz, A., Naidoo, P., Coquelet, C., and Ramjugernath, D., 2011, "Isothermal Vapor−Liquid Equilibrium Data for the Perfluorobutane (R610) + Ethane System at Temperatures from (263 to 353) K," J. Chem. Eng. Data, **56**(5), pp. 1918–1924.

[16] Gaines, G. L., 1966, Insoluble monolayers at liquid-gas interfaces, Interscience Publishers.

[17] Hobbs, S. K., Monsky, W. L., Yuan, F., Roberts, W. G., Griffith, L., Torchilin, V. P., and Jain, R. K., 1998, "Regulation of Transport Pathways in Tumor Vessels: Role of Tumor Type and Microenvironment," Proc. Natl. Acad. Sci., **95**(8), pp. 4607–4612.

[18] Pawley, J., 2010, Handbook of Biological Confocal Microscopy, Springer.

[19] Brown, J. A., and Mears, W. H., 1958, "Physical Properties of n-Perfluorobutane," J. Phys. Chem., **62**(8), pp. 960–962.

[20] Borden, M. A., Kruse, D. E., Caskey, C. F., Zhao, S., Dayton, P. A., and Ferrara, K. W., 2005, "Influence of lipid shell physicochemical properties on ultrasound-induced microbubble destruction," IEEE Trans. Ultrason. Ferroelectr. Freq. Control, **52**(11), pp. 1992–2002.

[21] Kwan, J. J., and Borden, M. A., 2010, "Microbubble Dissolution in a Multigas Environment," Langmuir, **26**(9), pp. 6542–6548.

[22] Kwan, J. J., and Borden, M. A., 2012, "Lipid monolayer dilatational mechanics during microbubble gas exchange," Soft Matter, **8**(17), pp. 4756–4766.

[23] Kwan, J. J., 2012, "Theranostic Oxygen Delivery Using Ultrasound and Microbubbles," Theranostics, **2**(12), pp. 1174–1184.

[24] Borden, M., 2009, "Nanostructural features on stable microbubbles," Soft Matter, **5**(4), pp. 716–720.

[25] Sirsi, S. R., 2013, "Lung Surfactant Microbubbles Increase Lipophilic Drug Payload for Ultrasound-Targeted Delivery," Theranostics, **3**(6), pp. 409–419.

[26] Katiyar, A., Sarkar, K., and Jain, P., 2009, "Effects of encapsulation elasticity on the stability of an encapsulated microbubble," J. Colloid Interface Sci., **336**(2), pp. 519–525.

[27] Sarkar, K., Shi, W. T., Chatterjee, D., and Forsberg, F., 2005, "Characterization of ultrasound contrast microbubbles using in vitro experiments and viscous and viscoelastic interface models for encapsulation," J. Acoust. Soc. Am., **118**(1), pp. 539–550.

[28] Katiyar, A., and Sarkar, K., 2010, "Stability analysis of an encapsulated microbubble against gas diffusion," J. Colloid Interface Sci., **343**(1), pp. 42–47.

Chapter 4

Thermal Activation of Superheated Fluorocarbon Drops

4.1 Introduction

This chapter identifies the conditions necessary for perfluorocarbon (PFC) condensed droplet vaporization. These droplet vaporization parameters and behaviors have been published in Langmuir titled *"Thermal Activation of Superheated Lipid-Coated Perfluorocarbon Drops"*.[1] Vaporization temperatures of nanodrops were measured for multiple PFCs. Thermal activation energy barriers dependent of microbubble shell material were calculated. A comparison to macroscopic and superheated homogeneous nucleation vaporization conditions was made.

4.2 Motivation

The previous chapter examined the pressure requirements for perfluorobutane (C_4F_{10}) microbubble condensation and found that saturation of the microbubble gas core occurred at higher pressures than for macroscopic C_4F_{10}. This method of microbubble condensation developed by Sheeran et al.[2] has been utilized for C_3F_8 and C_4F_{10} droplet formation owing to their low vaporization

temperatures. With boiling temperatures below room temperature, these microbubble condensed droplets (MCDs) are superheated and require an activation energy for phase change. Sheeran et al.[3] reduced the threshold acoustic intensity for vaporization of MCDs to clinically allowable limits by manipulation of the core material. Additionally, Dove et al.[4] reduced the threshold optical fluence for vaporization of gold nanoparticle-coated MCDs by manipulation of the core material. However, the effect of the lipid shell material on vaporization has not been studied.

Here, we report on the effects of lipid acyl chain length on the thermally induced vaporization of C_3F_8 and C_4F_{10} nanodrops. A custom optical chamber was used to control temperature and pressure while measuring the transmitted light through an MCD suspension during condensation and re-vaporization. The presence of condensed nanodrops and re-vaporized microbubbles was verified using dynamic light scattering and electrical impedance sizing measurements. Our results show that lipid composition can significantly impact the thermal activation energy and stability of perfluorocarbon MCDs. Finally, the reversibility of condensation and vaporization was examined by subjecting engineered MCDs to 10 complete phase-shift cycles.

4.3 Materials and Methods

4.3.1 Microbubble Synthesis

Fluorocarbon microbubbles coated with saturated diacyl phosphatidylcholine (PC) of different acyl chain lengths were synthesized to explore the effects of lipid cohesion on the thermally induced re-vaporization and dissolution of MCDs. All phospholipids were purchased from Avanti Polar Lipids (Alabaster, AL), unless otherwise noted, and stored at -20 °C prior to microbubble fabrication. Microbubbles were generated from a lipid suspension comprising 90 mol% of the

main PC component and 10 mol% of the emulsifier, 1,2-disteroyl-*sn*-glycero-3-phosphoethanolamine-N-[methoxy(polyethylene glycol)-2000] (DSPE-PEG2000) (NOF America, White Plains, NY). The following six different PC lipids were used for the comparison of cohesion: 1,2-dimyristoyl-*sn*-glycero-3-phosphocholine (DMPC, C14), 1,2-dipalmitoyl-*sn*-glycero-3-phosphocholine (DPPC, C16), 1,2-distearoyl-*sn*-glycero-3-phosphocholine (DSPC, C18), 1,2-diarachidoyl-*sn*-glycero-3-phosphocholine (DAPC, C20), 1,2-dibehenoyl-*sn*-glycero-3-phosphocholine (DBPC, C22), and 1,2-dilignoceroyl-*sn*-glycero-3-phosphocholine (DLiPC, C24). The lipid mixtures were suspended in 100 mL of 150 mM NaCl, 0.2-μm cold-filtered phosphate buffered saline (PBS) pH 7.4 (Sigma-Aldrich, St. Louis, MO) at a total lipid concentration (PC + DSPE-PEG2000) of 2 mg mL^{-1}. Dispersion and mixing of the lipids was accomplished by heating to 10 °C above the main phase transition temperature (T_m) of the PC lipid [DMPC (23 °C); DPPC (41 °C); DSPC (55 °C); DAPC (66 °C); DBPC (75 °C); DLIPC (80 °C)].[5] Microbubbles were generated in the lipid suspension by probe sonication at room temperature and then size-selected to 4-5 μm diameter, as previously described.[6,7] Size distributions and concentrations of the probe-sonicated microbubbles were measured by electrical impedance sensing using the MultiSizer 3 (Beckman Coulter, Brea, CA), which was found to be more accurate than optical extinction.[8] For enhanced stability during condensation and re-vaporization, all experiments were done in C_4F_{10} (or C_3F_8) saturated PBS solution.[7] This was accomplished by stirring and degassing PBS under house vacuum for 8 h and then re-pressurizing it by filling the head space with C_4F_{10} (or C_3F_8) and stirring for 24 h, all at room temperature.

4.3.2 Microbubble Condensation and Re-Vaporization

A light extinction experiment was developed to monitor populations of microbubbles being (1) converted to nanodrops by pressurization at room temperature and then (2) re-vaporized into

microbubbles by heating and rapid depressurization. A custom chamber was designed to simultaneously control pressure (up to 1.5 MPa absolute) and temperature (20 to 75 ^{o}C), to mix the suspension, and to allow light to pass through the chamber to measure optical extinction (Fig. 4.1). Temperature was monitored by a k-type thermistor (Omega, Stamford, CT) and controlled with a proportional-integral (PI) controller in LabView (National Instruments, Austin, TX) connected to a resistance heating cartridge (Marathon Heater TD25010A-14Q, Del Rio, TX). Chamber pressure was measured with a pressure transducer (Transducers Direct TDH30, Cincinnati, OH) and delivered or released with an on-off type solenoid valve (Omega, Stamford,

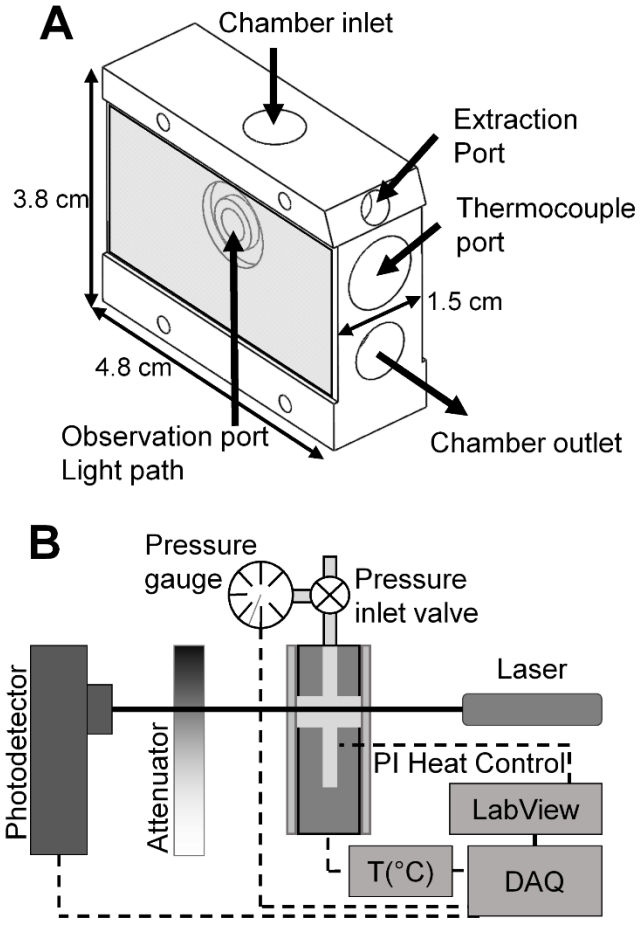

Figure 4.1. (A) Pressure chamber capable withstanding 1.5 MPa of hydrostatic pressure with an optical window that allows for transmittance of light. **(B)** Experimental apparatus for the simultaneous control of hydrostatic pressure and temperature, and measurement of transmitted light intensity based on microbubble concentration.

CT). Optical energy was delivered with a 650 nm laser (Alpec 4001, Sunnyvale, CA) to a photodetector (Thor Labs, DET100A. Newton, NJ) after passing through the chamber and a variable attenuator (Thor Labs, NDL-10C-2, Newton, NJ). Photodetector data were recorded in LabView, time averaged over 50 ms, and then filtered using a Butterworth digital low-pass filter in Matlab (Mathworks, Natick, MA) with a cutoff frequency of 0.5 Hz. The chamber was positioned above a magnetic mixing plate (Corning PC-210, Tewksbury, MA) so that the suspension could be stirred during heating.

The range of temperatures required for nanodrop re-vaporization was determined by the following steps: (1) The variable attenuator was set such that the amount of light transmittance for which no microbubbles were present in the chamber was set to 90% of the maximum voltage detectable by the photodetector. (2) 1 mL of microbubbles at a concentration of 2×10^8 mL^{-1} was delivered into the chamber via the chamber inlet port. This concentration was the minimum that resulted in total extinction of transmitted light through the chamber (13.4% of the maximum photodetector voltage). The chamber inlet and outlet valves were then closed. (3) The sample was rapidly pressurized at room temperature (25 °C) to condense the microbubbles into nanodrops. The pressure was set to exceed the minimum microbubble condensation pressure for C_4F_{10} at 25 °C (350 kPa), as previously measured.[7] In this work, the minimum microbubble condensation pressure for C_3F_8 at 25 °C was determined to be 780 kPa. Condensation was observed as a visual change in the suspension from opaque to transparent and confirmed by the optical measurement system as an increase in light transmission from 13.4% to 90% of the maximum voltage of the photodetector. (4) The chamber pressure was relieved to atmospheric (83.8 kPa), and heat was supplied to the chamber at a linear rate (0.5 °C s^{-1}). The minimum temperatures (55 °C for C_4F_{10}

and 30 °C for C_3F_8) were determined for the onset of nanodrop re-vaporization by a observing a rapid decrease in the transmitted light intensity.

In subsequent experiments, the chamber pressure was maintained at a constant value following microbubble condensation (500 kPa for C_4F_{10} and 780 kPa for C_3F_8), and the suspensions were heated to a specified temperature (55 to 75 °C for C_4F_{10} and 30 to 50 °C for C_3F_8 in 5 °C increments). Once the specified temperature was reached, the pressure was rapidly relieved back to atmospheric (83.8 kPa). A rapid drop in light transmittance was observed upon depressurization as nanodrops vaporized back into microbubbles.

4.3.3 Nanodroplet and Microbubble Sizing

To obtain size distributions of MCDs, 1 mL of DBPC:DSPE-PEG2000 C_3F_8 microbubbles were delivered into the chamber at a concentration of $5x10^8$ mL^{-1} and condensed by increasing the pressure to 780 kPa (~1,500 kPa s^{-1}). The resulting nanodrops were extracted from the chamber through the port shown in Figure 1A. 12 µL of the resulting solution was placed in a low-volume quartz cuvette (Malvern ZEN2112, Worcestershire, UK) and sized using dynamic light scattering (Malvern Nano-S90).

To obtain size distributions of re-vaporized MCDs, 1 mL of DBPC:DSPE-PEG2000 C_3F_8 microbubbles were flowed into the chamber at a concentration of $5x10^8$ mL^{-1} and condensed by stepping the pressure to 780 kPa. The chamber was then heated to 40 °C at a rate of 0.5 °C s^{-1}. Once the temperature had reached steady state, the pressure was relieved and the resulting solution was removed immediately through the extraction port. Extracted microbubbles were quenched in an ice bath (1 °C) to reduce the rate of microbubble dissolution. 50 µL of the re-vaporized solution was then measured by the MultiSizer 3.

4.3.4 Determination of Kinetic Rate Constants

A simple model was developed to decouple the rates of nanodrop vaporization and microbubble dissolution, which each contribute differently to the optical time-intensity data. We first assumed that all of the microbubbles were condensed into nanodrops by pressurization at room temperature. This assumption is valid if the pressurization rate was sufficiently high to prevent microbubble dissolution.[7] The concentration of re-vaporized microbubbles was determined from the transmitted light data by use of the Beer-Lambert law:

$$\frac{I}{I_{\max}} = e^{-l \cdot \alpha_b} \tag{4.1}$$

where I is the measured light intensity on the photodetector, I_{max} is the light intensity when no microbubbles were present (90% max voltage), l the path length (1.5 cm), and α the light attenuation coefficient of the microbubbles. It was assumed that light extinction from the nanodrops was negligible compared to that of the re-vaporized microbubbles. The light attenuation coefficient was:

$$\alpha_b = \sigma_b \cdot C_b \tag{4.2}$$

having σ_b be the scattering cross section of a bubble and C_b the bubble concentration. It was assumed that droplet vaporization for the formation of bubbles was very rapid and that size had little effect on the amount of light scattered during the re-vaporization process. Knowing dissolution occurs over a larger period of time, the average size of the bubble population and the amount of light it scatters during dissolution was approximated and taken into account (Figure 4.2). Microbubbles dissolved at a pseudo-zeroth order rate according to Epstein-Plesset[9,10] and is described by Duncan and Needham[10] to be:

$$\frac{dR}{dt} = -Dk_h BT \frac{1 - f + \frac{2M_w\gamma}{\rho BTR}}{1 + \frac{4M_w\gamma}{3\rho BTR}} \left[\frac{1}{R}\right] \tag{4.3}$$

assuming constant surface tension. For Figure 4.2A , the initial radius is for a 2.5 μm bubble dissolving at 35 °C (*T*). *D* is the diffusion coefficient of the gas (C_4F_{10}) in the medium (water, 4.935 x 10^{-10} m^2s^{-1}),[11] k_h is the Henry's constant for the gas in water (6.9 x 10^{-5} gm^{-3} Pa^{-1}),[11] *B* is the ideal gas constant (8.3144 m^3 Pa K^{-1} mol^{-1}), *f* is the ratio of the initial gas concentration to that at saturation (saturated, *f* = 1 at 25 °C), M_w is the gas molecular weight (238.0268 g mol^{-1}), γ is the surface tension (25 mN m^{-1}), and ρ is the gas density (11210 g m^{-3}). Note that, among other effects, increasing temperature reduces the solubility of PFB in water, leading to a supersaturated solution (f > 1 for T > 25 °C) and reduced rate of dissolution.

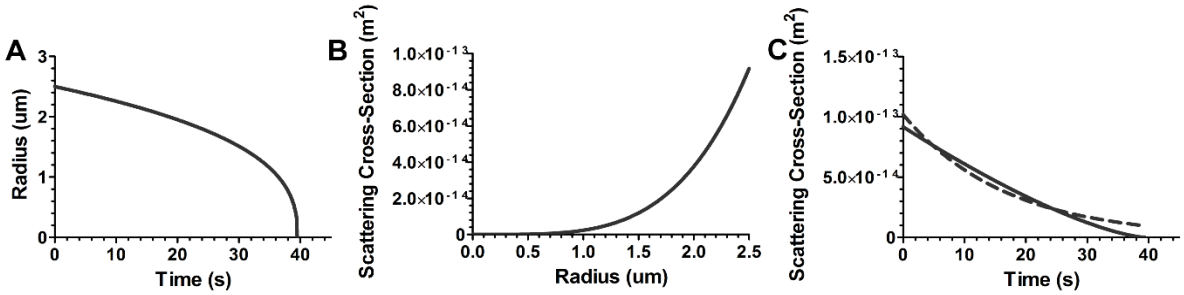

Figure 4.2. (A) The radius vs. time curve based on the Epstein-Plesset model for a 2.5 μm bubble with an interfacial surface tension of 25 mN m^{-1}. **(B)** The scattering cross-section vs. microbubble size based on anomalous diffraction theory.[2] **(C)** The scattering cross-section vs. time for a 2.5 μm bubble dissolving with an interfacial surface tension of 25 mN m^{-1} (solid) along with its exponential decay fit (dashed).

The amount of light scattered by a microbubble increases exponentially with radius (*R*) specifically as:

$$\sigma = Q(r) \cdot \pi R^2 \tag{4.4}$$

with σ being the optical cross-section of a particle and *Q* being:

$$Q(r) = 2 - \frac{4}{p}\sin(p) + \frac{4}{p^2}(1 - \cos(p)) \tag{4.5}$$

which is the efficiency factor of scattering for the particle based on the anomalous diffraction theory.[12] The *p* term represent the effective radius and is defined to be:

$$p = \frac{2\pi R}{\lambda}(n - 1) \tag{4.6}$$

with λ being the wavelength of light (650 nm) and *n* being the refractive index of gaseous perfluorobutane (1.003). Figure 4.2B shows the dependence of σ on *R*. These relationships were combined which lead to a first order response of scattering cross-section of a microbubble versus time (Figure 4.2C).

It was assumed that the amount of light attenuated versus time for a microbubble sample of constant concentration (C_{DO}) and decaying scatter (σ_b) was equivalent to a microbubble sample of decreasing concentration (C_b) and constant scatter (σ_o):

$$\alpha_b = \sigma_O C_b(t) = C_{DO}\sigma_b(t) \tag{4.7}$$

The concentration of condensed droplets (C_D [particles m^{-3}]) and re-vaporized microbubbles (C_b [particles m^{-3}]) at any instant following depressurization was found by assuming the first-order rate equations:

$$\frac{dC_D}{dt} = -k_1 C_D \tag{4.8}$$

$$\frac{dC_b}{dt} = k_1 C_D - k_2 C_b \tag{4.9}$$

which provided a droplet concentration of:

$$C_D = C_{DO} e^{-k_1 t} \tag{4.10}$$

Knowing that the concentration of bubbles present was related to the difference between bubbles formed and bubbles dissolved:

$$C_b = C_{DO}\frac{k_1}{k_2 - k_1}\left(e^{-k_1 t} - e^{-k_2 t}\right) \tag{4.11}$$

where k_1 is the rate constant of re-vaporization (s^{-1}), t is time (s) and k_2 as the rate constant of microbubble dissolution after re-vaporization (s^{-1}). From combining equations (4.1), (4.2) and (4.7) with (4.11), the attenuation and concentration of microbubbles were related to the amount of transmitted light. Prior to condensation, the ratio of light intensities was defined as the light intensity of microbubbles initially injected into the chamber (I_o) ($C_D = 0$; $\alpha_b = \alpha_o = \sigma_o C_{DO}$) over the maximum transmitted light:

$$\frac{I_o}{I_{\max}} = e^{-l\cdot\alpha_O} \tag{4.12}$$

Dividing equation (4.1) by (4.12) gave:

$$\frac{I}{I_o} = \frac{e^{-l\cdot\alpha_b}}{e^{-l\cdot\alpha_O}} = e^{l\cdot(\alpha_O - \alpha_b)} = e^{l\cdot\sigma_O(C_{DO} - C_b)} \tag{4.13}$$

Combining equations (4.1), (4.11) and (4.12) and taking the natural logarithm of both sides provided:

$$\ln\left(\frac{I}{I_o}\right) = -\ln\left(\frac{I_o}{I_{\max}}\right)\cdot\left(1 - \left(\frac{k_1}{k_2 - k_1}\left(e^{-k_1 t} - e^{-k_2 t}\right)\right)\right) \tag{4.14}$$

This equation provided a means of relating the transmitted light intensity to the kinetic rate constants of nanodrop vaporization and microbubble dissolution. The rate constants were determined by fitting Equation 4.14 to the experimental light intensity data in OriginPro (OriginLab, Northampton, MA).

4.3.5 Analysis of Vaporization Kinetics

The experiments provided time-intensity data, and hence kinetic rate constants (k_1 and k_2), for a range of temperatures at constant pressure (83.8 kPa). The kinetic rates for vaporization were then analyzed by the Arrhenius equation:

$$k_1 = A_1 e^{-E_a / RT} \tag{4.15}$$

where A_1 is a frequency factor (s^{-1}), E_a is the apparent phase-shift activation energy (J/mol), R is the ideal gas constant (8.3144 J K^{-1} mol^{-1}) and T is absolute temperature (K). The apparent phase-shift activation energy is then experimentally determined by the slope of an Arrhenius plot [ln(k_1) versus T^{-1}]:

$$E_a = -R \cdot \left(\frac{\partial \ln k_1}{\partial \left(\frac{1}{T} \right)} \right) \tag{4.16}$$

The activation energies were determined for each lipid coating using at least three measurements per sample and three samples per composition.

In addition to nucleating a gas embryo in a superheated liquid, the energy barrier associated with expanding the collapsed lipid monolayer and possible bilayers was predicted. The total monolayer cohesion energy (U_A) for a given area change (ΔA) is:

$$U_A = \frac{U}{N_O * A_L} \cdot \Delta A \tag{4.17}$$

where U is the molar van der Waals cohesion energy (J mol^{-1}), N_o is Avagadro's number and A_L is the area per lipid molecule.[13] The molar cohesion energy is a function of acyl chain length (n) according to the following relation for a saturated diacyl lipid:

$$U = 2nU_{CH2} \tag{4.18}$$

where U_{CH2} is the cohesion energy per methylene group, given by the following series:[13]

$$U_{CH2} = \frac{3\alpha_0^2 h\nu}{4(4\pi\varepsilon_0)^2}\left[\frac{6}{\sigma^6} + \frac{12}{\left[\sigma^2 + l^2\right]^3} + \frac{12}{\left[\sigma^2 + (2l)^2\right]^3} + \ldots\right]\frac{N_O}{2} \tag{4.19}$$

where $\alpha_o/4\pi\varepsilon_o$ is 1.84x10^{-30} m^3, $h\nu$ is 1.67x10^{-18} J, σ is the CH_2-CH_2 packing distance, and l is the CH_2-CH_2 bond length (0.127 nm). This gives a molar cohesion energy U of 169 to 289 kJ mol^{-1} for C14 to C24. A_L is given by the following relation for 2-D hexagonal close-packed (HCP) cylinders (91% packing density):[7]

$$A_L = \frac{2\pi}{3.64}\cdot\sigma^2 \tag{4.20}$$

The value of A_L is therefore estimated to be 40 nm^2, giving a value of σ equal to 4.81x10^{-9} m. The total area change for a 400-nm radius droplet converting to a 2-μm radius bubble is 4.83x10^{-11} m^2. Therefore, the lipid-shell cohesive energy barrier to nanodrop vaporization is estimated to range between 104 and 178 kJ mol^{-1} for C14 to C24. This energy along with any resistance to vaporization provided by the core was assumed to be the entire activation energy.

4.3.6 Analysis of Dissolution Kinetics

Microbubble dissolution typically is analyzed by the theory of Epstein and Plesset[9] or subsequent modifications to this theory to include terms for the lipid shell.[14] These analyses show an accelerating rate of dissolution with decreasing microbubble size owing to increasing surface area-to-volume and Laplace pressure. Here, dissolution was approximated as a first-order rate process, in which microbubbles instantly dissolve at a certain average rate (k_2) determined by the optical time-intensity data.

4.3.7 Probability of Vaporization

Microbubble stability during condensation and re-vaporization was examined by the probability of achieving complete nanodrop-to-microbubble conversion. This probability was defined as:

$$P_{revap} = \frac{I_{\max} - I_{\min}}{I_{\max} - I_o} \tag{4.21}$$

where I_{max} is the maximum light intensity achieved during condensation, I_{min} is the minimum light intensity achieved during re-vaporization, and I_o is the light intensity observed pre-condensation following injection of the initial microbubble suspension (90% of max voltage). The re-vaporization probability data were fit to a Gaussian cumulative distribution percentage curve with a maximum of 100% and minimum of 0%, using Prism software (Graph Pad, La Jolla, CA). The parameter P_{revap} provides two measures of stability: the probability of nanodrop-to-microbubble re-vaporization and the degree of microbubble dissolution. For example, a rapidly dissolving microbubble suspension cannot achieve a maximum P_{revap} of 100%.

4.3.8 Reversibility of Microbubble Condensation

The phase-shift repeatability of the microbubble condensation and re-vaporization process was examined by cycling pressure to achieve these two states sequentially. For these experiments, DBPC:DSPE-PEG2000 C_3F_8 core microbubbles were injected into the chamber at a concentration of 2 x 10^8 mL^{-1} in a PBS solution super-saturated C_3F_8, as previously described,[7] to inhibit dissolution. The chamber was pressurized to 780 kPa for condensation at room temperature and then heated to 40 °C, where the pressure was rapidly relieved to atmospheric (83.8 kPa) to induce re-vaporization for ~10 s. The pressure then was increased to 1.4 MPa and held for ~10 s to induce re-condensation at 40 °C. The re-condensation and re-vaporization cyclic process was carried out a total of 10 times. A hand-held microscope (Dino-Lite AM-3011, Torrance, CA) was oriented on

the incident side of the chamber to capture images without affecting the light transmission measurements.

4.4 Results and Discussion

4.4.1 Microbubble and Nanodroplet Size

These superheated nanodrops are metastable in the liquid state at standard temperature and pressure,[2,7] and must be thermally activated to vaporize back into microbubbles. Particle size distributions were measured to confirm C_3F_8 microbubble condensation at room temperature (25

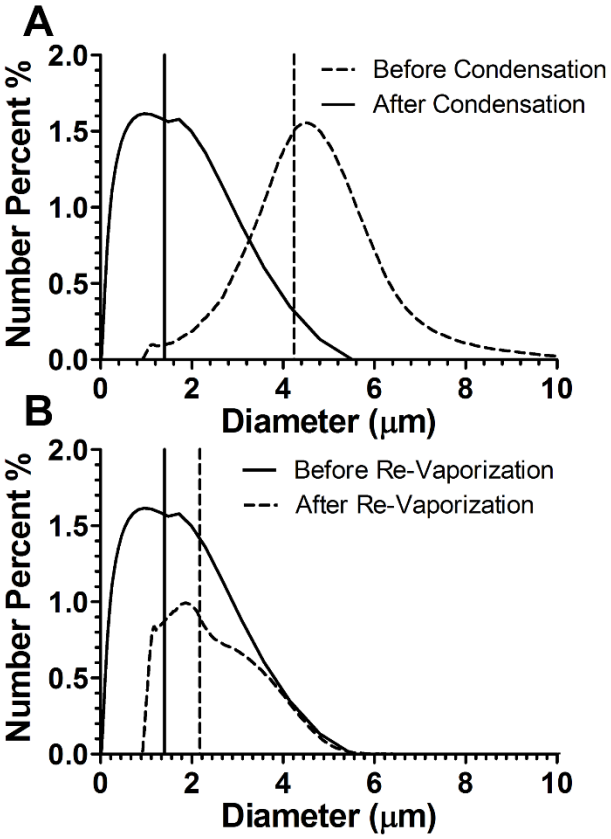

Figure 4.3. (A) MultiSizer 3 and DLS size distributions for DBPC:DSPE-PEG2000 C_3F_8 size-isolated microbubbles before (dashed) and after (solid) condensation. **(B)** MultiSizer 3 and DLS size distributions for the re-vaporized microbubbles (dashed) formed from the microbubble condensed nanodrops (solid).

^{o}C) and elevated pressure (780 kPa), and then re-vaporization at elevated temperature (40 ^{o}C) and atmospheric pressure (83.8 kPa). Figure 4.3 shows that the original size-isolated microbubbles had a peak diameter from 4-5 µm (4.24 ± 0.72 µm, average ± standard deviation). The condensed nanodrops had a peak diameter near 1 µm (1.40 ± 0.91 µm), as expected from the change in molar volume from the gas to liquid phase. The re-vaporized microbubbles had an average diameter of 2.18 ± 0.67 µm, which was about half that of the original microbubbles. Additionally, the total microbubble concentration dropped from $5x10^{8}$ to $2x10^{6}$ mL^{-1}. This decrease in microbubble concentration and size was likely due to dissolution during re-vaporization, extraction from the chamber, handling and particle size measurement. Despite the loss in microbubble size and number, the results showed clearly that these microbubbles could be hyperbarically condensed and then thermally re-vaporized.

4.4.2 Analysis of Thermal Re-Vaporization Kinetics

Figure 4.4 shows representative optical time-intensity curves with the corresponding pressure and temperature in the chamber. Initially, the optical intensity was very low owing to microbubble scattering. Condensation corresponded to a rapid increase in light transmittance. The minimum temperature to induce re-vaporization of condensed C_4F_{10} microbubbles at room temperature was determined by dropping the gauge pressure to zero (Fig. 4.4A, blue) and heating the nanodrop solution at a rate of 0.5 ^{o}C s^{-1} to ~80 °C (Fig. 4.4A, red). The onset of re-vaporization was marked by a significant decrease in transmitted light (Fig. 4.4A, green). For all C_4F_{10} microbubbles, the minimum re-vaporization temperature was found to be ~55 °C (328 K). This result shows that the nanodrops are superheated, as this value is ~20% higher than the equilibrium boiling temperature for C_4F_{10} (T_b = -1.7 ^{o}C). Dissolution was marked by a gradual return to high transmittance. The temperature corresponding to the inflection in the time-intensity curve from negative

(vaporization) to positive (dissolution) slope was observed to be 75 °C (348 K). This range, 55 to 75 °C, marked the regime of thermal activation for our lipid-coated C_4F_{10} MCDs.

In subsequent experiments, the pressure was maintained at ~500 kPa during heating, and vaporization was induced by a rapid decrease in pressure at this elevated temperature (Fig. 4.4C).

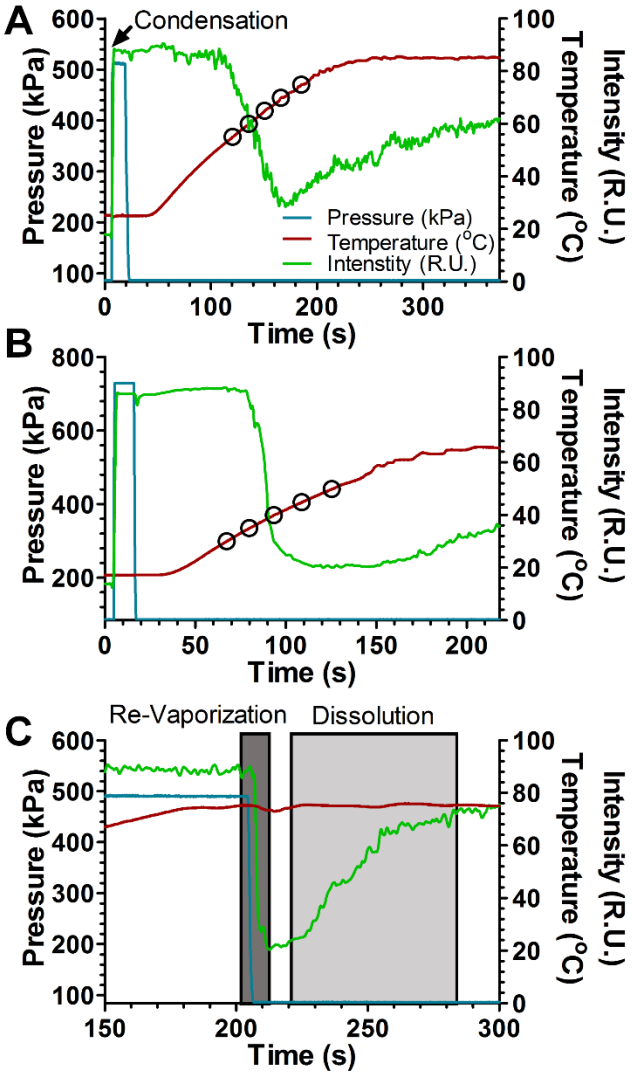

Figure 4.4. Time-intensity curves for DBPC:DSPE-PEG2000 C_4F_{10} **(A)** and C_3F_8 **(B)** microbubbles undergoing heating at ~0.5 °C s^{-1} to 80 °C for the purpose of defining the vaporization and dissolution temperature ranges. Circles represent temperatures for which re-vaporization rates were measured. **(C)** Re-vaporization rate plot depicting the regions of re-vaporization and dissolution for DBPC:DSPE-PEG2000 C_4F_{10} re-vaporized microbubbles at 75 °C. Pressure (blue), temperature (red) and intensity (green) are plotted versus time.

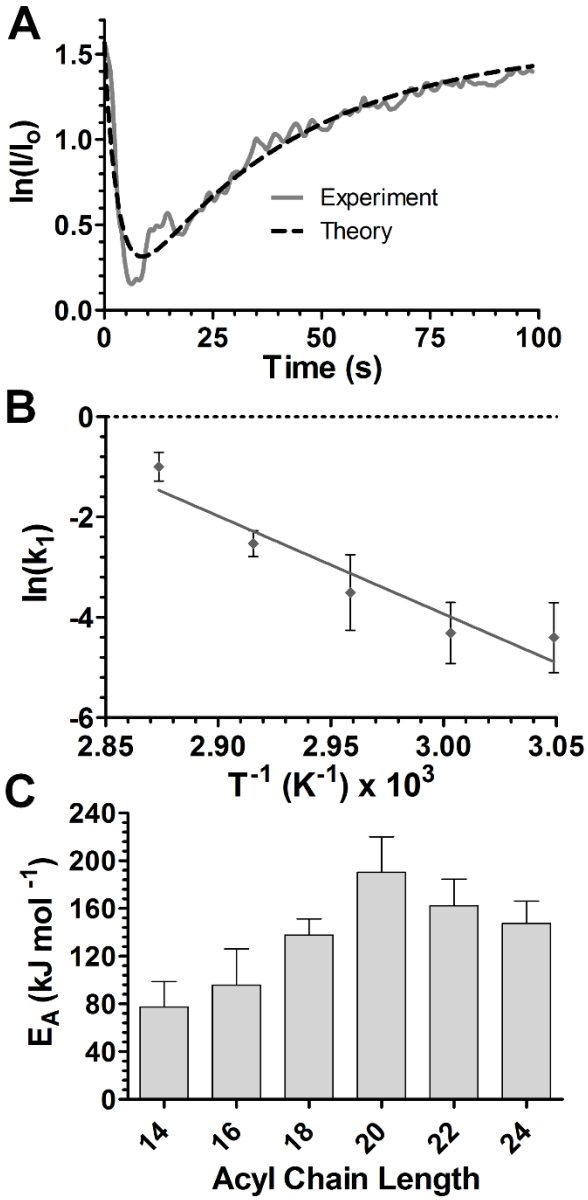

Figure 4.5. **(A)** The natural logarithm of the normalized transmitted light intensity versus time for DBPC:DSPE-PEG2000 C_4F_{10} nanodrops undergoing re-vaporization and dissolution at 75 °C. The experimental and theoretical intensities are represented by the solid and dashed lines, respectively. **(B)** Arrhenius plot for vaporization kinetics of DBPC:DSPE-PEG2000 C_4F_{10} nanodrops. **(C)** The phase-shift activation energy, based on k_1, for all acyl chains (C14-24) C_4F_{10} microbubbles (kJ mol^{-1}). The statistically different MCDs were: $P<0.01$ (**) are C14 vs. C20, C22 and C24. $P<0.05$ (*) are C14 vs. C18, C16 vs. C20 and C22, and C18 vs. C20 and C22.

Once the overpressure was relieved, the light intensity was observed to decrease at a nearly linear rate (Fig. 4.4C, dark shaded region). After some time, the time-intensity plot showed an inflection

and then positive slope, marking the onset of dissolution as a dominant process (Fig. 4.4C, light shaded region).

The first order rate constants (k_1 and k_2) were determined from by fitting the experimental time-intensity curves to equation (10), as shown on Fig. 4.5A. The temperature-dependence of the vaporization rate (k_1) was analyzed by an Arrhenius plot (Fig. 4.5B). DAPC (C20) had the greatest negative slope, whereas DMPC (C14) had the least negative slope (Figure 4.6). These slopes were converted to apparent phase-shift activation energies (E_a) by use of equation (12). The values of E_a increased substantially from DMPC (C14) to DAPC (C20) and then slightly decreased to DLiPC (C24) (Fig. 4.5C). Interestingly, similar trends with respect to acyl chain length from C14 to C24 were seen previously with shell resistance to microbubble condensation,[7] as well as *in vitro* and *in vivo* microbubble stability,[15] suggesting an interplay between intermolecular forces and microstructure. Taken together, these data suggest that lipid shell cohesion affects the re-vaporization energy, in addition to condensation pressure,[7] stability against dissolution,[15] gas permeability[16] and mechanical properties.[17]

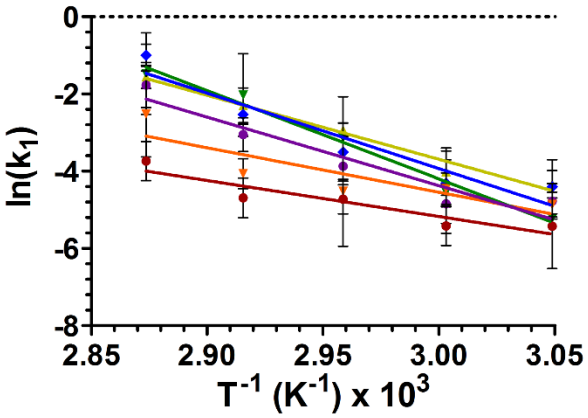

Figure 4.6. The natural logarithm of the re-vaporization rate for [DMPC (red), DPPC (orange), DSPC (yellow), DAPC (green), DBPC (blue) and DLIPC (purple)] : DSPE-PEG2K (9:1) coated, C4F10 core, microbubble condensed nanodrops are presented dependent of the constant inverse temperature of the solution during re-vaporization.

It is interesting to compare these experimental activation energies (E_a ranging ~70 kJ mol^{-1} for C14 to ~190 kJ mol^{-1} for C20) to the energy required to nucleate a stable vapor embryo inside a homogenous liquid. A vapor embryo is stable in a superheated liquid if it grows to the critical size, beyond which the Laplace pressure is too low to stifle further growth.[18,19] Once a stable vapor embryo forms, it can grow rapidly to vaporize the remaining liquid in the droplet. Vaporization proceeds with the mass flux of liquid perfluorocarbon molecules evaporating into the embryo, which is driven by the entropy gain. Surprisingly, all apparent activation energies measured here were much higher than the Gibbs free energy of critical embryo formation (ΔG_e ~ 1.2 kJ mol^{-1}, Ch. 2 Equation 2.33). This result indicated that other energy barriers were also inhibiting the vaporization process. Thus, the increase in E_a observed between C14 and C20, and the large magnitude compared to ΔG_e and the surface energy gain, suggest that lipid monolayer cohesion plays a significant role in damping thermal activation of MCD vaporization.

4.4.3 Expansion and bending during lipid bilayer unfolding

In an attempt to account for the heightened thermal activation energies, the energy of expanding the collapsed lipid shell was determined through calculating the lipid cohesion energies (Equation 4.19). A cartoon schematic of monolayer expansion and lipid bilayer unfolding during nanodrop-

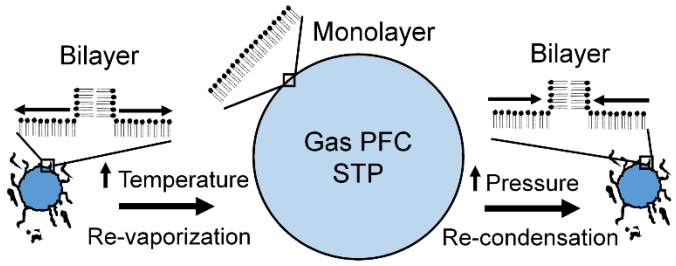

Figure 4.7. Cartoon schematic of a microbubble-condensed nanodrop with the lipid shell during vaporization and subsequent condensation. Shown are surface-associated strands of bilayer that form during condensation must be expanded and unzipped to adsorb as a monolayer onto the vapor microbubble. Excess monolayer then converts back into new bilayer strands upon subsequent condensation.

to-microbubble vaporization is shown in Figure 4.7. The phase change is accompanied by a large (24-fold) change in surface area, which forces the lipid monolayer to expand. However, monolayer expansion requires overcoming the van der Waals cohesion forces between the lipid acyl chains. This would result in an elastic expansion energy that adds to the total energy barrier for vaporization.

Additionally, surface-attached bilayers may unfold to shuttle more lipid to the gas/water interface during expansion. The unfolding process would require bending of the bilayer leaflets to separate the acyl chains, as shown in the cartoon below. This would result in an elastic bending energy that adds to the total energy barrier. In either case, expansion or bending, the acyl chains must be separated, and therefore the monolayer cohesion energy should add significantly to the total energy barrier for nanodrop vaporization.

The mechanism of how lipid cohesion affects MCD vaporization remains unknown. We previously reported microscopy evidence that condensing microbubbles form bilayer collapse strands that appear to remain attached to the droplet surface.[7] Sheeran et al.[3] showed evidence that the lipid is redeposited back onto the re-vaporized MCD. We therefore propose that lipid monolayer and bilayer expansion and bilayer unzipping back into the monolayer may explain the dependence of the vaporization rate on lipid acyl chain length (Fig. 4.7). We estimate the energy required to expand the lipid monolayer to be 134 kJ mol^{-1} (Equation 4.19). We believe that such a lipid cohesion energy barrier provides a reasonable explanation for the measured activation energies and qualitatively explains the dependence on acyl chain length.

4.4.4 Analysis of Dissolution Kinetics

The loss of light extinction following vaporization was likely due to microbubble dissolution, and it was modeled as such in equation (7). All acyl chain lipids, excluding DLiPC (C24), were above

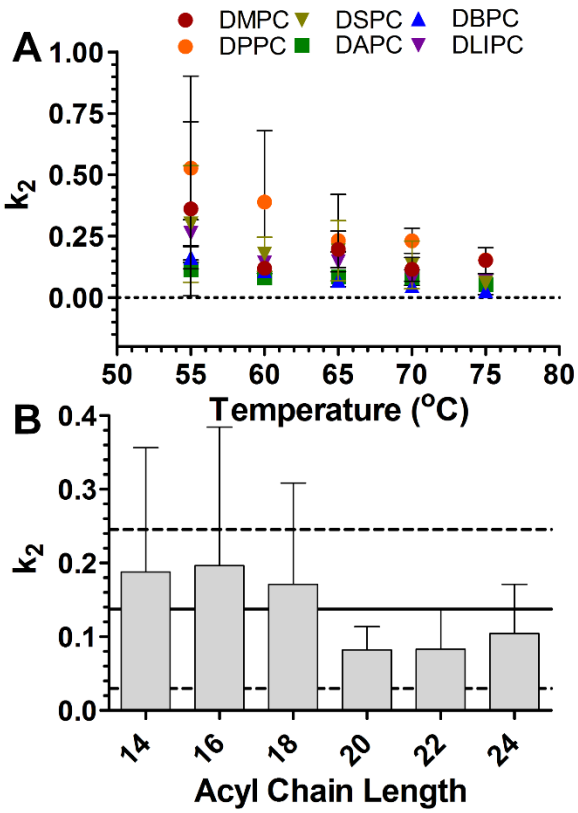

Figure 4.8. (A) The dissolution rate for [DMPC (red), DPPC (orange), DSPC (yellow), DAPC (green), DBPC (blue) and DLIPC (purple)] : DSPE-PEG2000 coated, C_4F_{10} core, re-vaporized microbubbles versus solution temperature. **(B)** The average dissolution rate for all temperatures versus lipid acyl chain length (C14-C24). The average dissolution rate over all chain lengths is presented (solid line) along with the standard deviation (dashed lines).

their main phase transition temperature (T_m) over the 55 to 75 °C experimental range.[5,15] Microbubbles are known to be substantially less stable when temperature exceeds T_m owing to weaker shell cohesion.[17] The kinetic energy of the permeating C_4F_{10} molecules also increases substantially at these working temperatures.[20] The first order kinetic rate constant for microbubble dissolution (k_2) was determined as a function of temperature for each acyl chain length (Fig. 4.8). Surprisingly, Figure 4.8A shows a general decrease in k_2 with increasing temperature for each acyl chain length. This trend is suspected to be an error introduced by bubble instability and the very simple model employed here. The average rate of microbubble dissolution

across all chain lengths and temperatures was found to be 0.138 ± 0.108 s^{-1} (Fig. 4.8B, solid line). However, Figure 4.8B shows a general decrease in k_2 with increasing acyl chain length from C14 to C20 and then an very small increase from C20 to C24. This follows the trend observed above for E_a and supports previous work on microbubble stability.[15]

4.4.5 Probability of Nanodrop Re-Vaporization

The probability of MCD vaporization was observed to depend on both the degree of superheat of the fluorocarbon liquid[21] and the stability of the original microbubble shell. Microbubble shells with shorter acyl chains (C14 and C16) were seen to reach much lower values for P_{revap} (Fig. 4.9A). In fact, only 20% re-vaporization was achieved for DMPC at 75 °C, and only 45% re-vaporization was reached for DPPC at this temperature. This result indicated the occurrence of rapid microbubble dissolution. Indeed, the re-vaporization rate constants (k_1 ~ 0.03 s^{-1}) were smaller than the dissolution rate constants (k_2 ~ 0.2 s^{-1}) for these lipids. Re-vaporization favors a decrease in I_{min}, whereas dissolution favors an increase in I_{min}. The similar rate constants for both competing phenomena confounded the probability analysis for these two lipids.

On the other hand, microbubble shells with longer acyl chains (C18-C24) achieved near complete re-vaporization (75-90%), which indicated much higher stability (Fig. 4.9B). Indeed, the re-vaporization rate constants (k_1 ~ 0.15 s^{-1}) exceeded the dissolution rate constants (k_2 ~ 0.05 s^{-1}) for these lipids, thus providing a more conclusive analysis of the effect of temperature on re-vaporization probability. Interestingly, the uncertainty of the probability of re-vaporization was higher for C18 and C20 (2.8 - 21%) than for C22 and C24 (1.9 - 14%). Although DSPC and DAPC were stable enough to achieve substantial re-vaporization, their main transition temperatures (55 and 66 °C, respectively) were within the experimental temperature range used here (55 to 75 °C).

Thus, the large uncertainty associated with these two lipids may have been owing to the lipids being in a transitional state between the two monolayer phases.

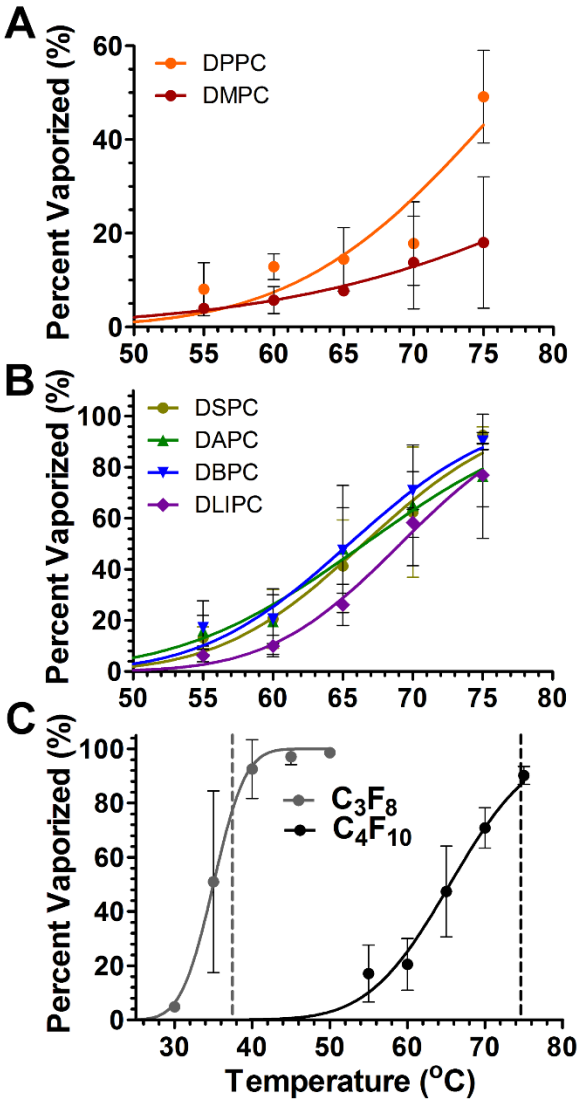

Figure 4.9. Probability of re-vaporization versus temperature for [**(A)** DMPC (red) and DPPC (orange)] or [**(B)** DSPC (yellow), DAPC (green), DBPC (blue) and DLIPC (purple)] C_4F_{10} nanodrops at 55, 60, 65, 70 and 75 °C. **(C)** Probability of re-vaporization versus temperature for DBPC:DSPE-PEG2000 C_3F_8 (grey) and C_4F_{10} (black) nanodrops. Lines represent the Gaussian cumulative distribution curves fit to the experimental data. Vertical dashed lines represent 90% of the critical temperature (72 °C for C_3F_8 and 113 °C for C_4F_{10}).

4.4.6 Effect of the Fluorocarbon

A more volatile perfluorocarbon, C_3F_8 (T_b = -37 ^oC), was used as the microbubble core material to determine if a nanodrop could be tuned for thermal re-vaporization. The lipid composition DBPC:DSPE-PEG2000 was chosen since it was shown to diminish dissolution in the C_4F_{10} experiment reported above (Fig. 4.9B). Here, the same pressure and temperature profiles were used for C_3F_8 (Fig. 4.4B, blue and red). The minimum re-vaporization temperature was found to be 35 °C, and almost complete transmitted light extinction was seen at 40 °C (Fig. 4.4B, green). Interestingly, these C_3F_8 re-vaporized microbubbles appeared to be more stable against dissolution than the C_4F_{10} re-vaporized microbubbles, probably owing to the lower temperatures required for re-vaporization compared to the lipid T_m.

The rapid decompression experiments were carried out for C_3F_8 nanodrops at five separate temperatures: 30, 35, 40, 45 and 50 °C (Fig. 4.4C, circles). The percentage of re-vaporized C_3F_8 microbubbles was measured and compared to C_4F_{10} (Fig. 4.9C). Both C_3F_8 and C_4F_{10} followed Gaussian cumulative distribution trends, but with different threshold temperatures and slopes in the linear regions. Previous studies have predicted and shown that homogeneous nucleation in pure super-heated gases occurs around 89 to 90% of the critical point temperature (72 °C for C_3F_8 and 113 °C for C_4F_{10}).[22–26] Thus, the shift to a lower thermal threshold for C_3F_8 was expected. Interestingly, while near complete re-vaporization of nanodrops occurred at 89-92% for C_3F_8 and 89-90% for C_4F_{10}, C_3F_8 nanodrops provided a much steeper re-vaporization slope than C_4F_{10} nanodrops. This latter result is perhaps another indication that a working temperature well below the lipid T_m provides more reproducible re-vaporization.

4.4.7 Phase Change Reversibility

The reproducibility of condensation and vaporization was tested for DBPC:DSPE-PEG2000 C_3F_8 microbubbles by cycling the pressure between 1.4 MPa and 83.8 kPa at constant temperature (40 °C). Figure 4.10 shows that these microbubbles endured 10 cycles of condensation and vaporization with minimal change in the transmitted light intensity. To verify that the extinction

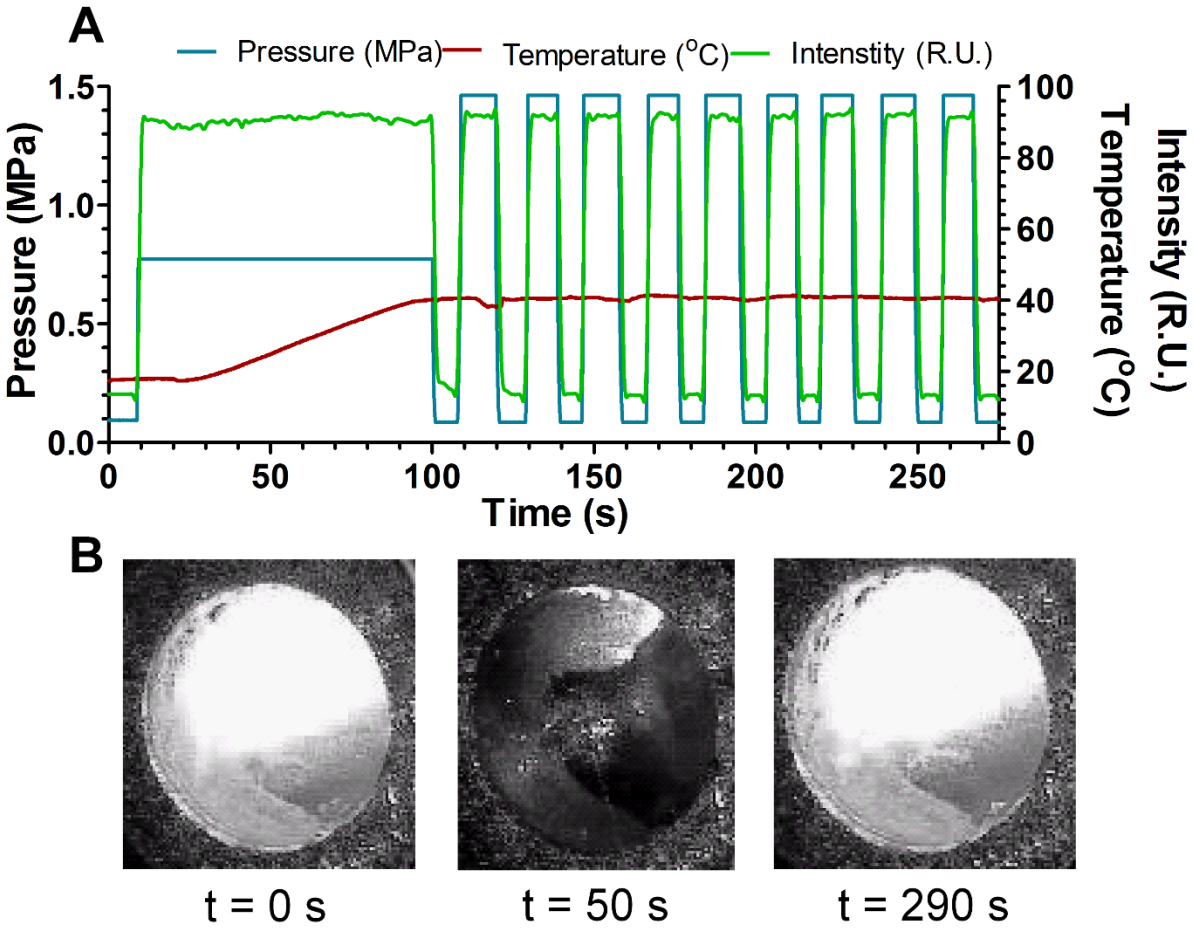

Figure 4.10. **A**) Time-intensity curve for the cyclic condensation/re-vaporization of DBPC:DSPE-PEG2000 C_3F_8 microbubbles at 40 °C. **B)** Images of the chamber window showing the condensation and vaporization of the microbubble emulsion at different time points.

of transmitted light was caused by the re-vaporization of nanodrops, a hand held microscope was used to capture video recording of the cyclic phase-shift process (Figure 4.10B). This exciting

result demonstrates that the condensation/vaporization process can be reversible for this engineered MCD composition.

4.4.8 Comparison to Superheated Homogeneous Nucleation

Referring back to Chapter 2 ,section 2.4.2, the kinetic limit of superheat was defined as the maximum temperature for which a pure liquid can remain in the liquid state. The results in Figure 9C agree with the maximum superheat temperature of 74 °C for C_4F_{10} and is combined with Figure 2.14 in Figure 4.11 for convenience. The maximum limit of superheat is the temperature at which there is enough energy to nucleate an embryo large enough to vaporize the entire droplet. We know from molecular thermodynamics and kinetics that not all the available energy will go into nucleating one embryo, it is dispersed into creating many embryos. The Gibbs free energy for nucleating a vapor embryo large enough to vaporize a nanodrop is inaccurate because it is assuming all of the energy is focused into one nucleate. From kinetic theory, a nucleation flux of approx. 10^{12} embryos m^{-3} s^{-1} is required to definitely form a vapor pocket large enough for vaporization.[18] Although 90% of vaporization is occurring at the critical flux, there is still droplet vaporization occurring far below the equilibrium embryo nucleation rate (Figure 4.11).

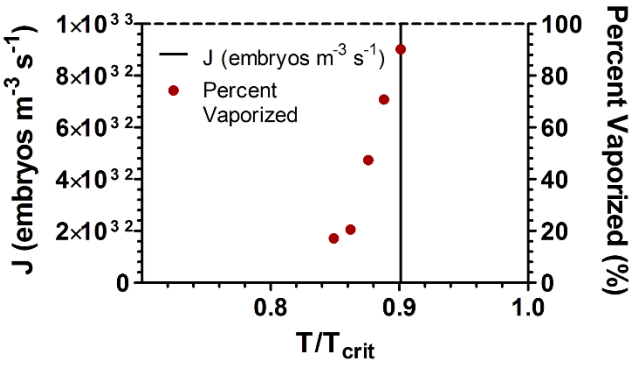

Figure 4.11. Experimental C_4F_{10} droplet vaporization probability (red circles) and vapor embryo nucleation flux rate (black line) versus temperature. Horizontal dashed line represents the nucleation flux required for equilibrium embryo formation. Vertical dashed line represents the spinodal temperature for superheated pure C_4F_{10} liquid (74 °C).

The most likely reasoning for this experimental observation is that not all droplets are undergoing homogeneous nucleation and therefore, mixed-nucleation is the mechanism responsible for the droplet superheated stability.

4.5 Conclusions

The vaporization temperatures for lipid-coated C_3F_8 and C_4F_{10} microbubble-condensed nanoemulsions were determined to be 40 and 75 °C, respectively, by monitoring light transmission through suspensions undergoing controlled temperature and pressure schedules. These vaporization temperatures were at the superheat limit (spinodal), estimated to be 80-90% of the fluorocarbon critical temperature (72 °C for C_3F_8 and 113 °C for C_4F_{10}, under atmospheric pressure).[18] Thus, our experimental results support the view that superheated phase-change agents are stabilized by the metastability of the pure fluid against homogeneous nucleation of a critical vapor embryo. Our data contradict the view of boiling point elevation owing to droplet Laplace pressure via Antoine's equation,[27] which predicts much lower vaporization temperatures (e.g., 16 °C for C_4F_{10} at 2 bar). However, analysis of the vaporization kinetics yielded apparent phase-shift activation energies that were much greater than that predicted by the Gibbs free energy for critical vapor embryo formation; the trend with lipid acyl chain length indicated a significant role for lipid intermolecular cohesion forces in slowing the vaporization process, possibly owing to expansion and unzipping of surface-associated lipid bilayers. These thermodynamic and kinetic data were used to engineer stable nanoemulsions capable of undergoing at least ten complete phase-shift (condensation/vaporization) cycles with minimal loss in light transmission/extinction. In comparison to superheated liquid kinetic theory, droplet

vaporization occurred far below previously observed vapor nucleation flux thresholds indicating the presence of molecularly large thermal fluctuations in the optical extinction chamber.

References

[1] Mountford, P. A., Thomas, A. N., and Borden, M. A., 2015, "Thermal Activation of Superheated Lipid-Coated Perfluorocarbon Drops," Langmuir, **31**(16), pp. 4627–4634.

[2] Sheeran, P. S., Luois, S., Dayton, P. A., and Matsunaga, T. O., 2011, "Formulation and Acoustic Studies of a New Phase-Shift Agent for Diagnostic and Therapeutic Ultrasound," Langmuir, **27**(17), pp. 10412–10420.

[3] Sheeran, P. S., Luois, S. H., Mullin, L. B., Matsunaga, T. O., and Dayton, P. A., 2012, "Design of ultrasonically-activatable nanoparticles using low boiling point perfluorocarbons," Biomaterials, **33**(11), pp. 3262–3269.

[4] Dove, J. D., Mountford, P. A., Murray, T. W., and Borden, M. A., 2014, "Engineering optically triggered droplets for photoacoustic imaging and therapy," Biomed. Opt. Express, **5**(12), p. 4417.

[5] Marsh, D., 2013, Handbook of Lipid Bilayers, Second Edition, CRC Press.

[6] Feshitan, J. A., Chen, C. C., Kwan, J. J., and Borden, M. A., 2009, "Microbubble size isolation by differential centrifugation," J. Colloid Interface Sci., **329**(2), pp. 316–324.

[7] Mountford, P. A., Sirsi, S. R., and Borden, M. A., 2014, "Condensation Phase Diagrams for Lipid-Coated Perfluorobutane Microbubbles," Langmuir, **30**(21), pp. 6209–6218.

[8] Satinover, S. J., Dove, J. D., and Borden, M. A., 2014, "Single-Particle Optical Sizing of Microbubbles," Ultrasound Med. Biol., **40**(1), pp. 138–147.

[9] Epstein, P. S., and Plesset, M. S., 1950, "On the Stability of Gas Bubbles in Liquid-Gas Solutions," J. Chem. Phys., **18**(11), pp. 1505–1509.

[10] Duncan, P. B., and Needham, D., 2004, "Test of the Epstein−Plesset Model for Gas Microparticle Dissolution in Aqueous Media: Effect of Surface Tension and Gas Undersaturation in Solution," Langmuir, **20**(7), pp. 2567–2578.

[11] Kwan, J. J., 2012, "Theranostic Oxygen Delivery Using Ultrasound and Microbubbles," Theranostics, **2**(12), pp. 1174–1184.

[12] Baker, E. T., and Lavelle, J. W., 1984, "The effect of particle size on the light attenuation coefficient of natural suspensions," J. Geophys. Res. Oceans, **89**(C5), pp. 8197–8203.

[13] Israelachvili, J. N., 1992, Intermolecular and Surface Forces, Second Edition: With Applications to Colloidal and Biological Systems, Academic Press.

[14] Katiyar, A., Sarkar, K., and Jain, P., 2009, "Effects of encapsulation elasticity on the stability of an encapsulated microbubble," J. Colloid Interface Sci., **336**(2), pp. 519–525.

[15] Garg, S., Thomas, A. A., and Borden, M. A., 2013, "The effect of lipid monolayer in-plane rigidity on in vivo microbubble circulation persistence," Biomaterials, **34**(28), pp. 6862–6870.

[16] Borden, M. A., and Longo, M. L., 2004, "Oxygen Permeability of Fully Condensed Lipid Monolayers," J. Phys. Chem. B, **108**(19), pp. 6009–6016.

[17] Kim, D. H., Costello, M. J., Duncan, P. B., and Needham, D., 2003, "Mechanical Properties and Microstructure of Polycrystalline Phospholipid Monolayer Shells: Novel Solid Microparticles," Langmuir, **19**(20), pp. 8455–8466.

[18] Carey, V. P., 2007, Liquid Vapor Phase Change Phenomena: An Introduction to the Thermophysics of Vaporization and Condensation Processes in Heat Transfer Equipment, Second Edition, CRC Press, New York.

[19] Brown, J. A., and Mears, W. H., 1958, "Physical Properties of n-Perfluorobutane," J. Phys. Chem., **62**(8), pp. 960–962.

[20] Child, M. S., 2012, Molecular Collision Theory, Courier Dover Publications.

[21] Zhang, P., and Porter, T., 2010, "An in vitro Study of a Phase-Shift Nanoemulsion: A Potential Nucleation Agent for Bubble-Enhanced HIFU Tumor Ablation," Ultrasound Med. Biol., **36**(11), pp. 1856–1866.

[22] Eberhart, J. G., 1976, "The thermodynamic and the kinetic limits of superheat of a liquid," J. Colloid Interface Sci., **56**(2), pp. 262–269.

[23] Kwak, H.-Y., and Lee, S., 1991, "Homogeneous Bubble Nucleation Predicted by a Molecular Interaction Model," J. Heat Transf., **113**(3), pp. 714–721.

[24] Barnabé-Heider, M., Di Marco, M., Doane, P., Genest, M.-H., Gornea, R., Guénette, R., Leroy, C., Lessard, L., Martin, J.-P., Wichoski, U., Zacek, V., Clark, K., Krauss, C. B., Noble, A. J., Behnke, E., Feighery, W., Levine, I., Muthusi, C., Kanagalingam, S., and Noulty, R., 2005, "Response of superheated droplet detectors of the PICASSO dark matter search experiment," Nucl. Instrum. Methods Phys. Res. Sect. Accel. Spectrometers Detect. Assoc. Equip., **555**(1–2), pp. 184–204.

[25] Katz, J. L., and Blander, M., 1973, "Condensation and boiling: Corrections to homogeneous nucleation theory for nonideal gases," J. Colloid Interface Sci., **42**(3), pp. 496–502.

[26] Jarvis, T. J., Donohue, M. D., and Katz, J. L., 1975, "Bubble nucleation mechanisms of liquid droplets superheated in other liquids," J. Colloid Interface Sci., **50**(2), pp. 359–368.

[27] Rapoport, N., 2012, "Phase-shift, stimuli-responsive perfluorocarbon nanodroplets for drug delivery to cancer," Wiley Interdiscip. Rev. Nanomed. Nanobiotechnol., **4**(5), pp. 492–510.

Chapter 5

Nanodrops as Sonothermometry Probes

5.1 Introduction

The two previous chapters explored the condensation and thermal vaporization of fluorocarbon nanodrops. This section looks to apply that condensation and vaporization knowledge towards tailoring nanodrops to vaporize at specific temperatures through manipulation of the core material. The efficacy of fluorocarbon nanodrops as sonothermometry probes is reported in a manuscript currently under review in Langmuir titled *"Fluorocarbon Nanodrops as Acoustic Temperature Probes"* and is the basis of this chapter. Two fluorocarbons were mixed at different molar ratios to onset droplet vaporization at different temperatures between 37 and 74 °C under diagnostic ultrasound imaging.

5.2 Motivation

Temperature mapping of tissue is crucial for feedback control of advanced surgical hyperthermia procedures, such as high-intensity focused ultrasound (HIFU) and radiofrequency (RF)

ablation.[1–3] Ultrasound is portable and offers excellent spatial and temporal resolution;[4,5] it may therefore be advantageous over other *in vivo* thermal imaging methods, such as magnetic resonance imaging (MRI), which is expensive, often requires anesthesia owing to long scan times, and excludes patients with pace-makers and other metallic implants.[6–8] Measuring and mapping temperature with ultrasound imaging (sonothermetry) could remove the need for MRI guidance in ablation therapies, making them economically feasible and universally applicable. Conversely, monitoring brain temperature during therapeutic hypothermic neuroprotective procedures for traumatic brain injury, cardiac arrest and other maladies may insure that neurons are undamaged by overcooling.[9] Sonothermetry possibly could improve the mobility of cerebral cooling therapies, allowing them to be administered closer to the time of incident. However, diagnostic ultrasound currently lacks the ability noninvasively monitor temperature *in vivo* at tissue depth.

The speed of sound in tissue is a weak function of temperature over the ranges used in hypothermic and hyperthermic therapies, making it difficult to measure temperatures accurately based on tissue properties alone.[10] One approach to sonothermetry may therefore be to use a thermal probe that can emit or backscatter an acoustic signal detectable by diagnostic ultrasound. Microbubble ultrasound contrast agents are the most echogenic particles available;[11–14] they have been approved by the US FDA for echocardiography to aid in monitoring myocardial profusion,[15] but their acoustic response is also a weak function of temperature.

In principle, the formation of a microbubble in tissue upon crossing a predetermined temperature threshold (set point) would provide feedback in the form of sudden positive ultrasound contrast. Recently, phase-change nanodrops have been investigated as theranostic agents capable of vaporizing into microbubbles.[16–18] These droplets are formulated in the liquid state and, upon activation with ultrasound, vaporize into echogenic microbubbles in a process called

"acoustic droplet vaporization" (ADV).[19] The liquid-to-gas phase transition is an abrupt event,[20] making the phase-change droplet an ideal thermal probe. As an example, the current maximum clinical exposure of HIFU-mediated tissue ablation is 60 °C for 1 s.[21] Careful selection of nanodrop chemistry may provide ADV-enhanced ultrasound contrast when the maximum exposure limit of HIFU has been met.

Nanodrop emulsions are most commonly formed at standard temperature and pressure (STP) with liquid perfluoropentane (C_5F_{12}), which has a boiling temperature (T_b) of 28 °C.[22] The droplets are metastable *in vivo* at physiological temperature (37 °C), but require a relatively high acoustic intensity (mechanical index) for vaporization. Recently, Sheeran et al.[23–27] described a method to produce droplets of more volatile perfluorocarbons (PFCs), such as octafluoropropane (C_3F_8, T_b = -37 °C) and decafluorobutane (C_4F_{10}, T_b = -2 °C), which are metastable at STP and physiological temperature. These superheated droplets are formed through a microbubble-condensation technique, where phospholipid-coated microbubbles are pressurized and cooled to condense the gaseous core into a liquid. The droplets are metastable because vaporization is suppressed by the need for homogenous nucleation of a critical vapor embryo,[28,29] which shifts the threshold from the boiling temperature to the spinodal (~90% of the critical temperature, T_c). Experiments have shown that C_3F_8-nanodrops (T_c = 72 °C) spontaneously vaporize at ~40 °C (near physiological temperature), and C_4F_{10}-nanodrops (T_c = 113 °C) spontaneously vaporize at ~75 °C.[29]

However, ultrasound can activate vaporization of superheated droplets well below the spinodal through a superharmonic focusing effect.[30] Experiments at STP have shown, for example, that C_3F_8-nanodrops vaporize under 7.5-MHz ultrasound at a mechanical index of ~0.84 and C_4F_{10}-nanodrops vaporize at a mechanical index of ~1.28.[25] For sonothermetry, one must

decouple the effects of temperature and acoustic intensity. Ideally, one could develop a library of droplets that vaporize at different temperatures for a particular mechanical index.

Prior attempts have been made to mix PFCs for tuning droplet vaporization. Barnabe-Heider et al.[31] described mixed C_3F_8:C_4F_{10} emulsions for the detection of neutrinos and other subatomic particles. Kawabata et al.[32] mixed C_5F_{12} and 2H,3H-C_5F_{10} to lower the threshold intensity for ADV. Sheeran et al.[25] showed 1:1 C_3F_8:C_4F_{10} droplets experienced ADV at a threshold mechanical index ~1.17 at 7.5 MHz, which is closer to the value for pure C_4F_{10} than for pure C_3F_8. We hypothesize that this latter result may be explained by preferential dissolution of C_3F_8 out of the droplets, enriching them with C_4F_{10}.

The goal of the current study was to investigate the molecular thermodynamics of superheated phase-change emulsions to determine if composition can be tuned for sonothermetry at different temperature thresholds. First, we used a closed optical chamber to determine experimentally the spontaneous vaporization temperatures of mixed C_3F_8:C_4F_{10} nanodrops. Second, we used an ultrasound system with an open chamber to measure the effects of temperature and mechanical index on vaporization of pure-component and mixed C_3F_8:C_4F_{10} nanodrops; proof-of-concept was demonstrated for the acoustic thermal probe. Finally, we theoretically and experimentally assessed mixed C_3F_8:C_4F_{10} droplet stability in the open system, to mimic physiological conditions and assess the utility of mixed PFCs for turning ADV in biomedical applications.

5.3 Methods and Materials

5.3.1 Microbubble Synthesis

The nanodrops explored in this study were produced using the method of microbubble condensation as first reported by Sheeran et al.[23] and a lipid formulation optimized for stability.[29,33] Microbubbles for condensation were generated from a lipid suspension comprising 1,2-diarachidoyl-*sn*-glycero-3-phosphocholine (DAPC, $C_{20:0}$) (Avanti Polar Lipids, Alabaster, AL) and 1,2-disteroyl-*sn*-glycero-3-phosphoethanolamine-N-[methoxy(polyethylene glycol)-2000] (DSPE-PEG2000) (NOF America, White Plains, NY) at a molar ratio of 9:1. The lipid mixture was suspended in 100 mL of 0.2-µm cold-filtered 150 mM NaCl phosphate buffered saline (PBS) pH 7.4 (Sigma-Aldrich, St. Louis, MO) for a total lipid concentration of 2 mg mL^{-1}. The suspension was then stirred and heated to 10 °C above the main phase transition temperature of DAPC (T_m = 65 °C)[34] to promote lipid mixing. Microbubbles were formed by probe sonication and then size-isolated to 4-5 µm in diameter.[35] Microbubble size distributions and concentrations were confirmed using electrical impedance sensing with the MultiSizer 3 (Beckman Coulter, Brea, CA).[36]

Perfluorocarbon (PFC) gas mixtures were introduced to the gas-liquid interface during microbubble synthesis. C_3F_8 and C_4F_{10} (FluoroMed, Round Rock, TX) were mixed at molar ratios of 1:0, 3:1, 1:1, 1:3 and 0:1 using a gas proportioning rotameter (Omega, Stamford, CT) (Fig. 5.1A). The diluent also was equilibrated with the indicated gas mixture:[29,33] the PBS working fluid was degassed under a house vacuum for at least 8 h, re-gassed with the appropriate PFC mixture and allowed to equilibrate for at least 8 h at room temperature.

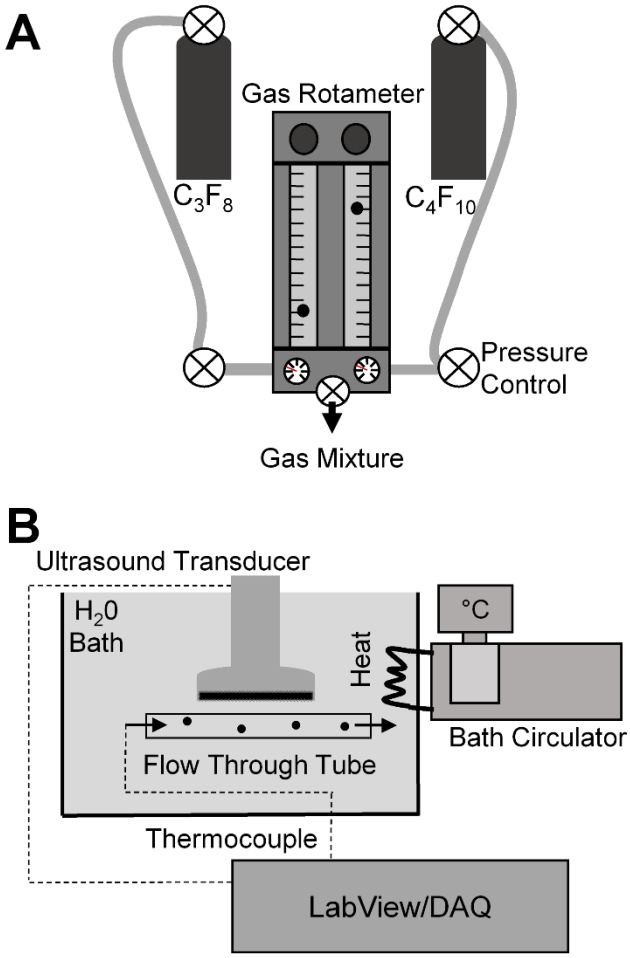

Figure 5.1. (A) Schematic of gas proportioning rotameter used to mix C_3F_8 and C_4F_{10} at specified molar ratios. **(B)** Experimental apparatus capable of providing diagnostic ultrasound images with simultaneous temperature data. Note that sample is held in a semi-permeable dialysis tube, and therefore the system is open to the atmosphere.

5.3.2 Optical Measurements in a Closed System

Transmitted light intensity was measured to follow the kinetics of condensation and vaporization in a closed system using our previously reported temperature- and pressure-controlled optical chamber (Fig. 4.1).[29] Microbubbles were injected into the chamber and condensed at a constant temperature of 25 °C, according to the following steps. First, the system was hydraulically primed with 20 mL of PFC-saturated PBS. 1 mL of the microbubble solution then was injected into the chamber at a concentration of 2 x 10^8 mL^{-1}. Successful microbubble delivery was confirmed

quantitatively through the measurement of light extinction: a decrease from ~90% to ~13% of the maximum voltage of the photodetector (Thor Labs, DET100A, Newton, NJ). The microbubbles were then converted to nanodrops by a step increase in pressure to 780 kPa. Microbubble condensation was confirmed optically by a return to ~90% max photodetector voltage.

In the first optical experiment, we measured the extent of vaporization following pressure release at a constant temperature. To accomplish this, the chamber was heated (0.5 °C s^{-1}) at constant pressure (780 kPa) to the indicated temperature. Five temperatures were examined for each nanodrop mixture: 30 to 50, 35 to 55, 45 to 65, 50 to 70 and 55 to 75 °C in 5 °C increments for C_3F_8:C_4F_{10} = 1:0, 3:1, 1:1, 1:3 and 0:1, respectively. Once the temperature equilibrated at the set point, the pressure was relieved rapidly back to atmospheric (83.8 kPa in Boulder, CO, USA), and the percentage of vaporized nanodrops was measured by light extinction according to the following equation:

$$P_{revap} = \frac{I_{\max} - I_{\min}}{I_{\max} - I_o} \tag{5.1}$$

where I_{max} was the maximum light-intensity achieved during condensation, I_{min} was the minimum light intensity achieved during vaporization and I_o was the initial light intensity when the microbubble solution was injected into the chamber. The probability-temperature data were then plotted and fit to a Gaussian cumulative distribution curve using Prism 5 (Graph Pad, La Jolla, CA), and this fit was used to determine the 50% vaporization temperature ($T_{50\%}$) for each mixed PFC nanodrop suspension.

In the second optical experiment, we measured the extent of vaporization during heating at constant (atmospheric) pressure. To accomplish this, the microbubbles were delivered to the chamber and condensed using the same steps as above. After condensation, however, pressure was immediately relieved back to atmospheric (83.8 kPa), and then the superheated nanodrop

suspension was heated at a rate of 0.5 °C s^{-1} until full vaporization was achieved, as indicated by minimum light transmission (~13%). The experimental vaporization temperature of each C_3F_8:C_4F_{10} nanodrop suspension was determined by applying a 3rd-order smoothing polynomial and 1st-order differentiation Savitzky-Golay filter in Matlab (Mathworks, Natick, MA) to the optical intensity-temperature curve. The filter outputted the inflection point of the light decay curve, which was deemed to be the spontaneous vaporization temperature (T_{VAP}) of the nanodrop suspension.

5.3.3 Ultrasound Measurements in an Open System

The microbubbles were converted to nanodrops prior to injection into the measurement system for the acoustic measurements. To accomplish this, 15 uL of size-selected (4-5 μm) bubbles were added to 300 μL of PFC-saturated PBS (the C_3F_8:C_4F_{10} ratio of the dissolved gas was matched to that of the microbubble core) in a 1 mL syringe to a final concentration of 2.5 x 10^8 mL^{-1}. The diluted microbubble suspension then was condensed as previously described by Dove et al.:[28] the 1 mL syringe was pressurized rapidly by hand until the suspension visibly changed from opaque to translucent.

Ultrasound studies of the nanodrop solutions undergoing acoustic vaporization were performed in a custom 9-L, temperature-controlled water bath (Fig. 1B). Temperature was monitored with a k-type thermistor (Omega, Stamford, CT) and controlled using an Isotemp 6200R20 heated circulating water bath (Fisher Sci., Waltham, MA). Ultrasound imaging was performed on an Acuson Sequoia C512 with an Acuson 15L8W transducer (Siemens, Malvern, PA) operating at a frequency of 8 MHz in cadence pulse sequencing (contrast) mode. Ultrasound images were captured from the scanner using an imaging converter (DFGUSB2pro, The Imaging Source, Charlotte, NC), and they were displayed and recorded with temperature measurements

using a custom LabView VI (National Instruments, Austin, TX). The ultrasound pulse intensity was set to the lowest available mechanical index (0.04), and the imaging system was used to align the sample tubing. A section of acoustically transparent 10-mm diameter (wet) cellulose dialysis tubing (Fisher Sci. 21-152-7, Pittsburg, PA) was positioned at the center of the ultrasound imaging field of view and oriented orthogonally to the transducer to capture the cross-section of the tube. The cellulose tubing allowed free exchange of solutes, including dissolved gases, between the nanodrop suspension and the water bath, which was open to the atmosphere.

In the first ultrasound imaging experiment, we determined the vaporization temperature for a constant pulse intensity (mechanical index) from the ultrasound imaging system. Once the water bath equilibrated to 25 °C, the scanner was turned on. Then, a 300-µL slug of superheated nanodrops was delivered from a syringe and through 25 cm of 10-mm diameter Tygon tubing coupled to the dialysis tubing. Once the center of the nanodrop slug was positioned in the dialysis tubing and in-plane with the transducer, the bath was heated at a rate of 0.5 °C min^{-1}. Vaporization of the nanodrops was captured as an increase in imaging contrast intensity from black to white pixels. The correlation between an increase in contrast video intensity and nanodrop vaporization was confirmed optically using a hand-held microscope (Dino-Lite AM-3011, Torrance, CA) with the ultrasound system operating at the maximum mechanical index (1.1) and 8 MHz. The log-compressed video intensity data (Siemens proprietary compression algorithm) from the stored images was integrated over a region of interest containing the dialysis tubing using ImageJ (NIH, Bethesda, MD). The video intensity-temperature data was plotted and put through a Savitzky-Golay filter for determining the inflection point of contrast enhancement. This inflection point was defined as the ultrasound-stimulated vaporization temperature (T_{US}) of the nanodrop solution (mechanical index = 0.04 at 8 MHz).

In the second ultrasound imaging experiment, we determined the threshold mechanical index for acoustic droplet vaporization at a constant temperature (37 and 60 °C). These temperatures represent normal physiological temperature and the highest temperature clinically allowed for high intensity focused ultrasound tissue ablation (60 °C for 1 s).[21] Mixed C_3F_8:C_4F_{10} nanodrop suspensions were injected into the dialysis tubing as described above and subjected to an ultrasound intensity ramp in which the intensity at the dialysis tubing was increased manually 30 dB, from a mechanical index of 0.04 to 1.1, at a rate of 1dB every 5 s. The relation between dB and mechanical index can be seen in Table 5.1. The ultrasound contrast intensity was analyzed as described above. Intensity was plotted as a function of mechanical index, and the inflection point was used to determine the temperature-dependent critical mechanical index for acoustic droplet vaporization.

MI	0.04	0.05	0.06	0.06	0.07	0.08	0.09	0.10	0.11
dB	-30.00	-29.00	-28.00	-27.00	-26.00	-25.00	-24.00	-23.00	-22.00
MI	0.13	0.14	0.16	0.18	0.20	0.22	0.25	0.28	0.31
dB	-21.00	-20.00	-19.00	-18.00	-17.00	-16.00	-15.00	-14.00	-13.00
MI	0.34	0.38	0.41	0.46	0.50	0.55	0.61	0.68	0.75
dB	-12.00	-11.00	-10.00	-9.00	-8.00	-7.00	-6.00	-5.00	-4.00
MI	0.83	0.92	1.00	1.10					
dB	-3.00	-2.00	-1.00	0.00					

Table 5.1. Relation between the mechanical index and power output (dB) for the diagnostic ultrasound machine at 8 MHz.

In the third ultrasound imaging experiment, we determined the mechanical index for vaporization at a constant temperature (37 °C) after allowing time for the nanodrop suspension to equilibrate through the wall of the dialysis tubing with the surrounding water bath. In this experiment, nanodrops comprising C_3F_8:C_4F_{10} ratios of 3:1, 1:1 and 0:1 were injected into the dialysis tubing as above and then allowed to equilibrate in the air-saturated water bath at 37 °C for 0, 5, 20, 60 and 300 s. The ultrasound images were recorded and analyzed as mentioned above.

5.3.4 Theoretical Dissolution of a Two-Component Nanodrop

Following the methodology of Epstein and Plesset,[37] we developed a dissolution model to explore the stability of a lipid-coated nanodrop comprising a mixture of C_3F_8 and C_4F_{10} in its core. The change in moles (n_i) of species *i* in the nanodrop core with respect to time is given by the flux (J_i) and an interfacial area (A):

$$-\frac{dn_i}{dt} = J_i A \tag{5.2}$$

For a spherical droplet, the interfacial area is:

$$A = 4\pi R^2 \tag{5.3}$$

where R is the droplet radius, and the mass flux is given by

$$J_i = k_i (C_{0i} - C_{\infty i}) \tag{5.4}$$

where k_i is the mass transfer coefficient for species *i*, and C_{0i} and $C_{\infty i}$ are the concentrations of species *i* in the aqueous phase at the droplet surface and in the bulk, respectively. The concentration boundary layer develops very quickly, and thus the mass transfer coefficient can be determined by a simple Sherwood number (Sh) correlation for pure diffusion from a sphere:

$$Sh_i = \frac{k_i R}{D_i} = 1 \tag{5.5}$$

where D_i is diffusivity. Concentration is related to mole fraction by:

$$C_i = \frac{x_i \rho_w}{M_w} \tag{5.6}$$

where ρ_w and M_w are the density and molecular weight of water. If we assume ideal solution conditions and local equilibrium at the droplet surface, then Raoult's law for the fluorocarbon core can be connected to Henry's law for the aqueous medium to relate the mole fraction of species *i* in the nanodrop (y_i) to the solubility in the aqueous phase (x_i):[38]

$$y_i P_i = H_i x_i \tag{5.7}$$

where P_i is the vapor pressure of pure component i and H_i is Henry's constant. The pure component vapor pressure is determined from Kelvin's equation:[39]

$$P_i = P_{i,sat} e^{\frac{2M_i\sigma}{BT\rho_i R}} \tag{5.8}$$

where $P_{i,sat}$ is saturation pressure, M_i is molecular weight, σ is surface tension, B is the ideal gas constant, T is absolute temperature and ρ_i is mass density. Combining (5.6) to (5.8) and rearranging gives the surface concentration:

$$C_{0i} = \frac{y_i \rho_w P_{i,sat}}{M_w H_i} e^{\frac{2M_i\sigma}{BT\rho_i R}}$$

(5.9)

Taking the limit as R goes to infinity gives the concentration in the bulk solution ($C_{\infty i}$):

$$C_{\infty i} = \frac{y_{\infty i} \rho_w P_{i,sat}}{M_w H_x} \tag{5.10}$$

where $y_{\infty i}$ is the corresponding mole fraction of species i in the aqueous phase far away from the droplet. Combining equations (5.9) and (5.10) with (5.2) through (5.4) yields an expression for the molar rate of change of species i in the droplet core:

$$-\frac{dn_i}{dt} = \frac{4\pi R \rho_w P_{i,sat}}{M_w H_i}\left[y_i e^{\frac{2M_i\sigma}{BT\rho_i R}} - y_{\infty i} \right] \tag{5.11}$$

The concentration of species i in the medium can vary from zero to saturation, and we therefore define the following relation:

$$y_{\infty i} = y_i \cdot f_i \tag{5.12}$$

where f_i is the ratio of species i in the bulk medium, ranging from 0 to 1. The two species are denoted as $i = 1$ for C_3F_8 and $i = 2$ for C_4F_{10}. The molar fractions of C_3F_8 and C_4F_{10} are therefore given as follows:

$$y_1 = \frac{n_1}{n_1 + n_2} \tag{5.13a}$$

$$y_2 = \frac{n_2}{n_1 + n_2} \tag{5.13b}$$

with n_1 and n_2 being the moles of C_3F_8 and C_4F_{10} in droplet, respectively. The instantaneous droplet radius is therefore given as:

$$R(t) = \left(\frac{3}{4\pi} \left(\frac{n_1(t)M_1}{\rho_1} + \frac{n_2(t)M_2}{\rho_2} \right) \right)^{\frac{1}{3}} \tag{5.14}$$

and is found by solving the system of ordinary differential equations:

$$-\frac{dn_1}{dt} = \frac{n_1}{n_1 + n_2} \frac{4\pi R \rho_w P_{1,sat}}{M_w H_1} \left[e^{\frac{2M_1\sigma}{BT\rho_1 R}} - f_1 \right] \tag{5.15a}$$

$$-\frac{dn_2}{dt} = \frac{n_2}{n_1 + n_2} \frac{4\pi R \rho_w P_{2,sat}}{M_w H_2} \left[e^{\frac{2M_2\sigma}{BT\rho_2 R}} - f_2 \right] \tag{5.15b}$$

with initial conditions given by the initial radius and composition of the droplet and bulk phase.

5.4 Results and Discussion

5.4.1 Spontaneous vaporization in a Closed System

Figure 5.2A presents the vaporization probability as a function of temperature for each of the mixed C_3F_8:C_4F_{10} nanodrop suspensions from the isothermal pressure-release experiment. As C_4F_{10} content increased, spontaneous vaporization shifted to higher temperatures. This data was

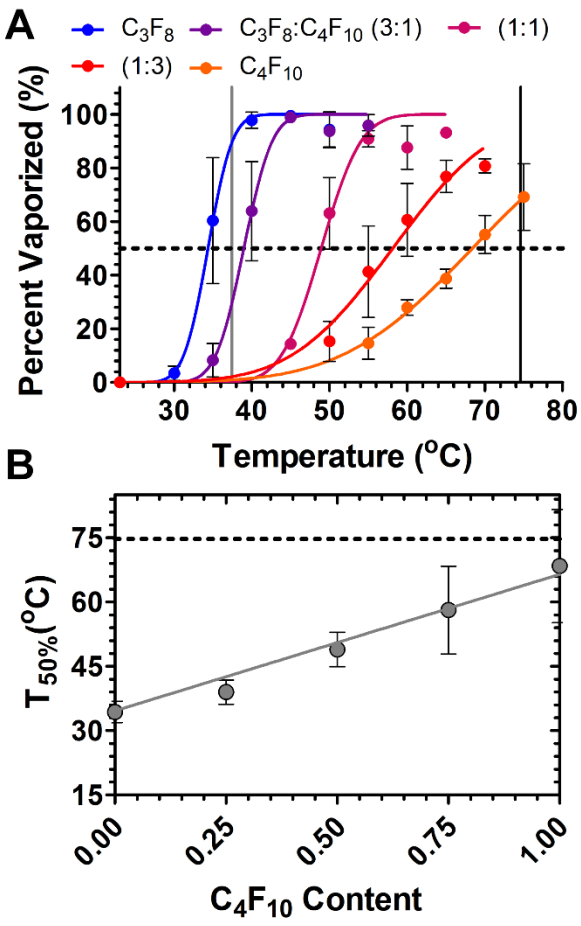

Figure 5.2. **(A)** Probability of vaporization versus temperature for DAPC:DSPE-PEG2000 (9:1) coated, C_3F_8:C_4F_{10} [1:0 (blue), 3:1 (violet), 1:1 (magenta), 1:3 (red) and 0:1 (orange)] core nanodrops (n=3). Colored lines are Gaussian cumulative distribution curve fits to data. Dashed line represents the 50% vaporization threshold used to determine $T_{50\%}$ for each composition. Solid vertical lines identify theoretical spinodal decomposition temperatures (90% of the critical temperature) for C_3F_8 (gray) and C_4F_{10} (black). **(B)** The $T_{50\%}$ values plotted against the mole fraction of C_4F_{10} in the droplet core. Solid gray line represents the linear regression of the data and the horizontal dashed black line indicates 90% of the critical temperature of C_4F_{10}.

used to determine the temperature required for 50% spontaneous vaporization ($T_{50\%}$). Figure 5.2B shows that $T_{50\%}$ increased linearly with C_4F_{10} mole fraction, providing a convenient and predictable range of vaporization thresholds that could be tuned by the C_3F_8:C_4F_{10} ratio. This is likely because the closed system remains near saturation (f = 1) as the temperature is changed.

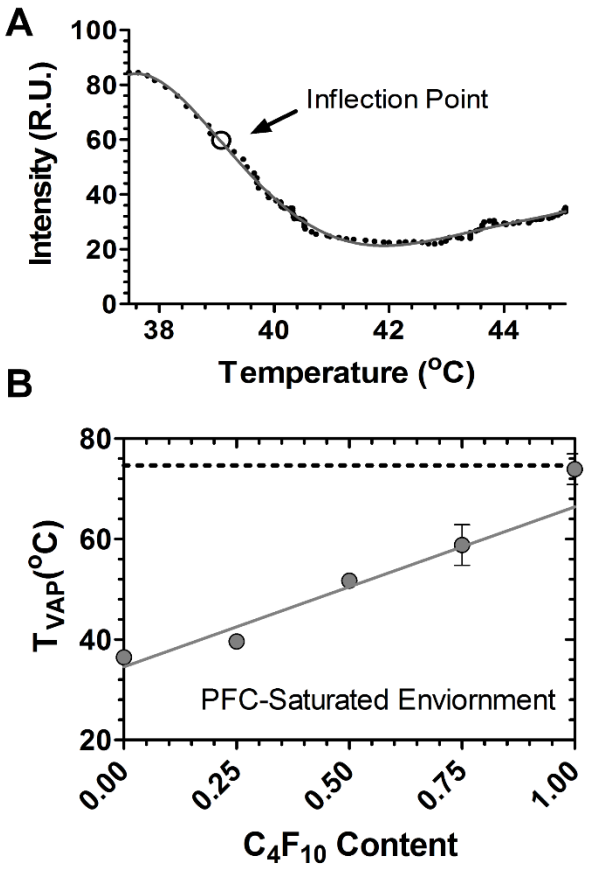

Figure 5.3. (A) A typical temperature-intensity curve for a DAPC:DSPE-PEG2000 (9:1) coated, C_3F_8:C_4F_{10} (3:1) filled nanodrop solution undergoing slow heating (0.5 °C s^{-1}) heating. Gray solid line is a 3rd-order polynomial fit of the data. The black circle indicates the inflection point (39.1 °C), which we define here as the vaporization temperature (T_{VAP}). **(B)** The T_{VAP} values plotted against the mole fraction of C_4F_{10} in the droplet core (n=3). Solid gray line is the linear regression of $T_{50\%}$ curve in Fig. 2b. Dashed black line indicates 90% of the critical temperature of C_4F_{10}.

One interesting observation was that the suspensions could not achieve 100% vaporization when heated above 65 °C. This temperature corresponded to the main phase transition temperature of the primary lipid species (DAPC) of the nanodrop shell. It has been previously established that microbubbles and nanodrops are unstable when their lipid shell is at or near the fluid state.[29,33] Rapid microbubble dissolution therefore is responsible for the inability of these nanodrop suspensions to reach complete vaporization. Dissolution, predominately determined here by the

lipid intermolecular forces, thus gives an upper limit on the allowable temperature range for sonothermetry by ADV.

Figure 5.3A shows the transmitted light intensity curve for a typical C_3F_8:C_4F_{10} (3:1) nanodrop suspension undergoing heating (0.5 °C s^{-1}) at constant atmospheric pressure (~84 kPa). The intensity began to decrease near 38 °C, with a maximum slope at 39.1 °C. The maximum slope (inflection point) indicates the point at which the nanodrop suspension vaporizes completely to a microbubble suspension, and thus defines the spontaneous vaporization temperature (T_{VAP}).

Figure 5.3B shows the spontaneous vaporization temperatures for each mixed C_3F_8:C_4F_{10} nanodrop suspension. Note that the T_{VAP} points fall on the line fitted to the $T_{50\%}$ values on Figure 5.2B. Thus, this nanodrop system shows excellent agreement in the spontaneous vaporization temperature, regardless of whether the emulsion was depressurized at constant temperature, or heated at constant pressure, to get to that point. One can therefore conclude that mixing C_3F_8 and C_4F_{10} in the droplet core is an effective method for tuning thermal vaporization in a closed, saturated environment.

5.4.2 Acoustic Vaporization in an Open System

For the fluorocarbon nanodrops to succeed as effective acoustic temperature probes, however, they must be imaged by ultrasound in a system open to the atmosphere (e.g., as happens *in vivo* in alveolar blood capillaries). Figure 5.4A shows a typical plot of the integrated ultrasound contrast video intensity as a function of temperature for a region of interest around the cross section of the dialysis tubing. The image to the left shows the droplets at 33 °C, before vaporization. The image on the right shows vaporized microbubbles at 38.3 °C (see video in Supporting Information). As with the optical intensity data, the inflection point of the ultrasound contrast enhancement signal was defined as the acoustic vaporization temperature (T_{US}).

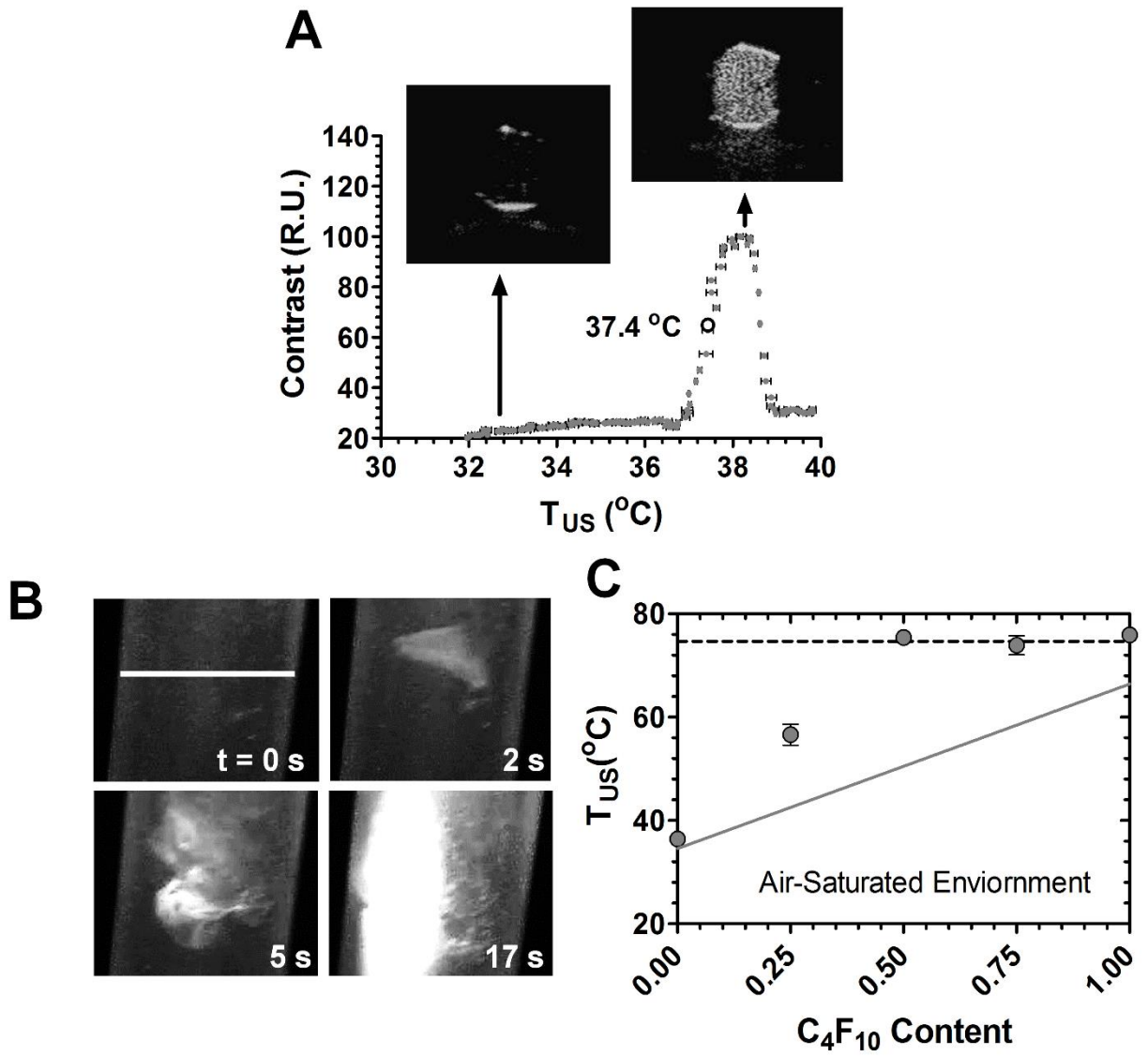

Figure 5.4. (A) A typical ultrasound contrast video intensity (mechanical index = 0.04 at 8 MHz) versus temperature curve for a DAPC:DSPE-PEG2000 (9:1) coated, C_3F_8 core nanodrop suspension. Black circle is the inflection point of the ultrasound intensity and indicates the acoustic vaporization temperature (T_{US}) of the nanodrop solution for this open system. Also shown are representative ultrasound images at the indicated temperatures. Note that the video intensity data is log-compressed with a proprietary algorithm by the ultrasound scanner prior to export and analysis of the video images. **(B)** Confirmation of nanodrop vaporization with a hand-held microscopy camera; these are C_4F_{10}-core droplets activated by ultrasound mechanical index of 1.1 at 8 MHz and 37 °C. A video of this image sequence can be seen in supporting information. Scale bar represents 10 mm. **(C)** The T_{US} values plotted against the mole fraction of C_4F_{10} in the droplet core (n=3). Solid gray line is the linear regression of $T_{50\%}$ curve in Fig. 2b. Dashed black line indicates 90% of the critical temperature of C_4F_{10}.

Confirmation of vaporization was provided by microscopy images (Fig. 5.4B). Here, some

C_4F_{10} droplets were seen to vaporize as they entered the ultrasound field of view (mechanical index = 1.1 at 8 MHz). Initially (t = 0 s), there were no droplets in the ultrasound field. As flow continued, the nanodrop suspension entered the ultrasound field of view, and the formation of bubbles was confirmed by a change of the liquid turning translucent (dark) to opaque (bright). Some interesting flow dynamics were visualized as vaporization proceeded (see video in Supporting Information).

Figure 5.4C shows the T_{US} values plotted versus C_4F_{10} mole fraction, with the line obtained from the $T_{50\%}$ data obtained above. The acoustic vaporization temperatures were close to the spontaneous vaporization temperatures for pure C_3F_8 and C_4F_{10}, but deviated significantly for each of the three mixtures. For example, the 3:1 (C_3F_8:C_4F_{10}) mixture acoustically vaporized near the spontaneous vaporization temperature for 1:3 mixture; the 1:1 and 1:3 mixtures acoustically vaporized at the pure C_4F_{10} acoustic vaporization temperature. This result strongly indicated that the ratio of C_3F_8:C_4F_{10} had decreased in this open system.

5.4.3 Effect of Temperature on Threshold Mechanical Index

Figure 5.5A shows a typical plot of the ultrasound contrast enhancement versus mechanical index for pure C_4F_{10} droplets at 60 °C. The inflection point was defined as the threshold mechanical index for acoustic droplet vaporization (~0.38 for this suspension). Figure 5.5B shows the threshold mechanical indices plotted as a function of C_4F_{10} mole fraction at 37 and 60 °C. All PFC mixtures vaporized at lower mechanical indices at 60 °C when compared to 37 °C. This result was expected because, as the droplets get closer to their spontaneous vaporization temperature, less additional acoustic energy (lower peak negative pressure in the region of superharmonic focusing) is required to nucleate a critical vapor embryo.

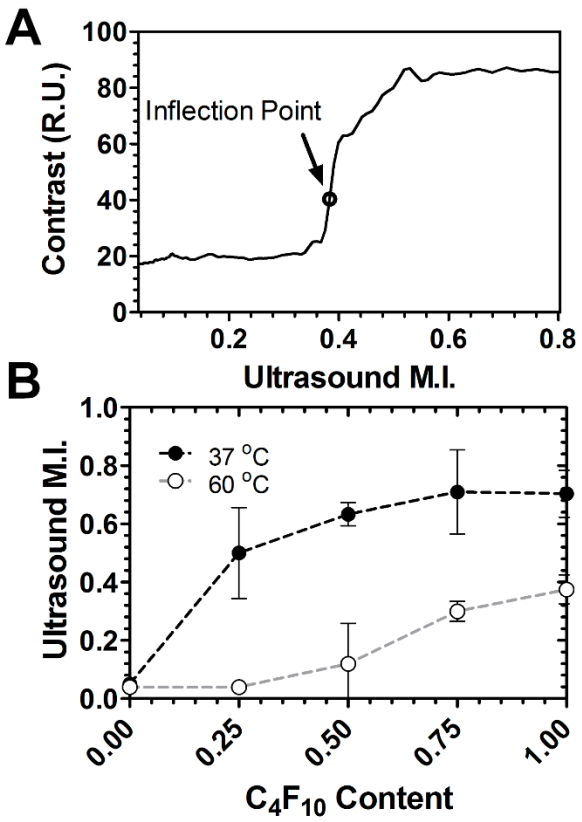

Figure 5.5. (A) A typical ultrasound contrast video intensity (8 MHz) versus mechanical index curve for a DAPC:DSPE-PEG2000 (9:1) coated, C_4F_4 core nanodrop solution at 60 °C. Black circle is the inflection point (mechanical index = 0.39) of the ultrasound intensity and indicates the acoustic mechanical index vaporization threshold for this open system. **(B)** The threshold mechanical index values plotted versus C_4F_{10} mole fraction at 37 °C (black) and 60 °C (gray) (n=3).

The droplets injected at 37 °C show a nonlinear relationship with respect to C_4F_{10} content, which again indicates a decaying amount of C_3F_8 in the droplet for this open system. Sheeran et al.[25] measured the mechanical indices for acoustic vaporization for pure 1-µm diameter C_3F_8 and C_4F_{10} droplets at 37 °C to be ~0.18 and 0.73, respectively, at 7.5 MHz, which is consistent with our results of 0.04 for pure C_3F_8 and 0.7 for pure C_4F_{10}. The greater values observed by Sheeran et al. may be explained by the higher atmospheric pressure in Chapel Hill, NC (~100 kPa) compared to that in Boulder, CO (~84 kPa), which would inhibit vaporization. Additionally, it

was observed that 1:0, 3:1 and 1:1 (C_3F_8:C_4F_{10}) droplets injected at 60 °C required a very low mechanical index for acoustic droplet vaporization.

Figure 5.6 shows representative ultrasound images of pure C_3F_8 and C_4F_{10} droplets at 37 and 60 °C and mechanical index of 0.38 at 8 MHz. This figure demonstrates proof-of-concept for

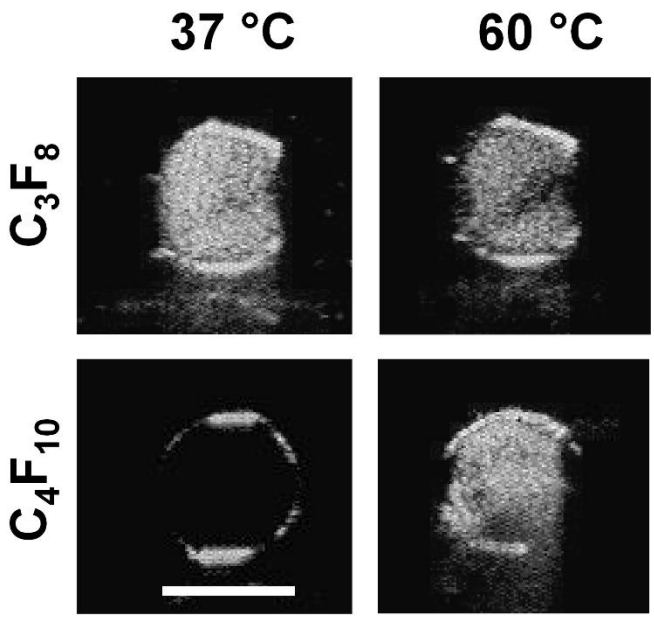

Figure 5.6. Demonstration of sonothermometry: C_4F_{10} core nanodrops vaporized at 60 °C, but not 37 °C, at a mechanical index of 0.38. All images were constructed by compiling the maximum signal over 5 frames (5 s). Scale bar represents 10 mm.

a thermal acoustic probe. Pure C_4F_{10} droplets were stable against spontaneous vaporization at both temperatures, whereas pure C_3F_8 droplets spontaneously vaporized near physiological temperature. Additionally, pure C_4F_{10} droplets were stable against acoustic droplet vaporization at 37 °C, but not at 60 °C. This result shows that the C_4F_{10} droplets can indicate a temperature threshold relevant to hyperthermia therapy in an open system using a clinical ultrasound scanner.

5.4.4 Stability of Mixed PFC Droplets Exposed to the Atmosphere

Figure 5.7A shows the effect of exposure time on the threshold mechanical index for acoustic droplet vaporization for two C_3F_8:C_4F_{10} mixtures and pure C_4F_{10}. The threshold mechanical index

increased for the two mixtures, but not C_4F_{10}, indicating that C_3F_8 is being depleted from the droplet core. The largest jump for the two mixtures appears to happen between 60 and 300 s, which is consistent with the theoretical predictions discussed below. We also note that the pure C_3F_8 and 1:1 mixed droplets produced by Sheeran et al.[25] showed an abrupt decrease in droplet count within the first 10 min, indicating that C_3F_8 dissolves faster than C_4F_{10}.

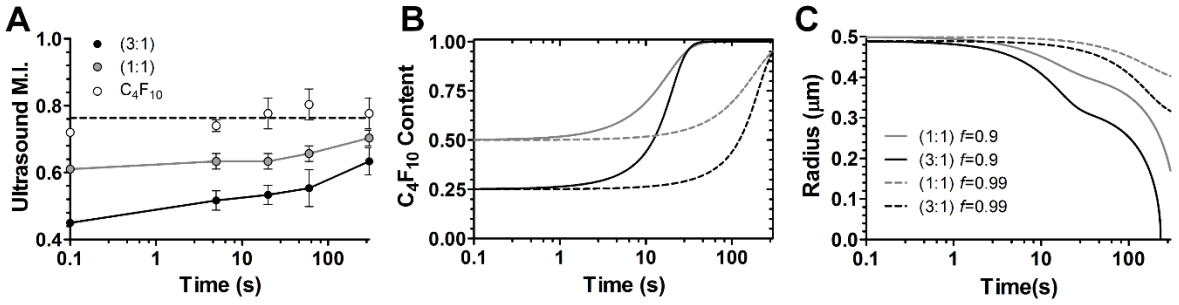

Figure 5.7. (A) Threshold mechanical index for vaporization at 8 MHz as a function of exposure time in the open system, for DAPC:DSPE-PEG2000 (9:1) coated PFC-filled (C_3F_8:C_4F_{10} at molar ratios of 3:1 (black), 1:1 (gray) and 0:1 (white)) (n=3). **(B)** The theoretical change in C_4F_{10} content over time for mixed PFC-core nanodrops. **(C)** The corresponding theoretical change in droplet radius. Shown are predictions for C_3F_8:C_4F_{10} = 3:1 (black) and 1:1 (gray). For the simulations, the amount of dissolved PFCs in the surrounding medium was set to f = 0.90 (solid) and 0.99 (dashed). Model parameters: D_1=7.33x10^{-10} m^{2}s^{-1}, D_2=4.94x10^{-10} m^{2}s^{-1}, $P_{i,sat}$=265 kPa, ρ_w=1000 kg m^{-3}, M_1=188.02 g mol^{-1}, M_2=238.03 g mol^{-1}, ρ_1=1601 kg m^{-3}, ρ_2=1594 kg m^{-3}, H_1=6.7x10^{-5} g m^{-3} Pa^{-1}, H_2=3.5x10^{-6} g m^{-3} Pa^{-1}, M_w=18.02 g mol^{-1}, γ=0.012 N m^{-1}, R_o=500 nm and T = 310 K.

We next modeled the dissolution behavior of two-component droplets suspended in an air-saturated medium. Figure 5.7B shows the theoretical percentage of C_4F_{10} in the droplet core versus time for both the 3:1 and 1:1 mixtures being suspended in 90 and 99% PFC-saturated PBS media. Both droplets become depleted of C_3F_8 over 20 s at 90% saturation, and over 120 s for 99% saturation. Figure 5.7C shows the corresponding change in overall droplet size. Although both droplets survive for an extended period of time (past 100 s), the C_3F_8:C_4F_{10} ratio changes quickly. These results confirm our experimental results, as well as those of Sheeran et al.,[25] and show that PFC mixtures may be unsuitable as phase-change agents for sonothermetry. However, pure

C_4F_{10} appears to be an excellent candidate for development of an acoustic thermal probe relevant to therapeutic hyperthermia.

5.5 Conclusions

This study demonstrated proof-of-concept for the use of superheated nanodrops created by condensation of lipid-coated microbubbles as acoustic thermal probes over a temperature range relevant to therapeutic hyperthermia. Additionally, experiments with C_3F_8:C_4F_{10} mixtures in a closed chamber confirmed that the vaporization temperature is governed by molecular thermodynamics of the fluorocarbons, and that microbubble stability is governed by intermolecular forces between the phospholipids. However, experiments and modeling of the nanoemulsions in an open system revealed that the tunability of vaporization by either temperature or ultrasound mechanical index is limited in C_3F_8:C_4F_{10} mixtures owing to rapid depletion of the more soluble C_3F_8 species. Overall, these results demonstrate the potential utility and limitations of superheated fluorocarbon emulsions for sonothermetry.

References

[1] S, M., C, K., N, S., M, S., L, V., and M, M., 1992, "Tissue ablation in benign prostatic hyperplasia with high-intensity focused ultrasound.," Eur. Urol., **23 Suppl 1**, pp. 39–43.

[2] Nahum Goldberg, S., Scott Gazelle, G., Dawson, S. L., Rittman, W. J., Mueller, P. R., and Rosenthal, D. I., 1995, "Tissue ablation with radiofrequency: Effect of probe size, gauge, duration, and temperature on lesion volume," Acad. Radiol., **2**(5), pp. 399–404.

[3] Brace, C. L., 2010, "Microwave Tissue Ablation: Biophysics, Technology, and Applications," Crit. Rev. Biomed. Eng., **38**(1), pp. 65–78.

[4] Fenster, A., and Downey, D. B., 1996, "3-D ultrasound imaging: a review," IEEE Eng. Med. Biol. Mag., **15**(6), pp. 41–51.

[5] Hides, J. A., Richardson, C. A., and Jull, G. A., 1998, "Use of real-time ultrasound imaging for feedback in rehabilitation," Man. Ther., **3**(3), pp. 125–131.

[6] Bertsch, F., Mattner, J., Stehling, M. K., M̈uller-Lisse, U., Peller, M., Loeffler, R., Weber, J. ̈urgen, Meßmer, K., Wilmanns, W., Issels, R., and Reiser, M., 1998, "Non-invasive temperature mapping using MRI: comparison of two methods based on chemical shift and T1-relaxation," Magn. Reson. Imaging, **16**(4), pp. 393–403.

[7] Cline, H. E., Hynynen, K., Hardy, C. J., Watkins, R. D., Schenck, J. F., and Jolesz, F. A., 1994, "MR temperature mapping of focused ultrasound surgery," Magn. Reson. Med., **31**(6), pp. 628–636.

[8] Samset, E., 2006, "Temperature mapping of thermal ablation using MRI," Minim. Invasive Ther. Allied Technol., **15**(1), pp. 36–41.

[9] Cilio, M. R., and Ferriero, D. M., 2010, "Synergistic neuroprotective therapies with hypothermia," Semin. Fetal. Neonatal Med., **15**(5), pp. 293–298.

[10] Ophir, J., 1986, "Estimation of the Speed of Ultrasound Propagation in Biological Tissues: A Beam-Tracking Method," IEEE Trans. Ultrason. Ferroelectr. Freq. Control, **33**(4), pp. 359–368.

[11] Ferrara, K., Pollard, R., and Borden, M., 2007, "Ultrasound microbubble contrast agents: fundamentals and application to gene and drug delivery," Annu. Rev. Biomed. Eng., **9**, pp. 415–447.

[12] Goldberg, B. B., Liu, J.-B., and Forsberg, F., 1994, "Ultrasound contrast agents: A review," Ultrasound Med. Biol., **20**(4), pp. 319–333.

[13] Stride, E., and Saffari, N., 2003, "Microbubble ultrasound contrast agents: A review," Proc. Inst. Mech. Eng. [H], **217**(6), pp. 429–447.

[14] Balen, F. G., Allen, C. M., and Lees, W. R., 1994, "Ultrasound contrast agents," Clin. Radiol., **49**(2), pp. 77–82.

[15] Li, P., Armstrong, W. F., and Miller, D. L., 2004, "Impact of myocardial contrast echocardiography on vascular permeability: comparison of three different contrast agents," Ultrasound Med. Biol., **30**(1), pp. 83–91.

[16] Sirsi, S. R., and Borden, M. A., 2014, "State-of-the-art materials for ultrasound-triggered drug delivery," Adv. Drug Deliv. Rev., **72**, pp. 3–14.

[17] Zhang, P., and Porter, T., 2010, "An in vitro study of a phase-shift nanoemulsion: A potential nucleation agent for bubble-enhanced HIFU tumor ablation," Ultrasound Med Biol, **36**(11), pp. 1856–1866.

[18] Husseini, G. A., Pitt, W. G., and Martins, A. M., 2014, "Ultrasonically triggered drug delivery: Breaking the barrier," Colloids Surf. B Biointerfaces, **123**, pp. 364–386.

[19] Kripfgans, O. D., Fowlkes, J. B., Miller, D. L., Eldevik, O. P., and Carson, P. L., 2000, "Acoustic droplet vaporization for therapeutic and diagnostic applications," Ultrasound Med. Biol., **26**(7), pp. 1177–1189.

[20] Sheeran, P. S., Matsunaga, T. O., and Dayton, P. A., 2014, "Phase change events of volatile liquid perfluorocarbon contrast agents produce unique acoustic signatures," Phys. Med. Biol., **59**(2), pp. 379–401.

[21] Zhou, Y.-F., 2011, "High intensity focused ultrasound in clinical tumor ablation," World J. Clin. Oncol., **2**(1), pp. 8–27.

[22] Williams, R., Wright, C., Cherin, E., Reznik, N., Lee, M., Gorelikov, I., Foster, F. S., Matsuura, N., and Burns, P. N., 2013, "Characterization of Submicron Phase-change Perfluorocarbon Droplets for Extravascular Ultrasound Imaging of Cancer," Ultrasound Med. Biol., **39**(3), pp. 475–489.

[23] Sheeran, P. S., Luois, S., Dayton, P. A., and Matsunaga, T. O., 2011, "Formulation and Acoustic Studies of a New Phase-Shift Agent for Diagnostic and Therapeutic Ultrasound," Langmuir, **27**(17), pp. 10412–10420.

[24] Sheeran, P. S., Wong, V. P., Luois, S., McFarland, R. J., Ross, W. D., Feingold, S., Matsunaga, T. O., and Dayton, P. A., 2011, "Decafluorobutane as a phase-change contrast agent for low-energy extravascular ultrasonic imaging," Ultrasound Med. Biol., **37**(9), pp. 1518–1530.

[25] Sheeran, P. S., Luois, S. H., Mullin, L. B., Matsunaga, T. O., and Dayton, P. A., 2012, "Design of ultrasonically-activatable nanoparticles using low boiling point perfluorocarbons," Biomaterials, **33**(11), pp. 3262–3269.

[26] Matsunaga, T. O., Sheeran, P. S., Luois, S., Streeter, J. E., Mullin, L. B., Banerjee, B., and Dayton, P. A., 2012, "Phase-change nanoparticles using highly volatile perfluorocarbons: toward a platform for extravascular ultrasound imaging," Theranostics, **2**(12), pp. 1185–1198.

[27] Sheeran, P. S., Matsunaga, T. O., and Dayton, P. A., 2013, "Phase-transition thresholds and vaporization phenomena for ultrasound phase-change nanoemulsions assessed via high-speed optical microscopy," Phys. Med. Biol., **58**(13), pp. 4513–4534.

[28] Dove, J. D., Mountford, P. A., Murray, T. W., and Borden, M. A., 2014, "Engineering optically triggered droplets for photoacoustic imaging and therapy," Biomed. Opt. Express, **5**(12), p. 4417.

[29] Mountford, P. A., Thomas, A. N., and Borden, M. A., 2015, "Thermal Activation of Superheated Lipid-Coated Perfluorocarbon Drops," Langmuir, **31**(16), pp. 4627–4634.

[30] Shpak, O., Verweij, M., Vos, H. J., Jong, N. de, Lohse, D., and Versluis, M., 2014, "Acoustic droplet vaporization is initiated by superharmonic focusing," Proc. Natl. Acad. Sci., **111**(5), pp. 1697–1702.

[31] Barnabé-Heider, M., Di Marco, M., Doane, P., Genest, M.-H., Gornea, R., Guénette, R., Leroy, C., Lessard, L., Martin, J.-P., Wichoski, U., Zacek, V., Clark, K., Krauss, C. B., Noble, A. J., Behnke, E., Feighery, W., Levine, I., Muthusi, C., Kanagalingam, S., and Noulty, R., 2005, "Response of superheated droplet detectors of the PICASSO dark matter search experiment," Nucl. Instrum. Methods Phys. Res. Sect. Accel. Spectrometers Detect. Assoc. Equip., **555**(1–2), pp. 184–204.

[32] Kawabata, K., Sugita, N., Yoshikawa, H., Azuma, T., and Umemura, S., 2005, "Nanoparticles with Multiple Perfluorocarbons for Controllable Ultrasonically Induced Phase Shifting," Jpn. J. Appl. Phys., **44**, pp. 4548–4552.

[33] Mountford, P. A., Sirsi, S. R., and Borden, M. A., 2014, "Condensation Phase Diagrams for Lipid-Coated Perfluorobutane Microbubbles," Langmuir, **30**(21), pp. 6209–6218.

[34] Marsh, D., 2013, Handbook of Lipid Bilayers, Second Edition, CRC Press.

[35] Feshitan, J. A., Chen, C. C., Kwan, J. J., and Borden, M. A., 2009, "Microbubble size isolation by differential centrifugation," J. Colloid Interface Sci., **329**(2), pp. 316–324.

[36] Satinover, S. J., Dove, J. D., and Borden, M. A., 2014, "Single-Particle Optical Sizing of Microbubbles," Ultrasound Med. Biol., **40**(1), pp. 138–147.

[37] Su, J. T., and Needham, D., 2013, "Mass Transfer in the Dissolution of a Multicomponent Liquid Droplet in an Immiscible Liquid Environment," Langmuir, **29**(44), pp. 13339–13345.

[38] Prausnitz, J. M., Lichtenthaler, R. N., and Azevedo, E. G. de, 1998, Molecular Thermodynamics of Fluid-Phase Equilibria, Prentice Hall, Upper Saddle River, N.J.

[39] Skinner, L. M., and Sambles, J. R., 1972, "The Kelvin equation—a review," J. Aerosol Sci., **3**(3), pp. 199–210.

Chapter 6

Conclusions

6.1 Summary of Thesis and Contributions

Microbubble condensed superheated lipid-coated fluorocarbon nanoemulsions are metastable in the liquid state when subjected to temperatures near the physiological and higher. They are capable of vaporizing back into the gaseous state with externally applied acoustic, optical or thermal energy. Little was known about their condensation and vaporization behavior. This thesis improved the understanding of microbubble condensation and nanodroplet vaporization and will progress current diagnostic and therapeutic medical applications.

In Chapter 2, classical thermodynamics was used to introduce traditional liquid-gas phase change theories. Intermolecular interactions of a gas and liquid were briefly introduced with the Lennard-Jones potential, which depicted the balance of molecular energy and attraction forces. The van der Waals equation of state was used to construct a classical thermodynamic saturation curve, which requires phase transition when the chemical potential of the liquid phase equals that of the gas and forbids the simultaneous existence of both phases. The Laplace pressure of a lipid-

coated microbubble was applied to the bulk saturation curve and predicted a decrease in hydrostatic pressure required for microbubble condensation. The Antoine vapor equation was used in combination with the Laplace pressure to determine the superheat stability of microbubble condensed emulsions. It was determined that the Laplace pressure alone could not account for recently observed condensed emulsion superheat stabilities.

The homogeneous and heterogeneous nucleation of water vapor was briefly reviewed to provide an understanding of the molecular origin of condensation. Macroscopic condensation and vaporization through homogeneous nucleation required great supersaturation pressures and superheat temperatures, respectively, because of the energy barrier associated with forming nucleates of sufficient size for phase transition. The microbubble core was assumed to be a pure gas, free of particulates and imperfections capable of causing premature heterogeneous nucleation. The energy required to form a sufficient liquid embryo for condensation was equivalent to the Gibbs energy, the energies required to liquefy the embryo and expand its interfacial surface area. The molecular kinetics of forming condensation capable liquid embryos was reviewed to account for the probability of overcoming the Gibbs energy barrier for a continuously nucleating dual-phase supersaturated gas. Predicted nucleation rates were compared to literature to construct a supersaturated microbubble condensation curve. Having accounted for the Laplace pressure in the core, microbubble condensation due to homogeneous nucleation was predicted to occur at ~150% of the bulk saturation pressure.

Similarly, the thermal vaporization of a microbubble condensed droplet core was treated as a superheated liquid undergoing homogeneous nucleation of the vapor phase. The Gibbs free energy barrier for equilibrium vapor embryo formation was quantified along with nucleate formation rates for a lipid-coated condensed fluorocarbon nanodrop. Comparison of predicted

critical nucleation flux rates to previous literature provided droplet vaporization temperatures near 90% of the fluorocarbons critical temperature at relatively low reduced pressures. Condensation and vaporization predictions suggested the simultaneous stability of the gas and liquid phase over significant pressure and temperature ranges.

Chapter 3 presented the high compression behaviors and condensation pressures for fluorocarbon microbubbles with various lipid coatings over a large temperature range. A custom observation chamber, with pressure and temperature control, was created to monitor microbubble condensation under brightfield and fluorescent microscopy. A theoretical microbubble compression model was derived to compare to experimental microbubble compression measurements. Droplet formation was confirmed visually and with current particle sizing techniques. Fluorescent microscopy elucidated information on the mechanical behavior of the lipid monolayer shell during compression and condensation. The amount of fluorocarbon gas in the surrounding media greatly affected compression and condensation stability. Microbubble compression behavior varied with temperature. At lower lipid reduced temperatures, microbubbles resisted compression, but as temperature was increased they behaved similar to ideal gas compression with dissolution. Microbubbles condensed at pressures higher than predicted by Laplace, but lower than predicted by homogeneous nucleation theory. Increasing the acyl chain length of the lipid monolayer shell was found to increase condensation strength. It was determined that the combination of shell strength and core supersaturated stability was responsible for the heightened saturation pressures.

In Chapter 4, the thermal vaporization of microbubble condensed fluorocarbon nanodrops with multiple lipid shell compositions was observed. A novel optical chamber was fabricated to permit temperature and pressure control while providing light-extinction in the presence of

microbubbles and light-transmission in the presence of nanodrops. Thermal vaporization and dissolution rates of condensed nanoemulsions were deducted by comparing light-transmission data to Beer's law. Thermal activation energies were quantified by constructing Arrhenius plots with measured vaporization rates. Higher acyl chain length lipid-coated drops had greater activation energies and resistance to high heat dissolution. C18-C24 acyl chain lipid coatings also enhanced droplet vaporization probability. The vaporization temperature was determined for two fluorocarbons as the 90% probability of droplet vaporization which was 90% of the materials critical temperature agreeing with homogeneous nucleation vaporization theory. The cyclic condensation and vaporization ability of fluorocarbon droplets was presented and showed high phase-change hysteretic stability for 10 cycles.

An attempt to utilize fluorocarbon nanodrops as a temperature feedback probe for ultrasound imaging was presented in Chapter 5. Microbubble condensed nanodrops were fabricated with two fluorocarbons, one fluorocarbon more volatile than the other, to vaporize at predetermined temperatures. Using the methodology from Chapter 4, these two component lipid stabilized nanodrops vaporized at different temperatures between 37 and 74 °C, dependent upon the molar ratio of the core mixture, in a fluorocarbon saturated environment. A temperature controlled ultrasound water bath apparatus was constructed to measure condensed droplet vaporization temperatures under diagnostic ultrasound imaging. Ultrasound imaging provided droplet vaporization temperatures that differed from the measurements taken in the light-extinction chamber. This result was assumed to be due to the greater dissolution of the volatile fluorocarbon species out of the droplet core and into the air-saturated surrounding medium.

6.2 Future Work

Lipid-coated microbubble condensed fluorocarbon nanoemulsion condensation and vaporization properties have been extensively reviewed in this work. This sections makes suggestions for furthering the knowledge of condensed nanodrops and improving their design for all fields of study and applications.

The amazing stability of microbubbles before and after condensation is owed to their lipid monolayer coating. In Chapter 3, the lipid monolayer shell was observed during condensation with fluorescent microscopy. This study suggested the formation and department of lipid bilayers existing around the condensed nanodrop. To better understand lipid membrane mechanics and more accurately quantify the droplet vaporization energy barrier, freeze-fracture electron microscopy (FFEM) should be conducted on size-isolated lipid-coated microbubble condensed nanodrops. FFEM has been used to analyze the nanostructure of many biological materials in cell biology. Nanodrops can be formed through condensation, rapidly froze with liquid nitrogen and fractured to expose the nanostructure. Upon fracture, the droplet nanostructure would be coated with carbon and platinum making visible under electron microscopy. The specificity of freeze-fracture in combination with the resolution of electron microscopy could provide amazing images of the lipid-monolayer post condensation and confirm lipid bilayer formation and location with respect to the nanodrop. These results would either support or reject the predicted lipid-cohesion energy barrier found in Chapter 4.

Additionally, further understanding of the lipid shell during vaporization could provide insight into complex lipid mechanics. Specifically, visualizing lipid incorporation at the interface of a rapidly vaporizing droplet through bilayer unzipping or free lipid adhesion could help quantify the energies associated with changing the molecular structure of a lipid membrane. To observe

the lipid monolayer during vaporization, optical vaporization of a fluorescent lipid-coated condensed droplet is suggested. Optical excitation can heat a droplet without heating the surrounding solution, preventing natural convection of the suspension and allowing the droplet to be stationary during vaporization. Fluorescent nanodrops can be made by condensing fluorescent microbubbles as seen in Chapter 3. In addition to the fluorescent shell, gold nanoparticles should be conjugated to the shell with the same avidin-biotin binding techniques as previously performed by Dr. Jake Dove in optical droplet vaporization studies. An experimental apparatus permitting the concentric alignment of fluorescent microscopy with an optical energy source would need to be designed to complete this work. In addition to the fluorescent microscopy, inductively coupled plasma (ICP) mass spectrometry could be performed before condensation and after vaporization on washed gold nanoparticle-templated microbubbles to quantitatively determine the loss in lipid material during phase change.

To improve the stability of nanoemulsions during phase change processes, new shell materials should be explored. Naturally occurring lipid monolayers in lung surfactant contain an assortment of proteins that help facilitate the bending and folding of a monolayer. Chapter 1. briefly introduced the bovine extracted lung surfactant, Survanta. Survanta contains these essential bending and anchoring proteins and is readily available in the Borden lab. A hysteretic phase change experiment, similar to the one conducted in Chapter 4, should be conducted on both perfluoropropane (C_3F_8) and perfluorobutane (C_4F_{10}) microbubbles coated with Survanta and compared to the previously observed C22 coated C_3F_8 microbubbles. This study would verify the importance of folding proteins in the stabilization of a highly compressed lipid monolayer. All lipid monolayer observation studies previously reported and proposed could be conducted on Survanta coated phase change emulsions for comparison to higher strength monolayers. If it was

found that Survanta provided desirable phase change behaviors, but lacked the resistance to gas dissolution of the higher acyl chain lipid monolayers, then synthetic lipid synthesis could be pursued. A DAPC (C20):DSPE-PEG 2K lipid monolayer composition with added sp-B and sp-C folding proteins is suggested as an optimal fluorocarbon phase change agent shell material.

It was found in Chapter 5 that two-component core condensed nanodrops lacked the dissolution stability in an open environment necessary for being applied as an acoustic thermal probe. There are two immediate ways to improve acoustic thermal probe nanodrops: 1. Find a shell with an exceptional resistance to gas permeation and mix the fluorocarbons as described in Chapter 5. 2. Find a pure material that is safe for medical use and whose 90% critical temperature equates to the desired thermal indication temperature. The latter of the two is suggested for designing an acoustic thermal probe because of the ideal compressibility of the lipid monolayer shell. There may exist shell materials with great resistances to diffusion, but lack the mechanical properties required for enhancing contrast in diagnostic ultrasound.

In this work initial steps have been taken towards applying condensed fluorocarbon nanoemulsions as acoustic thermal probes. The next steps need to subject condensed nanoemulsions to thermotherapies under ultrasound imaging and determine if they behave the same way. High intensity focused ultrasound (HIFU) could be applied to the imaging studies performed in Chapter 5 to determine any changes in vaporization conditions. To elaborate, tissue mimicking phantoms could be loaded with nanodrops and subjected to HIFU heating. Ideally, a thermocouple would be placed in the phantom at the location of the HIFU-heated drops and verify vaporization temperatures. Once phantom studies provide consistent results, condensed fluorocarbon droplets could be applied *in vivo* for small animals and provide temperature feedback during HIFU tumor tissue ablation.

Bibliography

Ahmar, E.E. et al., 2011. Isothermal Vapor−Liquid Equilibrium Data for the Perfluorobutane (R610) + Ethane System at Temperatures from (263 to 353) K. Journal of Chemical & Engineering Data, 56(5), pp.1918–1924.

Apfel, R.E., 1979. The superheated drop detector. Nuclear Instruments and Methods, 162(1–3), pp.603–608.

Asami, R., Azuma, T. and Kawabata, K., 2009. Fluorocarbon droplets as next generation contrast agents 2013;3 MHz ultrasound. In: Ultrasonics Symposium (IUS), 2009 IEEE International. pp.1294 –1297.

Avedisian, C.T. and Glassman, I., 1981. High Pressure Homogeneous Nucleation of Bubbles within Superheated Binary Liquid Mixtures. Journal of Heat Transfer, 103(2), pp.272–280.

Baker, E.T. and Lavelle, J.W., 1984. The effect of particle size on the light attenuation coefficient of natural suspensions. Journal of Geophysical Research: Oceans, 89(C5), pp.8197–8203.

Balen, F.G., Allen, C.M. and Lees, W.R., 1994. Ultrasound contrast agents. Clinical Radiology, 49(2), pp.77–82.

Barnabé-Heider, M. et al., 2005. Response of superheated droplet detectors of the PICASSO dark matter search experiment. Nuclear Instruments and Methods in Physics Research Section A: Accelerators, Spectrometers, Detectors and Associated Equipment, 555(1–2), pp.184–204.

Bertsch, F. et al., 1998. Non-invasive temperature mapping using MRI: comparison of two methods based on chemical shift and T1-relaxation. Magnetic Resonance Imaging, 16(4), pp.393–403.

Borden, M., 2009. Nanostructural features on stable microbubbles. Soft Matter, 5(4), pp.716–720.

Borden, M.A. et al., 2005. Influence of lipid shell physicochemical properties on ultrasound-induced microbubble destruction. IEEE Transactions on Ultrasonics, Ferroelectrics and Frequency Control, 52(11), pp.1992–2002.

Borden, M.A. and Longo, M.L., 2002. Dissolution Behavior of Lipid Monolayer-Coated, Air-Filled Microbubbles: Effect of Lipid Hydrophobic Chain Length. Langmuir, 18(24), pp.9225–9233.

Borden, M.A. and Longo, M.L., 2004a. Oxygen Permeability of Fully Condensed Lipid Monolayers. The Journal of Physical Chemistry B, 108(19), pp.6009–6016.

Borden, M.A. and Longo, M.L., 2004b. Oxygen Permeability of Fully Condensed Lipid Monolayers. The Journal of Physical Chemistry B, 108(19), pp.6009–6016.

Boukhira, N. et al., 2000. Suitability of superheated droplet detectors for dark matter search. Astroparticle Physics, 14(3), pp.227–237.

Brace, C.L., 2010. Microwave Tissue Ablation: Biophysics, Technology, and Applications. Critical Reviews™ in Biomedical Engineering, 38(1), pp.65–78.

Brown, J.A. and Mears, W.H., 1958. Physical Properties of n-Perfluorobutane. The Journal of Physical Chemistry, 62(8), pp.960–962.

Cahn, J.W., 1961. On spinodal decomposition. Acta Metallurgica, 9(9), pp.795–801.

Carey, V.P., 2007. Liquid Vapor Phase Change Phenomena: An Introduction to the Thermophysics of Vaporization and Condensation Processes in Heat Transfer Equipment, Second Edition. 2 edition ed. New York: CRC Press.

Child, M.S., 2012. Molecular Collision Theory. Courier Dover Publications.

Cilio, M.R. and Ferriero, D.M., 2010. Synergistic neuroprotective therapies with hypothermia. Seminars in Fetal and Neonatal Medicine, 15(5), pp.293–298.

Cline, H.E. et al., 1994. MR temperature mapping of focused ultrasound surgery. Magnetic Resonance in Medicine, 31(6), pp.628–636.

Culp, W.C. et al., 2001. Microbubble Potentiated Ultrasound as a Method of Declotting Thrombosed Dialysis Grafts: Experimental Study in Dogs. CardioVascular and Interventional Radiology, 24(6), pp.407–412.

Cuthbertson, A. et al., 2003. Amphiphilic Lipopeptide Microparticles as Contrast Agents for Medical Ultrasound Imaging. Macromolecular Bioscience, 3(1), pp.11–17.

D'Arrigo, J.S. and Imae, T., 1992. Physical characteristics of ultrastable lipid-coated microbubbles. Journal of Colloid and Interface Science, 149(2), pp.592–595.

Davies, J.T. and Rideal, S.E.K., 1963. Interfacial phenomena. Academic Press.

Díaz-López, R., Tsapis, N. and Fattal, E., 2009. Liquid Perfluorocarbons as Contrast Agents for Ultrasonography and 19F-MRI. Pharmaceutical Research, 27(1), pp.1–16.

Dove, J.D., Mountford, P.A., Murray, T.W. and Borden, M.A., 2014. Engineering optically triggered droplets for photoacoustic imaging and therapy. Biomedical Optics Express, 5(12), p.4417.

Dove, J.D., Murray, T.W. and Borden, M.A., 2013. Enhanced photoacoustic response with plasmonic nanoparticle-templated microbubbles. Soft Matter, 9(32), pp.7743–7750.

Duncan, P.B. and Needham, D., 2004. Test of the Epstein−Plesset Model for Gas Microparticle Dissolution in Aqueous Media: Effect of Surface Tension and Gas Undersaturation in Solution. Langmuir, 20(7), pp.2567–2578.

Eastoe, J. and Dalton, J.S., 2000. Dynamic surface tension and adsorption mechanisms of surfactants at the air–water interface. Advances in Colloid and Interface Science, 85(2–3), pp.103–144.

Eberhart, J.G., 1976. The thermodynamic and the kinetic limits of superheat of a liquid. Journal of Colloid and Interface Science, 56(2), pp.262–269.

Epstein, P.S. and Plesset, M.S., 1950a. On the Stability of Gas Bubbles in Liquid-Gas Solutions. The Journal of Chemical Physics, 18(11), p.1505.

Epstein, P.S. and Plesset, M.S., 1950b. On the Stability of Gas Bubbles in Liquid-Gas Solutions. The Journal of Chemical Physics, 18(11), pp.1505–1509.

Fabiilli, M.L. et al., 2009. The role of inertial cavitation in acoustic droplet vaporization. IEEE Transactions on Ultrasonics, Ferroelectrics and Frequency Control, 56(5), pp.1006–1017.

Fang, J.-Y., Hung, C.-F., Hua, S.-C. and Hwang, T.-L., 2009. Acoustically active perfluorocarbon nanoemulsions as drug delivery carriers for camptothecin: Drug release and cytotoxicity against cancer cells. Ultrasonics, 49(1), pp.39–46.

Felizardo, M. et al., 2008. New acoustic instrumentation for the SIMPLE superheated droplet detector. Nuclear Instruments and Methods in Physics Research Section A: Accelerators, Spectrometers, Detectors and Associated Equipment, 589(1), pp.72–84.

Fenster, A. and Downey, D.B., 1996. 3-D ultrasound imaging: a review. IEEE Engineering in Medicine and Biology Magazine, 15(6), pp.41–51.

Ferrara, K., Pollard, R. and Borden, M., 2007a. Ultrasound Microbubble Contrast Agents: Fundamentals and Application to Gene and Drug Delivery. Annual Review of Biomedical Engineering, 9(1), pp.415–447.

Ferrara, K., Pollard, R. and Borden, M., 2007b. Ultrasound microbubble contrast agents: fundamentals and application to gene and drug delivery. Annual Review of Biomedical Engineering, 9, pp.415–447.

Feshitan, J.A., Chen, C.C., Kwan, J.J. and Borden, M.A., 2009. Microbubble size isolation by differential centrifugation. Journal of Colloid and Interface Science, 329(2), pp.316–324.

Gaines, G.L., 1966. Insoluble monolayers at liquid-gas interfaces. Interscience Publishers.

Garg, S., Thomas, A.A. and Borden, M.A., 2013. The effect of lipid monolayer in-plane rigidity on in vivo microbubble circulation persistence. Biomaterials, 34(28), pp.6862–6870.

Gittens, G.J., 1969. Variation of surface tension of water with temperature. Journal of Colloid and Interface Science, 30(3), pp.406–412.

Goldberg, B.B., Liu, J.-B. and Forsberg, F., 1994. Ultrasound contrast agents: A review. Ultrasound in Medicine & Biology, 20(4), pp.319–333.

Gopal, A. et al., 2006. Microscopic Folds and Macroscopic Jerks in Compressed Lipid Monolayers. The Journal of Physical Chemistry B, 110(21), pp.10220–10223.

Gorce, J.M., Arditi, M. and Schneider, M., 2000. Influence of bubble size distribution on the echogenicity of ultrasound contrast agents: a study of SonoVue. Investigative Radiology, 35(11), pp.661–671.

Gramiak, R. and Shah, P.M., 1968. Echocardiography of the aortic root. Investigative Radiology, 3(5), pp.356–366.

Hamel, L.A. et al., 1997. A superheated droplet detector for dark matter search. Nuclear Instruments and Methods in Physics Research Section A: Accelerators, Spectrometers, Detectors and Associated Equipment, 388(1–2), pp.91–99.

Hannah, A. et al., 2014. Indocyanine Green-Loaded Photoacoustic Nanodroplets: Dual Contrast Nanoconstructs for Enhanced Photoacoustic and Ultrasound Imaging. ACS Nano, 8(1), pp.250–259.

Hernot, S. and Klibanov, A.L., 2008. Microbubbles in ultrasound-triggered drug and gene delivery. Advanced Drug Delivery Reviews, 60(10), pp.1153–1166.

Hettiarachchi, K. et al., 2007. On-chip generation of microbubbles as a practical technology for manufacturing contrast agents for ultrasonic imaging. Lab on a Chip, 7(4), pp.463–468.

Hides, J.A., Richardson, C.A. and Jull, G.A., 1998. Use of real-time ultrasound imaging for feedback in rehabilitation. Manual Therapy, 3(3), pp.125–131.

Hobbs, S.K. et al., 1998. Regulation of Transport Pathways in Tumor Vessels: Role of Tumor Type and Microenvironment. Proceedings of the National Academy of Sciences, 95(8), pp.4607–4612.

Hoff, L., 2002. Acoustic characterization of contrast agents for medical ultrasound imaging. Springer.

Hung, C.-H., Krasnopoler, M.J. and Katz, J.L., 1989. Condensation of a supersaturated vapor. VIII. The homogeneous nucleation of n-nonane. The Journal of Chemical Physics, 90(3), pp.1856–1865.

Husseini, G.A., Pitt, W.G. and Martins, A.M., 2014. Ultrasonically triggered drug delivery: Breaking the barrier. Colloids and Surfaces B: Biointerfaces, 123, pp.364–386.

Illingworth, A.J., 1988. The formation of rain in convective clouds. Nature, 336(6201), pp.754–756.

Israelachvili, J.N., 1992. Intermolecular and Surface Forces, Second Edition: With Applications to Colloidal and Biological Systems. 2nd ed. Academic Press.

Jarvis, T.J., Donohue, M.D. and Katz, J.L., 1975. Bubble nucleation mechanisms of liquid droplets superheated in other liquids. Journal of Colloid and Interface Science, 50(2), pp.359–368.

Jolesz, F.A., 2009. MRI-Guided Focused Ultrasound Surgery. Annual review of medicine, 60, pp.417–430.

Kaneko, Y. et al., 2005. Use of a microbubble agent to increase the effects of high intensity focused ultrasound on liver tissue. European Radiology, 15(7), pp.1415–1420.

Katiyar, A. and Sarkar, K., 2010. Stability analysis of an encapsulated microbubble against gas diffusion. Journal of Colloid and Interface Science, 343(1), pp.42–47.

Katiyar, A., Sarkar, K. and Jain, P., 2009a. Effects of encapsulation elasticity on the stability of an encapsulated microbubble. Journal of Colloid and Interface Science, 336(2), pp.519–525.

Katiyar, A., Sarkar, K. and Jain, P., 2009b. Effects of encapsulation elasticity on the stability of an encapsulated microbubble. Journal of colloid and interface science, 336(2), pp.519–525.

Katz, J.L. and Blander, M., 1973. Condensation and boiling: Corrections to homogeneous nucleation theory for nonideal gases. Journal of Colloid and Interface Science, 42(3), pp.496–502.

Kawabata, K. et al., 2005. Nanoparticles with Multiple Perfluorocarbons for Controllable Ultrasonically Induced Phase Shifting. Japanese Journal of Applied Physics, 44, pp.4548–4552.

Ke, H. et al., 2009. Quantum-dot-modified microbubbles with bi-mode imaging capabilities. Nanotechnology, 20(42), p.425105.

Kim, C. et al., 2010. Multifunctional microbubbles and nanobubbles for photoacoustic and ultrasound imaging. Journal of Biomedical Optics, 15(1), p.010510.

Kim, D.H., Costello, M.J., Duncan, P.B. and Needham, D., 2003a. Mechanical Properties and Microstructure of Polycrystalline Phospholipid Monolayer Shells: Novel Solid Microparticles. Langmuir, 19(20), pp.8455–8466.

Kim, D.H., Costello, M.J., Duncan, P.B. and Needham, D., 2003b. Mechanical Properties and Microstructure of Polycrystalline Phospholipid Monolayer Shells: Novel Solid Microparticles. Langmuir, 19(20), pp.8455–8466.

Kim, S.H. and Franses, E.I., 2005. New protocols for preparing dipalmitoylphosphatidylcholine dispersions and controlling surface tension and competitive adsorption with albumin at the air/aqueous interface. Colloids and Surfaces. B, Biointerfaces, 43(3-4), pp.256–266.

Kincaid, J.F. and Eyring, H., 1938. Free Volumes and Free Angle Ratios of Molecules in Liquids. The Journal of Chemical Physics, 6(10), pp.620–629.

Kopechek, J. et al., 2013. Accumulation of Phase-Shift Nanoemulsions to Enhance MR-Guided Ultrasound-Mediated Tumor Ablation In Vivo. Journal of Healthcare Engineering, 4(1), pp.109–126.

Kopechek, J.A., Zhang, P., Burgess, M.T. and Porter, T.M., 2012. Synthesis of Phase-shift Nanoemulsions with Narrow Size Distributions for Acoustic Droplet Vaporization and Bubble-enhanced Ultrasound-mediated Ablation. Journal of Visualized Experiments, (67).

Krafft, M.P., 2001. Fluorocarbons and fluorinated amphiphiles in drug delivery and biomedical research. Advanced Drug Delivery Reviews, 47(2–3), pp.209–228.

Kripfgans, O.D. et al., 2000. Acoustic droplet vaporization for therapeutic and diagnostic applications. Ultrasound in Medicine & Biology, 26(7), pp.1177–1189.

Kwak, H.-Y. and Lee, S., 1991. Homogeneous Bubble Nucleation Predicted by a Molecular Interaction Model. Journal of Heat Transfer, 113(3), pp.714–721.

Kwan, J.J., 2012. Theranostic Oxygen Delivery Using Ultrasound and Microbubbles. Theranostics, 2(12), pp.1174–1184.

Kwan, J.J. and Borden, M.A., 2010. Microbubble Dissolution in a Multigas Environment. Langmuir, 26(9), pp.6542–6548.

Kwan, J.J. and Borden, M.A., 2012a. Lipid monolayer collapse and microbubble stability. Advances in Colloid and Interface Science, 183–184, pp.82–99.

Kwan, J.J. and Borden, M.A., 2012b. Lipid monolayer dilatational mechanics during microbubble gas exchange. Soft Matter, 8(17), pp.4756–4766.

Lamberti, V.E., Fosdick, L.D., Jessup, E.R. and Schauble, C.J.C., 2002. A Hands-On Introduction to Molecular Dynamics. Journal of Chemical Education, 79(5), p.601.

Langmuir, I. and Schaefer, V.J., 1943. Rates of evaporation of water through compressed monolayers on water. Journal of the Franklin Institute, 235(2), pp.119–162.

L'Annunziata, M.F., 2012. Handbook of radioactivity analysis.

Lemmon, E. W., Huber, M. L., and McLinden, M. O., 2002, NIST reference fluid thermodynamic and transport properties–REFPROP, Version.

Lide, D.R., 1999. CRC Handbook of chemistry and physics: a ready-reference book of chemical and physical data. Boca Raton [etc.]: CRC press.

Lin, C.-Y. and Pitt, W.G., 2013. Acoustic Droplet Vaporization in Biology and Medicine. BioMed Research International, 2013.

Lindner, J.R. et al., 2002. Microvascular rheology of Definity microbubbles after intra-arterial and intravenous administration. Journal of the American Society of Echocardiography: Official Publication of the American Society of Echocardiography, 15(5), pp.396–403.

Li, P., Armstrong, W.F. and Miller, D.L., 2004. Impact of myocardial contrast echocardiography on vascular permeability: comparison of three different contrast agents. Ultrasound in Medicine & Biology, 30(1), pp.83–91.

Lipp, M.M., Lee, K.Y., Zasadzinski, J.A. and Waring, A.J., 1996. Phase and morphology changes in lipid monolayers induced by SP-B protein and its amino-terminal peptide. Science (New York, N.Y.), 273(5279), pp.1196–1199.

Liu, Z. et al., 2011. Iron oxide nanoparticle-containing microbubble composites as contrast agents for MR and ultrasound dual-modality imaging. Biomaterials, 32(26), pp.6155–6163.

Liu, Z., Kiessling, F. and Gätjens, J., 2010. Advanced Nanomaterials in Multimodal Imaging: Design, Functionalization, and Biomedical Applications. J. Nanomaterials, 2010, pp.51:1–51:15.

Lum, A.F.H. et al., 2006. Ultrasound radiation force enables targeted deposition of model drug carriers loaded on microbubbles. Journal of Controlled Release, 111(1–2), pp.128–134.

MacDonald, R.C. and Simon, S.A., 1987. Lipid monolayer states and their relationships to bilayers. Proceedings of the National Academy of Sciences, 84(12), pp.4089–4093.

Marmottant, P. et al., 2005. A model for large amplitude oscillations of coated bubbles accounting for buckling and rupture. The Journal of the Acoustical Society of America, 118(6), pp.3499–3505.

Marsh, D., 2013. Handbook of Lipid Bilayers, Second Edition. CRC Press.

Martin, A.L. et al., 2012. Intracellular Growth of Nanoscale Perfluorocarbon Droplets for Enhanced Ultrasound-Induced Phase-Change Conversion. Ultrasound in Medicine & Biology, 38(10), pp.1799–1810.

Martz, T.D. et al., n.d. Precision Manufacture of Phase-Change Perfluorocarbon Droplets Using Microfluidics. Ultrasound in Medicine & Biology, (0).

Matsunaga, T.O. et al., 2012. Phase-change nanoparticles using highly volatile perfluorocarbons: toward a platform for extravascular ultrasound imaging. Theranostics, 2(12), pp.1185–1198.

McConnell, H.M., 1991. Structures and Transitions in Lipid Monolayers at the Air-Water Interface. Annual Review of Physical Chemistry, 42(1), pp.171–195.

McConnell, H.M., Tamm, L.K. and Weis, R.M., 1984. Periodic structures in lipid monolayer phase transitions. Proceedings of the National Academy of Sciences, 81(10), pp.3249–3253.

MD, B.B.G., 1996. Ultrasound Contrast Agents. London: CRC Press.

Meairs, S. and Alonso, A., 2007. Ultrasound, microbubbles and the blood–brain barrier. Progress in Biophysics and Molecular Biology, 93(1–3), pp.354–362.

Medwin, H., 1974. Acoustic fluctuations due to microbubbles in the near-surface ocean. The Journal of the Acoustical Society of America, 56(4), pp.1100–1104.

Menger, F.M., 1979. Laplace pressure inside micelles. The Journal of Physical Chemistry, 83(7), pp.893–893.

Mesiwala, A.H. et al., 2002. High-intensity focused ultrasound selectively disrupts the blood-brain barrier in vivo. Ultrasound in Medicine & Biology, 28(3), pp.389–400.

Morgan, K.E. et al., 2000. Experimental and theoretical evaluation of microbubble behavior: effect of transmitted phase and bubble size. IEEE Transactions on Ultrasonics, Ferroelectrics and Frequency Control, 47(6), pp.1494 –1509.

Mountford, P.A., Sirsi, S.R. and Borden, M.A., 2014. Condensation Phase Diagrams for Lipid-Coated Perfluorobutane Microbubbles. Langmuir, 30(21), pp.6209–6218.

Mountford, P.A., Thomas, A.N. and Borden, M.A., 2015. Thermal Activation of Superheated Lipid-Coated Perfluorocarbon Drops. Langmuir, 31(16), pp.4627–4634.

Moyer, L.C. et al., 2015. High-intensity focused ultrasound ablation enhancement in vivo via phase-shift nanodroplets compared to microbubbles. Journal of Therapeutic Ultrasound, 3(1), p.7.

Nahum Goldberg, S. et al., 1995. Tissue ablation with radiofrequency: Effect of probe size, gauge, duration, and temperature on lesion volume. Academic Radiology, 2(5), pp.399–404.

Nishihara, M., Imai, K. and Yokoyama, M., 2009. Preparation of Perfluorocarbon/Fluoroalkyl Polymer Nanodroplets for Cancer-targeted Ultrasound Contrast Agents. Chemistry Letters, 38(6), pp.556–557.

Noguez, C. and Garzón, I.L., 2009. Optically active metal nanoparticles. Chemical Society Reviews, 38(3), pp.757–771.

Nosé, S., 1984. A molecular dynamics method for simulations in the canonical ensemble. Molecular Physics, 52(2), pp.255–268.

Okada, K. et al., 2010. Characteristics of microbubbles generated by porous mullite ceramics prepared by an extrusion method using organic fibers as the pore former. Journal of the European Ceramic Society, 30(6), pp.1245–1251.

Ophir, J., 1986. Estimation of the Speed of Ultrasound Propagation in Biological Tissues: A Beam-Tracking Method. IEEE Transactions on Ultrasonics, Ferroelectrics, and Frequency Control, 33(4), pp.359–368.

Pace, E.L. and Plaush, A.C., 1967. Thermodynamic Properties of Octafluoropropane from 14°K to Its Normal Boiling Point. An Estimate of the Barrier to Internal Rotation from the Entropy and Heat Capacity of the Gas. The Journal of Chemical Physics, 47(1), pp.38–43.

Park, J.I. et al., 2010. Microbubbles Loaded with Nanoparticles: A Route to Multiple Imaging Modalities. ACS Nano, 4(11), pp.6579–6586.

Pawley, J., 2010. Handbook of Biological Confocal Microscopy. Springer.

Pedley, T.J., 1977. Pulmonary Fluid Dynamics. Annual Review of Fluid Mechanics, 9(1), pp.229–274.

Pissuwan, D., Valenzuela, S.M. and Cortie, M.B., 2006. Therapeutic possibilities of plasmonically heated gold nanoparticles. Trends in Biotechnology, 24(2), pp.62–67.

Pitt, W.G. et al., 2014. Phase transitions of perfluorocarbon nanoemulsion induced with ultrasound: A mathematical model. Ultrasonics Sonochemistry, 21(2), pp.879–891.

Porter, T.R. and Xie, F., 2001. Ultrasound, microbubbles, and thrombolysis. Progress in Cardiovascular Diseases, 44(2), pp.101–110.

Prausnitz, J.M., Lichtenthaler, R.N. and Azevedo, E.G. de, 1998. Molecular Thermodynamics of Fluid-Phase Equilibria. 3 edition ed. Upper Saddle River, N.J: Prentice Hall.

Rapoport, N. et al., 2011. Ultrasound-mediated tumor imaging and nanotherapy using drug loaded, block copolymer stabilized perfluorocarbon nanoemulsions. Journal of Controlled Release, 153(1), pp.4–15.

Rapoport, N., 2012a. Phase-shift, stimuli-responsive perfluorocarbon nanodroplets for drug delivery to cancer. Wiley interdisciplinary reviews. Nanomedicine and nanobiotechnology, 4(5), pp.492–510.

Rapoport, N., 2012b. Phase-shift, stimuli-responsive perfluorocarbon nanodroplets for drug delivery to cancer. Wiley Interdisciplinary Reviews: Nanomedicine and Nanobiotechnology, 4(5), pp.492–510.

Rapoport, N.Y. et al., 2009. Controlled and targeted tumor chemotherapy by ultrasound-activated nanoemulsions/microbubbles. Journal of Controlled Release, 138(3), pp.268–276.

Reif, F., 2008. Fundamentals of Statistical and Thermal Physics. Waveland Pr Inc.

Reznik, N. et al., 2013. The efficiency and stability of bubble formation by acoustic vaporization of submicron perfluorocarbon droplets. Ultrasonics, 53(7), pp.1368–1376.

Reznik, N., Williams, R. and Burns, P.N., 2011. Investigation of Vaporized Submicron Perfluorocarbon Droplets as an Ultrasound Contrast Agent. Ultrasound in Medicine & Biology, 37(8), pp.1271–1279.

Samset, E., 2006. Temperature mapping of thermal ablation using MRI. Minimally Invasive Therapy & Allied Technologies, 15(1), pp.36–41.

Sarkar, K., Shi, W.T., Chatterjee, D. and Forsberg, F., 2005. Characterization of ultrasound contrast microbubbles using in vitro experiments and viscous and viscoelastic interface models for encapsulation. The Journal of the Acoustical Society of America, 118(1), pp.539–550.

Sarker, D.K., 2005. Engineering of Nanoemulsions for Drug Delivery. Current Drug Delivery, 2(4), pp.297–310.

Satinover, S.J., Dove, J.D. and Borden, M.A., 2014. Single-Particle Optical Sizing of Microbubbles. Ultrasound in Medicine & Biology, 40(1), pp.138–147.

Sboros, V. et al., 2007. Acoustic Rayleigh scattering at individual micron-sized bubbles. Applied Physics Letters, 90(12), p.123902.

Schwarz, R., Schuurmans, M., Seelig, J. and Künnecke, B., 1999. 19F-MRI of perfluorononane as a novel contrast modality for gastrointestinal imaging. Magnetic Resonance in Medicine, 41(1), pp.80–86.

Seo, M., Gorelikov, I., Williams, R. and Matsuura, N., 2010. Microfluidic Assembly of Monodisperse, Nanoparticle-Incorporated Perfluorocarbon Microbubbles for Medical Imaging and Therapy. Langmuir, 26(17), pp.13855–13860.

Sheeran, P.S. et al., 2011a. Decafluorobutane as a Phase-Change Contrast Agent for Low-Energy Extravascular Ultrasonic Imaging. Ultrasound in Medicine & Biology, 37(9), pp.1518–1530.

Sheeran, P.S. et al., 2012. Design of ultrasonically-activatable nanoparticles using low boiling point perfluorocarbons. Biomaterials, 33(11), pp.3262–3269.

Sheeran, P.S. and Dayton, P.A., 2012. Phase-change contrast agents for imaging and therapy. Current Pharmaceutical Design, 18(15), pp.2152–2165.

Sheeran, P.S., Luois, S., Dayton, P.A. and Matsunaga, T.O., 2011c. Formulation and Acoustic Studies of a New Phase-Shift Agent for Diagnostic and Therapeutic Ultrasound. Langmuir, 27(17), pp.10412–10420.

Sheeran, P.S., Luois, S., Matsunaga, T.O. and Dayton, P.A., 2011d. Submicron decafluorobutane phase-change contrast agents generated by microbubble condensation. In: Ultrasonics Symposium (IUS), 2011 IEEE International. Ultrasonics Symposium (IUS), 2011 IEEE International. pp.636–639.

Sheeran, P.S., Matsunaga, T.O. and Dayton, P.A., 2013. Phase-transition thresholds and vaporization phenomena for ultrasound phase-change nanoemulsions assessed via high-speed optical microscopy. Physics in Medicine and Biology, 58(13), pp.4513–4534.

Sheeran, P.S., Matsunaga, T.O. and Dayton, P.A., 2014. Phase change events of volatile liquid perfluorocarbon contrast agents produce unique acoustic signatures. Physics in Medicine and Biology, 59(2), pp.379–401.

Shpak, O. et al., 2014a. Acoustic droplet vaporization is initiated by superharmonic focusing. Proceedings of the National Academy of Sciences, 111(5), pp.1697–1702.

Shpak, O. et al., 2014b. Acoustic droplet vaporization is initiated by superharmonic focusing. Proceedings of the National Academy of Sciences, 111(5), pp.1697–1702.

Sirsi, S. et al., 2009. Lung surfactant microbubbles. Soft Matter, 5(23), pp.4835–4842.

Sirsi, S. et al., 2010. Effect of Microbubble Size on Fundamental Mode High Frequency Ultrasound Imaging in Mice. Ultrasound in Medicine & Biology, 36(6), pp.935–948.

Sirsi, S.R., 2013. Lung Surfactant Microbubbles Increase Lipophilic Drug Payload for Ultrasound-Targeted Delivery. Theranostics, 3(6), pp.409–419.

Sirsi, S.R. and Borden, M.A., 2014. State-of-the-art materials for ultrasound-triggered drug delivery. Advanced Drug Delivery Reviews, 72, pp.3–14.

Skalak, R. and Branemark, P.I., 1969. Deformation of Red Blood Cells in Capillaries. Science, 164(3880), pp.717–719.

Skinner, L.M. and Sambles, J.R., 1972. The Kelvin equation—a review. Journal of Aerosol Science, 3(3), pp.199–210.

S, M. et al., 1992. Tissue ablation in benign prostatic hyperplasia with high-intensity focused ultrasound. European urology, 23 Suppl 1, pp.39–43.

Stride, E. and Saffari, N., 2003. Microbubble ultrasound contrast agents: A review. Proceedings of the Institution of Mechanical Engineers, Part H: Journal of Engineering in Medicine, 217(6), pp.429–447.

Strohm, E. et al., 2011. Vaporization of perfluorocarbon droplets using optical irradiation. Biomedical Optics Express, 2(6), pp.1432–1442.

Strohm, E.M. et al., 2010. Optical droplet vaporization (ODV): Photoacoustic characterization of perfluorocarbon droplets. In: 2010 IEEE Ultrasonics Symposium (IUS). 2010 IEEE Ultrasonics Symposium (IUS). IEEE, pp.495–498.

Su, J.T. and Needham, D., 2013. Mass Transfer in the Dissolution of a Multicomponent Liquid Droplet in an Immiscible Liquid Environment. Langmuir, 29(44), pp.13339–13345.

Suslick, K.S. and Grinstaff, M.W., 1990. Protein microencapsulation of nonaqueous liquids. Journal of the American Chemical Society, 112(21), pp.7807–7809.

Thomson, G.W., 1946. The Antoine Equation for Vapor-pressure Data. Chemical Reviews, 38(1), pp.1–39.

Tierney, D.F. and Johnson, R.P., 1965. Altered surface tension of lung extracts and lung mechanics. Journal of Applied Physiology, 20(6), pp.1253–1260.

Tsige, M. and Grest, G.S., 2008. Surface Tension and Surface Orientation of Perfluorinated Alkanes. The Journal of Physical Chemistry C, 112(13), pp.5029–5035.

Unger, E.C. et al., 2001. Local drug and gene delivery through microbubbles. Progress in Cardiovascular Diseases, 44(1), pp.45–54.

Unger, E.C. et al., 2004. Therapeutic applications of lipid-coated microbubbles. Advanced Drug Delivery Reviews, 56(9), pp.1291–1314.

Waldram, J.R., 1985. The Theory of Thermodynamics.

Wan, J., Bick, A., Sullivan, M. and Stone, H.A., 2008. Controllable Microfluidic Production of Microbubbles in Water-in-Oil Emulsions and the Formation of Porous Microparticles. Advanced Materials, 20(17), pp.3314–3318.

Watson, K.M., 1943. Thermodynamics of the Liquid State. Industrial & Engineering Chemistry, 35(4), pp.398–406.

Wei, C. et al., 2014a. Laser-induced cavitation in nanoemulsion with gold nanospheres for blood clot disruption: in vitro results. Optics Letters, 39(9), pp.2599–2602.

Wei, C. et al., 2014b. Nonlinear contrast enhancement in photoacoustic molecular imaging with gold nanosphere encapsulated nanoemulsions. Applied Physics Letters, 104(3), p.033701.

Wiebe, R. and Gaddy, V.L., 1940. The Solubility of Carbon Dioxide in Water at Various Temperatures from 12 to 40° and at Pressures to 500 Atmospheres. Critical Phenomena*. Journal of the American Chemical Society, 62(4), pp.815–817.

Williams, R. et al., 2013. Characterization of Submicron Phase-change Perfluorocarbon Droplets for Extravascular Ultrasound Imaging of Cancer. Ultrasound in Medicine & Biology, 39(3), pp.475–489.

Wilson, C.T.R., 1897. Condensation of Water Vapour in the Presence of Dust-Free Air and other Gases. Proceedings of the Royal Society of London, 61(369-377), pp.240–242.

Wilson, K., Homan, K. and Emelianov, S., 2012. Biomedical photoacoustics beyond thermal expansion using triggered nanodroplet vaporization for contrast-enhanced imaging. Nat Commun, 3, p.618.

Yaws, C.L., 2006. The Yaws Handbook of Thermodynamic Properties for Hydrocarbons and Chemicals. Gulf Pub.

Yu, S., Harding, P.G.R., Smith, N. and Possmayer, F., 1983. Bovine pulmonary surfactant: Chemical composition and physical properties. Lipids, 18(8), pp.522–529.

Zhang, M. et al., 2011. Acoustic Droplet Vaporization for Enhancement of Thermal Ablation by High Intensity Focused Ultrasound. Academic Radiology, 18(9), pp.1123–1132.

Zhang, P., Kopechek, J.A. and Porter, T.M., 2013. The impact of vaporized nanoemulsions on ultrasound-mediated ablation. Journal of Therapeutic Ultrasound, 1, p.2.

Zhang, P. and Porter, T., 2010a. An in vitro study of a phase-shift nanoemulsion: A potential nucleation agent for bubble-enhanced HIFU tumor ablation. Ultrasound in Med. & Biol., 36(11), pp.1856–1866.

Zhang, P. and Porter, T., 2010b. An in vitro Study of a Phase-Shift Nanoemulsion: A Potential Nucleation Agent for Bubble-Enhanced HIFU Tumor Ablation. Ultrasound in Medicine & Biology, 36(11), pp.1856–1866.

Zhou, Y.-F., 2011. High intensity focused ultrasound in clinical tumor ablation. World Journal of Clinical Oncology, 2(1), pp.8–27.